Rotation Studies in Fusion Plasmas via Imaging X-ray Crystal Spectroscopy

by

Alexander Charles Ince-Cushman

B.A.Sc., Aerospace Engineering,
University of Toronto (2003)

Submitted to the Department of Nuclear Science & Engineering
in partial fulfillment of the requirements for the degree of

Doctor of Philosophy

at the

MASSACHUSETTS INSTITUTE OF TECHNOLOGY

September 2008

Author .....
Department of Nuclear Science & Engineering
August 28, 2008

Certified by .....
Dr. John E. Rice
Principal Research Scientist
Thesis Supervisor

Certified by .....
Prof. Ian H. Hutchinson
Nuclear Science & Engineering Department Head
Thesis Reader

Accepted by .....
Prof. Jacquelyn C. Yanch
Professor of Nuclear Science & Engineering
Chair, Department Committee on Graduate Students

Rotation Studies in Fusion Plasmas via Imaging X-ray Crystal Spectroscopy

by

Alexander Charles Ince-Cushman

Submitted to the Department of Nuclear Science & Engineering
on August 28, 2008, in partial fulfillment of the
requirements for the degree of
Doctor of Philosophy

Abstract

The increase in plasma performance associated with turbulence suppression via flow shear in magnetically confined fusion plasmas has been well documented. Currently, the standard methods for both generating and measuring plasma rotation involves neutral beam injection (NBI). In the large, high density plasmas envisaged for next generation reactors, such as ITER, NBI will be considerably more difficult than in current experiments. As a result, there is a need to identify alternative methods for generating and measuring plasma flows. In an effort to meet these needs, a high resolution x-ray crystal spectrometer capable of making spatially resolved measurements has been designed, built, installed and operated on the Alcator C-Mod tokamak. By taking advantage of toroidal symmetry and magnetic flux surface mapping it is possible to perform spectral tomography with a single fan of views. This combination of spatially resolved spectra and tomographic techniques has allowed for local measurement of a number of plasma parameters from line integrated x-ray spectra for the first time. In particular these techniques have been used to measure temporally evolving profiles of emissivity, charge state densities, rotation velocities, electron temperature, ion temperature, as well as radial electric field over most of the plasma cross section ($r/a < 0.9$). In this thesis three methods for the generation of flows without the use of NBI are identified; intrinsic rotation in enhanced confinement modes, lower hybrid wave induced rotation and ICRF mode conversion flow drive. Each of these methods is discussed in detail with reference to how they might be used in next generation tokamaks.

Thesis Supervisor: Dr. John E. Rice
Title: Principal Research Scientist

Thesis Supervisor: Prof. Ian H. Hutchinson
Title: Nuclear Science & Engineering Department Head

Acknowledgments

There are a great many people who have helped to produce the work contained in the pages that follow. Without their collective efforts this thesis would simply not have been possible. First and foremost I would like to thank Dr. John Rice for his uncanny ability to blend perfectly the roles of adviser, teacher and friend. He has taught me virtually everything I know about the art and science of being an experimentalist for which I am eternally grateful. There is a number of ways in which John has helped me throughout the years I have known him, not least of which is his unwavering dedication to grammatical correctness (Split infinitives beware, dangling modifiers be gone, and let the data speak for themselves).

My fellow graduate student Mathew Reinke deserves special praise for the tremendous contributions he has made to this work. Among other things, he is responsible for the development and implementation of a spectral tomographic algorithm that was crucial for this thesis. The thoughtfulness and attention to detail that he brings to his work is extraordinary. I can not thank him enough for all his help.

I would also like to acknowledge my collaborators from the Princeton Plasma Physics Laboratory; Doctors Manfred Bitter, Kenneth Hill and Steve Scott. It was Dr Bitter who first conceived of the idea of an imaging x-ray crystal spectrometer. Moreover, it was the early experiments of Dr. Bitter and Dr. Hill on this type of instrument that laid the foundation for the spectrometer that is the focus of this thesis. Their helpful guidance through the design, construction and operation of the spectrometer was invaluable. I would like to thank Dr. Earl Marmar, for his encouragement and for ensuring that this project had all the resources needed for success.

I would like to thank Ming Feng Gu for providing the atomic physics data used throughout the thesis. Here too, Mathew Reinke, deserves the credit for using these data to calculate electron temperature and charge state density profiles based on line emission spectra. I would like to acknowledge the members of the Alcator C-Mod Lower Hybrid Current Drive group (Prof. Ronald Parker, Gregory Wallace, Dr.

Shunichi Shiraiwa, Dr. Randy Wilson, and Orso Meneghini) for their collaborations on joint rotation/lower hybrid experiments. I would like to thank Dr. Yijun Lin for spearheading the investigations of mode conversion flow drive experiments on Alcator C-Mod and his patience in teaching me about this fascinating field of study.

A number of people generously provided data were was used in this thesis. They are: Amanada Hubbard (electron temperature from electron cyclotron emission), Jerry Hughes (electron temperature and density from Thomson scattering), Steve Wolfe (magnetic equilibrium calculations), Catherine Fiore (central ion temperature from neutron emission), Rachael McDermott (ion temperature and radial electric field from charge exchange spectroscopy) and Jim Irby (electron density from interferometry).

I would like to thank my thesis reader, professor Ian Hutchinson for his careful reading of this document and a number of fruitful discussions that undoubtedly improved the final result. I would like acknowledge the other members of my thesis committee, professors Jeffrey Friedberg and Dennis Whyte. In addition to those mentioned above I would like to thank all of the scientists, technicians, professors, administrators and engineers that make up the Alcator C-Mod community, all of whom have helped me over the years: Abhay Ram, Andy Pfeifer, Bob Childs, Bob Granetz, Brain LaBombard, Bruce Lipschultz, Clare Egan, Corrine Fogg, Darin Ernst, Dave Arsenault, Dave Belloffato, Don Nelson, Dorian McNamara, Dragana Zubcevic, Earl Marmar, Ed Fitzgerald, Felix Kreisel, Gary Dekow, Heather Geddry, Henry Bergler, Henry Savelli, James Zaks, Jason Thomas, Jessica Coco, Jim Terry, Joe Bosco, Joe Snipes, Josh Stillerman, Lee Keating, Leslie West, Liz Parmelee, Marcia Tench-Mora, Mark Iverson, Mark London, Martin Greenwald, Matt Fulton, Michael Rowell, Miklos Porkolab, Patrick MacGibbon, Paul Bonoli, Paul Lienard, Paul Rivenberg, Peter Brenton, Peter Catto, Peter Koert, Rachel Morton, Ravi Gondhalekar, Richard Murray, Rick Leccacorvi, Rosalie West, Rui Vieira, Steve Wukitch, Ted Biewer, Tom Fredian, Tommy Toland, Valerie Censabella, William Burke, William Byford, William Parkin, and Xiwen Zhong.

I would also like to thank my fellow graduate students for their help, camaraderie,

and control room antics over the years: Aaron Bader, Alexandre Parisot, Andrea Schmidt, Arturo Dominguez, Brock Bose, Eric Edlund, Gregory Wallace, Igor Bespamyatnov, Jason Sears, Jinseok Ko, John Liptac, Kelly Smith, Kenneth Marr, Laurence Lyons, Liang Lin, Marco Ferrara, Matthew Reinke, Nathan Howard, Noah Smick, Rachael McDermott, Scott Mahar, and Vincent Tang.

Finally, I would like to thank my parents Sue and Paul, my brother Daniel and the entire MacDonald clan who collectively make up my family in the truest sense of the word.

Contents

List of Figures

THIS PAGE INTENTIONALLY LEFT BLANK

List of Tables

THIS PAGE INTENTIONALLY LEFT BLANK

Chapter 1

Introduction

One of the fundamental problems facing the magnetic confinement fusion community is the reduction in performance associated with plasma turbulence. In present experiments, turbulence is the limiting factor on temperature and density gradients which in turn limit the rate of fusion energy production. Although much remains to be done, progress has been made both theoretically and experimentally on understanding and characterizing this turbulence.

An example of this improved understanding is the recognition of the importance of rotation on plasma performance. Strong plasma rotation can help stabilize destructive magneto-hydrodynamic instabilities (resistive wall modes, RWMs [1], [2]) while gradients in rotation can improve confinement by suppressing turbulence[3],[4]. In many experiments the rotation profiles associated with improved performance are generated through the use of neutral beam injection (NBI)[5]. Unfortunately this approach may prove impractical in the large, high density plasmas envisioned for next generation devices such as ITER [6], [7]. As a result, there is a need to develop alternatives to NBI for driving strong plasma rotation. Significant self generated flows have been observed on a number of tokamaks [8] suggesting that it may be possible to reap the benefits of rotation without the use of NBI. Furthermore, chapters 7 and 8 of this thesis discuss recent observations of significant flow drive by wave heating.

While these alternative approaches to flow generation have been receiving increased study in recent years, they remain poorly understood theoretically and sparsely

measured experimentally. This paucity of measurement can be explained by the fact that the standard method for measuring rotation profiles is active charge exchange spectroscopy with NBI. The neutral beams involved generally represent large sources of external momentum making it very difficult to study intrinsic flows. Passive x-ray spectroscopy has been used to diagnose intrinsic rotation without the use of perturbative beams but is often limited to a just of few line-integrated measurements.

To address the need for rotation profile measurements without the use of neutral beams, a new type of x-ray crystal spectrometer has been developed. This instrument combines the passive nature of standard x-ray spectroscopy with the ability to make spatial resolved measurements. The contents of this thesis are divided between two broad themes. The first involves the theory and design of imaging x-ray crystal spectrometers. The second deals with plasma flows experiments made possible by the expanded diagnostic capabilities of the new instrument.

1.1 Outline

This thesis is divided into 9 chapters and 7 appendices. The topic of imaging x-ray crystal spectrometers is addressed in chapters 2, 3 and 4. Specifically, chapter 2 summarizes the physics of such an instrument and how to go about designing one. Chapter 3 describes the imaging x-ray crystal spectrometer that was designed and built to obtain the data for the second half of this thesis. Chapter 4 describes how plasma parameters can be inferred from the line emission spectra the aforementioned spectrometer was designed to measure.

Chapters 5 through 8 focus on the study of tokamak plasma flows in the absence of external momentum input from neutral beams. Chapter 5 provides an overview of rotation theories and discusses them in the context of rotation measurements made to date. Chapter 6 describes intrinsic rotation in enhanced confinement regime plasmas. Chapters 7 and 8 cover recent measurements of rotation drive by lower hybrid waves and mode converted ICRF[1] waves, respectively. The final chapter, Chapter 9, briefly summarizes the key findings of the thesis and outlines some possible directions for

[1] Ion cyclotron range of frequency

future work. Appendix A provides details on the line emission spectra of hydrogen- and helium- like argon. Appendix B outlines the calculation of the x-ray transmission through the helium-air mixture present in the spectrometer housing. Appendix C consists of calculations of interspecies thermal equilibration times. This appendix also provides evidence of the strong thermal coupling between impurity and bulk ions in Alcator C-Mod plasmas and discusses the conditions under which temperature separation between ions and electrons is to be expected. Appendix D covers the concept of instrumental temperature and describes a novel technique for determining the resolving power of a spectrometer. Appendix E discusses the separation of ion and impurity parallel flows in tokamak plasmas. Appendix F provides a summary of the variables used in the multi-machine intrinsic rotation database as well as derivations of approximate expressions for the average ion mass, and the acoustic sounds speed. Appendix G discusses how toroidal rotation can be generated through asymmetries in momentum diffusivity.

1.2 The Alcator C-Mod Tokamak

The spectrometer that is the focus of the first part of this thesis was installed on the Alcator C-Mod tokamak at the MIT Plasma Science and Fusion Center. Alcator C-Mod is a compact tokamak designed to operate at the high magnetic field and densities envisaged for burning plasmas on reactors such as ITER and DEMO. Figure 1.1 shows isometric and cross sectional views of the device while table 1.1 summarizes its key parameters.

Alcator C-Mod is the ideal device for conducting research on the twin goals of this thesis, namely the development of high resolution imaging x-ray spectroscopy and intrinsic rotation studies. High resolution x-ray spectroscopy is made easier by the enormous amount of line radiation emitted by the high density discharges produced on Alcator C-Mod [2]. Furthermore Alcator C-Mod does not use NBI for heating which allows for the study of intrinsic plasma rotation on every discharge.

[2]For a fixed impurity fraction, radiated power is proportional to the square of electron density

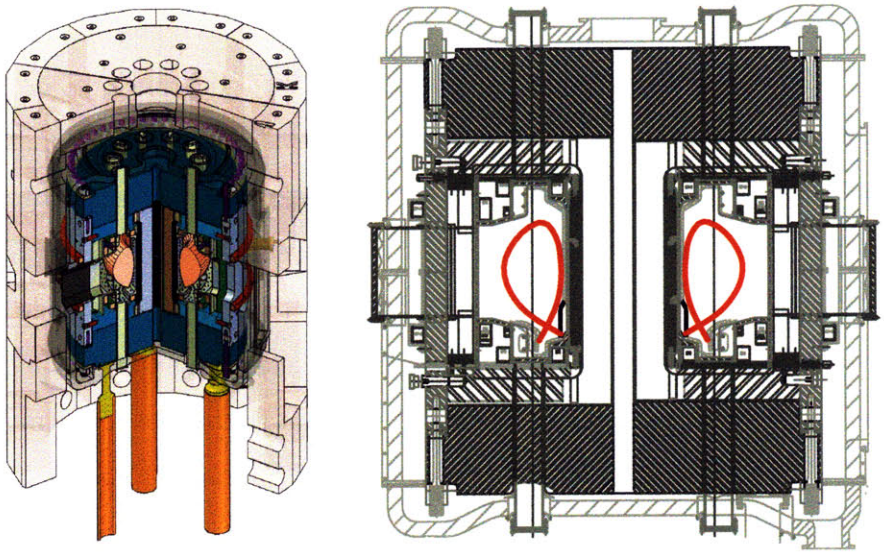

Figure 1-1: The Alcator C-Mod tokamak

1.3 Units

The units used throughout this thesis are in the system international, SI, and specifically MKS. The one exception is that temperatures are quoted in electron volts (where 1eV $\sim$ 11,600 $°K$) since writing and reading sentences like "the plasma was heated to 60,000,000 $°K$" is somewhat cumbersome.

Table 1.1: Alcator C-Mod Facility Parameters

Parameter	**Value/Range**
Major Radius	R $\sim$ 0.68 m
Minor Radius	a $\sim$ 0.22 m
Plasma Volume	V $\sim 1m^3$
Plasma Surface Area	S $\sim 7m^2$
Maximum Toroidal Field	$B_T \leq 8$ T
Maximum Plasma Current	$I_p \leq 2$ MA
Elongation	$\epsilon \leq 1.9$
Triangularity	$\delta \leq 0.85$
Maximum Toroidal Field Pulse length	5 s >> τ_{CR}
Ion Cyclotron RF source Power	8 MW, 50 to 80 MHz
Lower Hybrid RF Source Power	3 MW, 4.6 GHz
Collisionality range	$0.05 < \nu^* < 10$
Normalized pressure	$\beta_N \leq 1.8$
Absolute Plasma Pressure	$\leq$ 0.2 MPa (volume average)

THIS PAGE INTENTIONALLY LEFT BLANK

Chapter 2

Imaging X-ray Crystal Spectrometers

High resolution measurements of line radiation from partially ionized atoms have been used to diagnose fusion plasmas for a number of years[9]. While this method has been successfully employed on a variety of experiments, its usefulness has been limited by the lack of spatial localization associated with the line integrated nature of the measurement.

The problem of spatial localization can be overcome if spectra from multiple lines of sight are available. The general problem of inferring local quantities from a set of line integrated measurements is not unique to plasma physics. Indeed, the entire discipline of tomography was developed to address it. The analytic methods required for performing spectro-spatial tomographic inversions of line emission spectra have been known for some time ([10], [11]). These techniques had not been applied to x-ray data, however, due to the difficulties associated with simultaneously measuring a large number of high resolution spectra, each with its own view through the plasma. Even a relatively modest tomographic scheme requires of order 10 lines of sight. If a separate spectrometer is required for each line of sight, then these requirements become extremely onerous in port space, funds and labor.

In their 1999 paper, B.S. Fraenkel and M. Bitter [12] proposed a novel solution to this problem. By using a spherically bent crystal and a 2d x-ray detector arranged

in the Johann configuration [13], it is possible to obtain multiple lines of sight from a single spectrometer. Early attempts to implement such a solution were frustrated by the lack of a large area x-ray detector capable of handling the high count rates necessary for useful measurements of rapidly evolving plasmas [14]. Recently, however, just such a detector was developed at the PSI in Switzerland. It is this dramatic improvement in x-ray detector technology that has made high resolution imaging x-ray spectroscopy of fusion plasmas practical.

This chapter will describe various concepts and considerations essential to the design of a high resolution image x-ray crystal spectrometer.

2.1 Bragg Reflection

X-ray crystal spectrometers are based on the principle that the regular spacing of atoms in a crystal lattice can be used as a diffraction grating. Bragg reflection takes place when the distance traveled by photons reflecting off adjacent layers of a crystal is an integral multiple of the photon wavelength. This gives rise to constructive interference of the reflected waves as shown figure 2-1. From this diagram one can readily derive the famous Bragg condition:

$$n\lambda = 2d \sin\theta_b \tag{2.1}$$

This expression relates the resonant angle, θ_b, to the wavelength of the photons, λ, the inter-atomic spacing of the crystal, d, and the order of reflection, n. The inter-atomic spacing of crystals is typically a few angstroms[15]. Figure 2-2 shows how a flat crystal, a slit and a position sensitive x-ray detector can be arranged to form a spectrometer (angles have been exaggerated for illustrative purposes).

Note that all the photons reaching a given point on the detector have the same Bragg angle. Since there is a one-to-one correspondence between θ and λ via the Bragg condition, it follows that the intensity measured at a point on the detector is from photons of a specific wavelength.

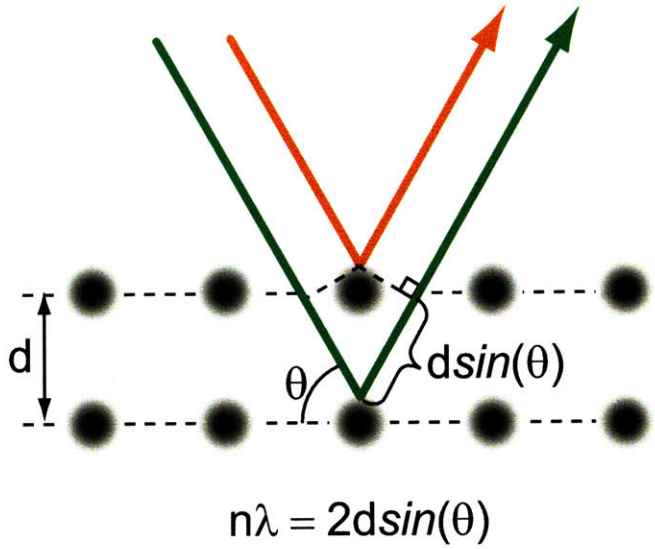

Figure 2-1: Bragg Reflection

Even for a perfectly unblemished crystal, the infinitely precise one-to-one relation between λ and θ_b implied by the Bragg relation is only approximate. In reality, there is a small range in angle for which there is significant constructive interference. This fact is illustrated in what has come to be known as a rocking curve [16]. The rocking curve plots reflected intensity against the deviation angle from the wavelength given by the Bragg condition. An example rocking curve for a calcite crystal is shown in figure 2-3.

The narrower the width of the rocking curve, the sharper the resonance. In figure 2-3 we see that the rocking curve has a full width at half maximum (FWHM) of $\sim$15 arc seconds. As will be seen in the next section, the finite width of the rocking curve can often be neglected when dealing with bent crystal spectrometers due to the inherent focusing imperfections of spherical mirrors.

2.2 Johann Spectrometers

Although the arrangement depicted in figure 2-2 is easy to implement, it suffers from two principal draw backs. Firstly, the presence of the slit significantly reduces throughput. Secondly, the spectrometer only provides a single line of sight. The

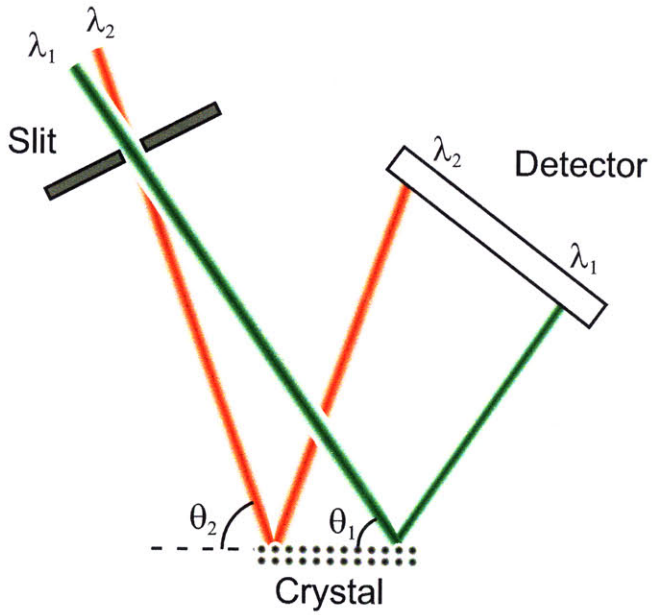

Figure 2-2: A simple flat crystal spectrometer

throughput problem can be resolved by bending the crystal in the plane of the spectrometer as shown in figure 2-4.

The dashed line in figure 2-4 is referred to as the Rowland circle and has a diameter equal to the radius of curvature of the crystal. Using simple geometric arguments it can be shown that all rays from a given point on the Rowland circle to any point on the crystal will have the same angle of incidence (with respect to the crystal surface). Due to the 1-to-1 relationship between angle of incidence and λ implied by the Bragg condition, each point on the Rowland circle will correspond to a specific wavelength. Unlike the flat crystal spectrometer described above, there is no slit in this arrangement which gives rise to greatly increased throughput. In the flat crystal spectrometer described previously, photons measured a specific location on the detector are reflected off only a small portion of the crystal. Therefore, variations in crystal quality can lead to distortions of the measured spectra. With a curved crystal, however, this problem is mitigated by the fact that any given point on the

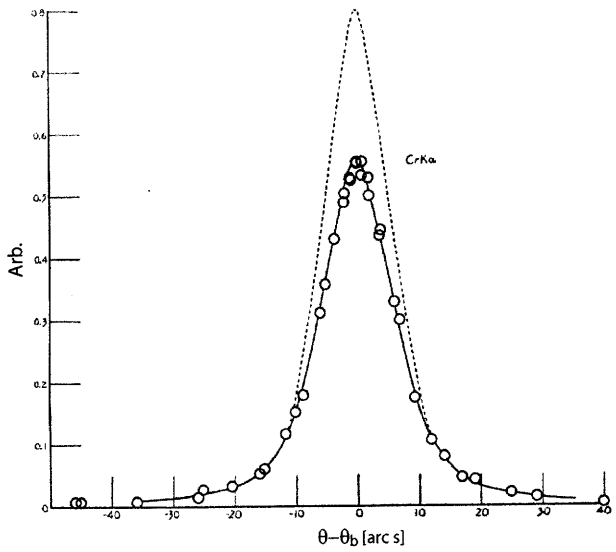

Figure 2-3: Rocking curve of a calcite crystal[17]. The dashed line shows a calculated rocking curve in which absorption by the crystal is neglected.

detector is measuring photons reflected by every part of the crystal. It should be noted that there are practical limitations on the minimum radius of curvature for a crystal. Although there is variation between crystal types, having a radius of curvature $\sim$ 1 m or less can lead to substantial broadening of the rocking curve. This limitation on the radius of curvature sets a lower bound on the size of bent crystal spectrometers.

2.2.1 Spherically Bent Crystal Optics

The spectrometer depicted in figure 2-4 provides only a single line of sight. If instead of a cylindrically bent crystal, a spherically bent crystal is used then the spectrometer will have spatial resolution in the meridional plane (i.e. the direction perpendicular to the spectrometer plane). In such a spectrometer all photons that arrive at the detector below the meridional plane must have originated above this plane and vice versa. The optical properties of spherical mirrors can be difficult to visualize due to the fact that the horizontal (meridional) and vertical (sagittal) focal lengths are different [18]. The meridional and sagittal focus are given by:

$$f_m = R_c \sin\theta_b \tag{2.2}$$

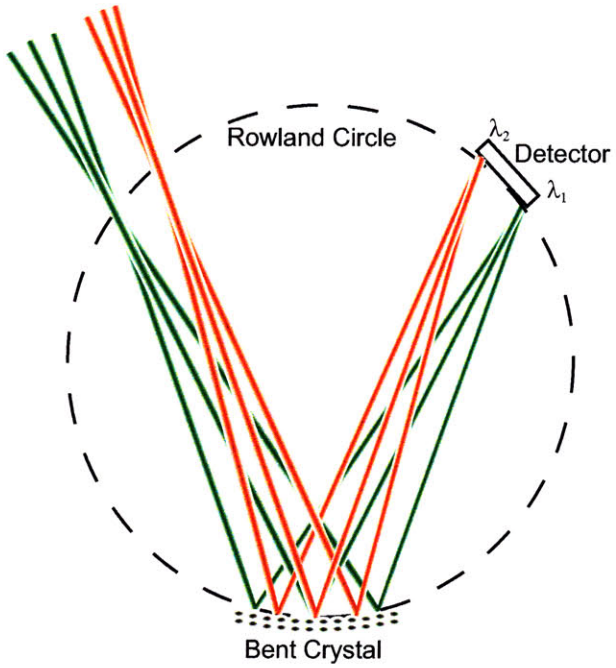

Figure 2-4: A singly bent Johann crystal spectrometer

$$f_s = -f_m / \cos 2\theta_b \tag{2.3}$$

where is θ_b the Bragg angle, R_c is the radius of curvature of the crystal and f_m and f_s are respectively, the meridional and sagittal focal lengths. An example of the peculiar focusing properties of a spherically bent mirror is depicted in figure 2-5.

2.2.2 Spatial Resolution

Figure 2-6 shows the spatial imaging properties of a Johann spectrometer. If the height of the crystal is doubled, so too is the height of the ray bundle at every point along the line of sight. From figure 2-6 it can be seen that the spatial resolution of a given spectrometer arrangement is approximately:

$$\Delta x = \frac{|f_s - L_{cp}|}{f_s} d \tag{2.4}$$

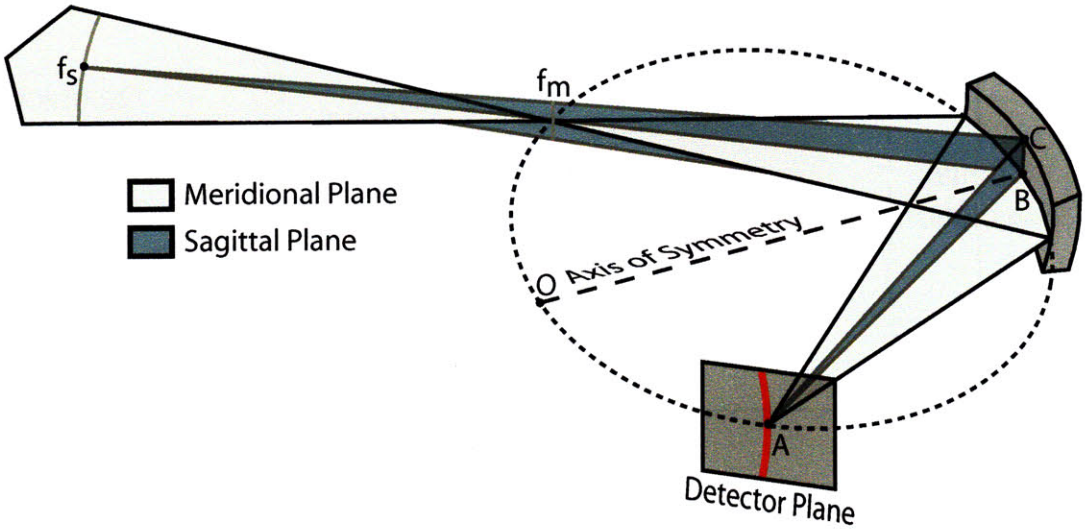

Figure 2-5: The spherically bent crystal optics of a Johann spectrometer. If the ray bundle is rotated about the axis of symmetry (OB), an ellipse will be traced out on the detector plane (red line).

Since the throughput of the spectrometer is proportional to the area of the crystal, there is a fundamental trade off between throughput and spatial resolution. For fixed crystal height the spatial resolution can be improved by having the meridional focus as close as possible to the plasma. This can be accomplished through judicious choice of the Bragg angle, crystal radius of curvature, and the distance between the plasma and the crystal.

From equation 2.3 we see that for Bragg angles less than 45°, the sagittal rays are diverging. If spatial resolution is important, diverging sagittal rays should be avoided, which argues for choosing a Bragg angle $> 45°$.

2.2.3 Detector Alignment

For optimal focusing, the x-ray detectors should be tangent to the Rowland sphere. Since the surface of x-ray detectors are generally planar, they cannot be tangent to the Rowland sphere everywhere. The detectors can be arranged to mitigate this focusing error by using the alignment scheme shown in figure 2-7.

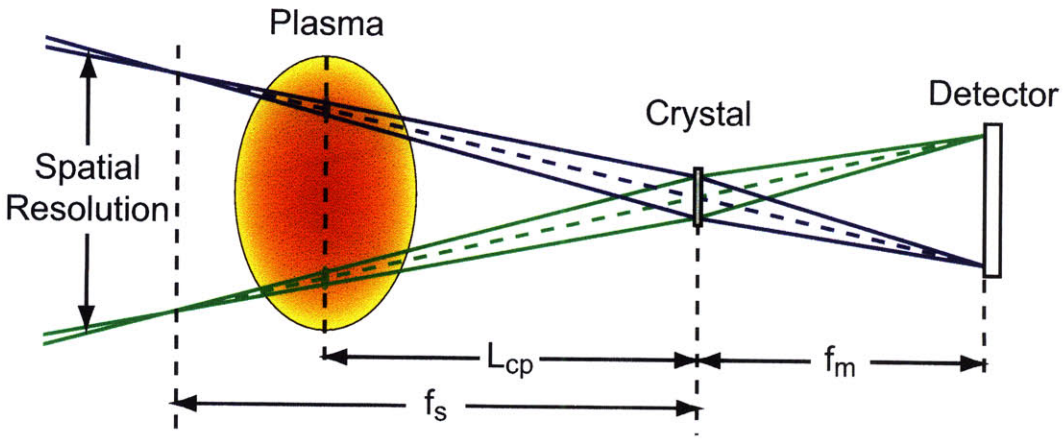

Figure 2-6: Spatial resolution for an imaging Johann spectrometer. The sagittal and meridional focal lengths (f_s and f_m) are given by equation 2.2 and 2.3. L_{cp} is the distance between the crystal and the plasma.

This figure shows a relatively straightforward way to arrange multiple planar detectors such that the center of each detector is tangent to the Rowland sphere. The wedge angle, α, can be determined from geometrical considerations and is given by $\alpha = 90 - \theta_b$.

2.2.4 Johann Error and Spectral Resolution

As mentioned in the previous section, the spherically bent crystals used in a Johann spectrometer do not perfectly focus all photons of a specified wavelength to a single point on the detector. This focusing imperfection gives rise to a limit on the spectral resolution of a Johann spectrometer referred to as the Johann error[19]. Physically the Johann error leads to spatial smearing of photons of a given energy on the detector. This is shown graphically in figure 2-8. The extent of this smearing can be calculated from figure 2-8 using straightforward geometric arguments and is given by[19]:

$$\delta x_j = \frac{l^2 cos\theta_b}{8R_c} \tag{2.5}$$

where, δx_j is the Johann error, l is the width of the crystal, θ_b is the Bragg angle and R_c is the crystal radius of curvature. This expression demonstrates that the

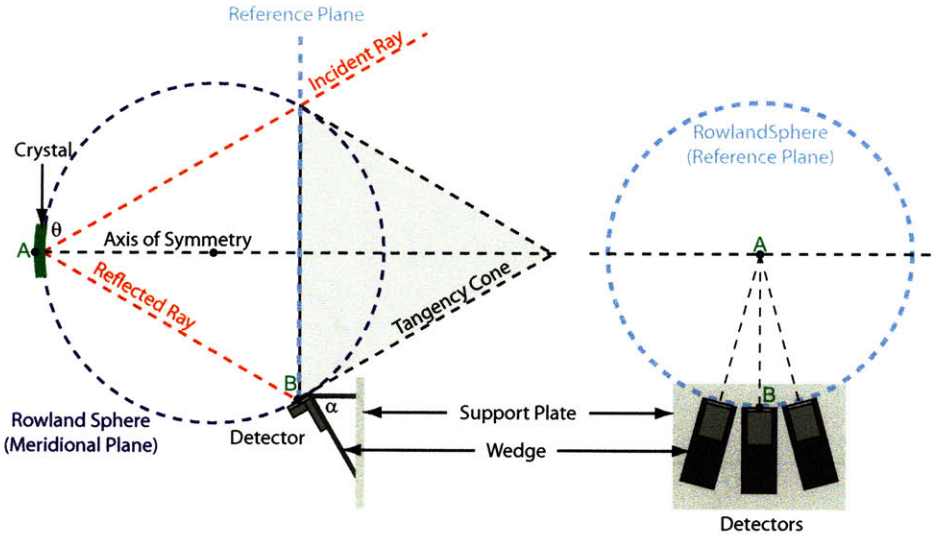

Figure 2-7: Optimal arrangement of 3 detector modules such that their centers are tangent to the Rowland sphere.

Johann error can be made arbitrarily small by reducing the width of the crystal. This illustrates a fundamental trade-off between throughput (proportional to the area of the crystal) and spectral resolution (inversely proportional to the width of the crystal). It is also worth noting that the Johann error is smaller at larger Bragg angles. Therefore, Bragg angles of greater than 45 ° have the dual benefit of reduced Johann error and enhanced spatial resolution.

The resolving power of a Johann spectrometer can also be influenced by the finite width of the detector's pixels. Clearly, if the pixel width, δx_p is much larger than δx_j, then the resolving power will not depend on the Johann error at all. If the pixel width and the Johann error are of similar magnitudes then their combined effect can be approximated by adding the two lengths in quadrature, i.e.

$$\delta x \approx \sqrt{(\delta x_j)^2 + (\delta x_p)^2} \tag{2.6}$$

Using the Bragg condition, it can readily be shown that the resolving power of a crystal spectrometer is given by

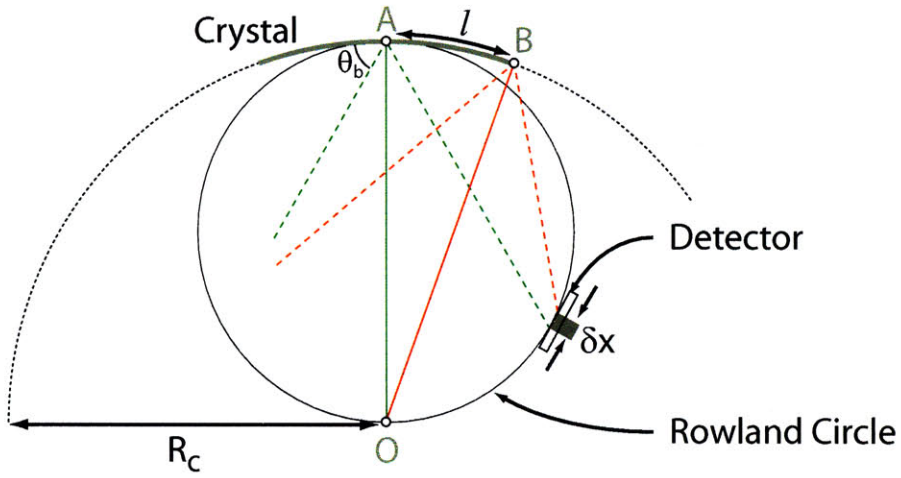

Figure 2-8: Geometric construction showing the origins of the Johann focusing error.

$$\frac{\lambda_o}{\Delta\lambda} = \frac{\tan\theta_b}{d\theta} \tag{2.7}$$

Making the substitution $\delta\theta = \delta x/f_m$ and plugging in the above expression for δx gives,

$$\frac{\lambda_o}{\Delta\lambda} = \frac{8}{\sqrt{1+(\delta x_p/\delta x_j)^2}}\left(\frac{R_c}{l}\tan\theta_b\right)^2 \tag{2.8}$$

For example, plugging in $R_c = 1.5m$, $\theta_b = 60\,°$, $l = 5cm$ and assuming a negligible pixel size gives a resolving power of ~20,000 [1].

2.3 Emission Line Selection

The design of a Johann spectrometer for diagnosis of a fusion plasma begins with the selection of the impurity emission lines to be measured. Noble gases are commonly chosen because they are chemically inert and their concentration in the plasma can

[1] For comparison the natural broadening of L_α for argon is $\lambda_o/\Delta\lambda = 2.04 \times 10^5$

be easily controlled. The choice of specific noble gas depends primarily on the temperature range of the plasma to be diagnosed. For any given impurity, the hydrogen and helium like charge states have relatively simple spectra with several well studied and strong emission lines. Furthermore, they tend to be the dominant charges states over a broad range in temperature. These properties make line emission from H- and He-like charges states ideal for spectroscopic analysis. Figure 2-9 shows the fractional abundance of the H- and He-like charge states in coronal equilibrium for helium, neon, argon and krypton as a function of electron temperature.

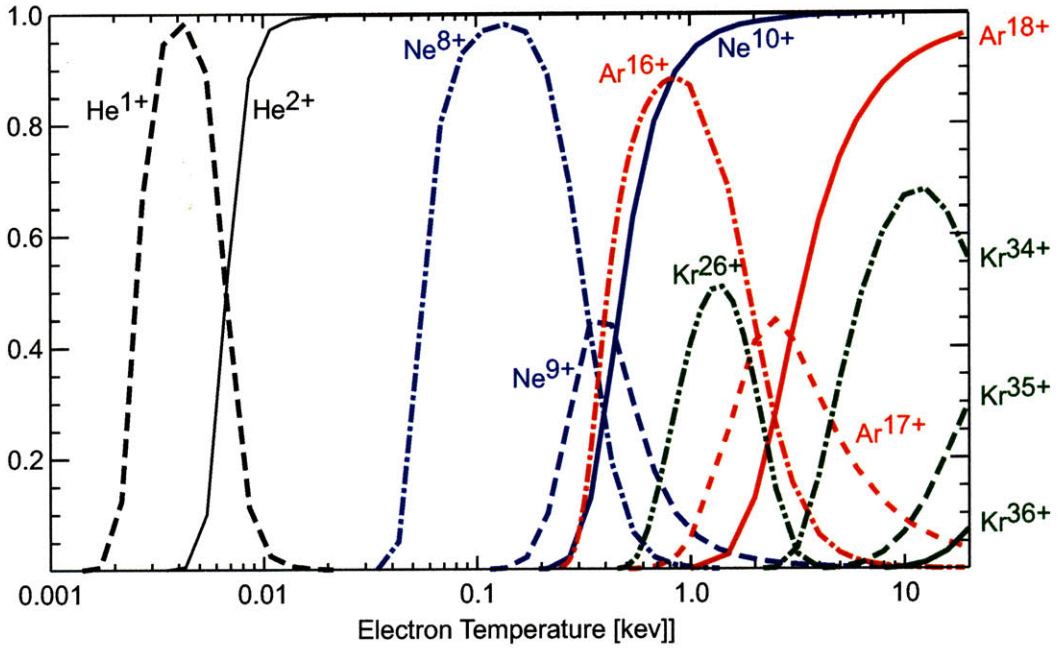

Figure 2-9: Fractional charge state abundances for various noble gases in coronal equilibrium. Fully stripped charge states are in depicted in solid lines, H-like in dashed, He-like in dash-dot and Ne-like in dash-dot-dot.

Figure 2-9 makes clear that for the temperature range of interest in Alcator C-Mod plasmas (0.5-6kev), neon is fully stripped except in the relatively cool edge region. Argon, on the other hand, has H- and He-like as the dominant charge states. Krypton could plausibly be used for diagnosing the core, but because of its relatively high atomic number ($Z_{Kr} = 36$, $Z_{Ar} = 18$) it is considerably more perturbative than argon for the same absolute density (it both radiates considerably more power, and

more significantly dilutes the ion density). These considerations make argon the ideal non-native diagnostic impurity species for Alcator C-Mod plasmas (The details of the H-, and He-like argon spectra are covered in appendix A).

2.4 Crystal Selection

Once the spectral range has been determined, the Bragg condition then sets a constraint on the relationship between the Bragg angle and the 2d spacing of the crystal to be used. To have the improved spatial resolution associated with converging meridional rays requires a Bragg angle greater than 45°. However, Bragg angles of more than $\sim 80\,^\circ$ become problematic because of interference of the incoming rays with the detectors (for a Bragg angle of $90\,^\circ$ the incoming and reflected rays are coincident). This range of $\sim 45\,^\circ < \theta_b < 80\,^\circ$ for the Bragg angles then imposes limits on the allowable 2d spacing of the crystal. Although the Bragg angle is a continuous variable and can take on any value in the range mentioned above, the available 2d spacing of suitable crystals is discrete. A fairly comprehensive list of commonly used crystals can be found in reference [15].

2.5 Chapter Summary

This chapter has outlined the basic physical principles underlying crystal spectroscopy in general and imaging Johan spectrometers in particular. The basic design process of such a spectrometer has been covered and can be summarized as follows:

- The temperature range influences the selection of trace impurity
- The impurity selection influences with wavelength region
- The crystal is chosen to accommodate the selected wavelength region
  - 2d spacing of the crystal sets the Bragg angle ($\theta_B < 45^{circle}$ for improved spatial and spectral resolution).

  - Height of crystal influences throughput and spatial resolution.
  - Width of crystal influences throughput and spectral resolution (through the Johann error)

- The choice of crystal radius of curvature sets the meridional and sagittal foci
  - Larger radius of curvature reduces magnification
  - Trade-off between spectral coverage and resolution

THIS PAGE INTENTIONALLY LEFT BLANK

Chapter 3

The Spatially Resolving High Resolution X-ray Spectrometer: Hirex-Sr

3.1 Design Criteria

An imaging x-ray spectrometer of the Johann type has been designed, built, installed and operated on the Alcator C-Mod tokamak. This instrument has been dubbed the Hirex-Sr spectrometer[1]. The goals of this project were to enhance the diagnostic capabilities of the Alcator C-Mod program and demonstrate the feasibility of using an imaging x-ray crystal spectrometer as a practical diagnostic for fusion plasmas. In order to accomplish these goals the spectrometer had to:

1. Image the entire plasmas cross section
2. Have sufficient signal to make measurements on a time scale shorter than the energy, momentum and particle confinements times (i.e. < 20 ms).
3. Have sufficient spectral coverage to measure emission lines in the range $3.94\mathring{A} < \lambda < 4.00\mathring{A}$ for measurement of He-like argon emission lines

[1]Hirex is a contraction of "HIgh REsolution X-ray", while Sr is a reference to its ability to make spatially resolved measurements

$3.72 < \lambda < 3.80$ for measurement of H-like argon emission lines

4. Have sufficient spectral resolution to measure the minute Doppler shifts of emission lines associated with plasma rotation down to the km/s range ($\lambda/\Delta\lambda \sim$ 10,000).

5. Have a spatial resolution of $\sim$ 1 cm to capture the subtleties of radial variation in Alcator C-mod plasmas.

3.2 Design Constraints

All design projects are fundamentally about managing constraints and making trade offs between competing requirements. As has already been mentioned, there are fundamental trade offs between spatial, spectral and temporal resolution. Furthermore, the design of the spectrometer was significantly constrained by the shape and size of Alcator C-Mod ports, as well as the available space in and around the reactor. Given the constraints summarized above, it was determined that separate pairs of crystals and detectors would be needed for the two spectral ranges of interest (i.e. one crystal-detector pair for the He-like argon spectra and another for the H-like argon spectra). In effect this meant designing two separate spectrometers contained in a single housing.

The requirement to image the entire plasma cross section meant using one of the 10 racetrack shaped radial ports on Alcator C-Mod. This however, was at odds with the desire to give the spectrometer a line of sight with a large tangential component to allow for measurement of toroidal rotation. Furthermore the spectrometer had to be designed in such a way that it did not interfere with existing diagnostics. To allow for a greater understanding of the complex relationship between the many trade offs involved in the spectrometer design, specialized software was written. This software package used dozens of design decisions as inputs and calculated the resulting spectrometer layout and performance metrics. It was also capable of performing ray tracing calculations to identify interferences between the spectrometer lines of sight

and other diagnostics in the tokamak. This code made it possible to compare hundreds of competing designs and select the one that satisfied all the spatial constraints while maximizing the spectrometer's performance characteristics. Figure 3-1 shows the layout of the final spectrometer design and how it interfaces with Alcator C-Mod.

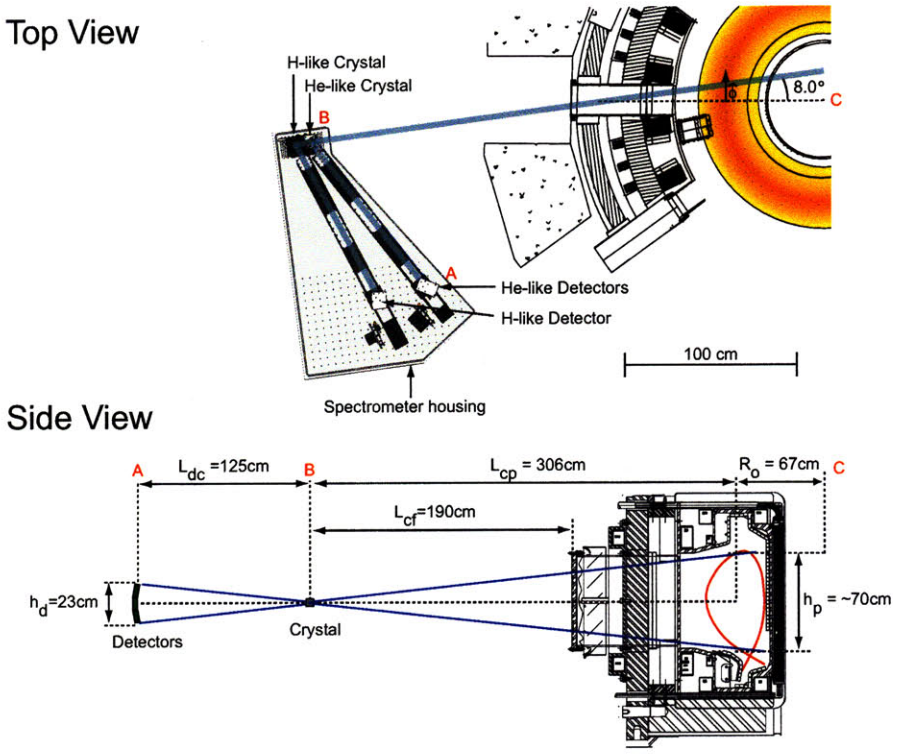

Figure 3-1: Top view a), and side view b), of the Hirex-Sr spectrometer as installed on Alcator C-Mod

Although the central view of the spectrometer is only 8° off-radial, the toroidal component of the line of sight is sufficient to make toroidal rotation measurements. Having views of both the top and bottom of the plasma cross section makes it possible to distinguish between line shifts caused by poloidal and toroidal rotation.

3.3 Component Descriptions

The following section provides a detailed description of the critical components of the imaging x-ray crystal spectrometer.

3.3.1 Crystals

For both the H-like and He-like spectrometers, (102)-quartz was chosen as the dispersive elements. This crystal cut has a precisely known 2d spacing of $4.56215\mathring{A}$ which gives Bragg angles of 55.5° and 60.5° for the H-like and He-like spectrometer, respectively. In addition to having a convenient 2d spacing, (102)-quartz is relatively inexpensive, has good bending properties and high reflectivity. To achieve the desired radius of curvature, a glass substrate is ground and polished to the appropriate dimensions. When the relatively thin (~0.15 mm) quartz crystal is placed on the substrate, it is bent to the same radius of curvature as the substrate and is held in place via contact forces. The H-like crystal has a diameter of 50 mm and a radius of curvature of 1385 mm, while the He-like crystal is rectangular (64 mm in width, 27 mm in height). Some of the specifications/properties of the H-like crystal assembly are summarized below:

Table 3.1: Crystal Specifications

Diameter	$50mm$
Spherical curvature	$1300 \pm 20mm$
Substrate thickness	$30 \pm 1mm$ on the edge
Quartz Thickness	0.15 ± 0.01 mm
Quartz surface parallelism	< 10 arc sec
Contacting voids	$< 20\%$ crystal area

3.3.2 X-ray Detectors

A total of four Pilatus [20] 100k x-ray detector modules are used in the spectrometer, three to image the He-like spectra and one for the H-like spectra. Each module

consists of a 487 × 196 array of x-ray sensitive hybrid-pixels (0.172 mm × 0.172 mm) operating in single-photon counting mode. Each pixel acts as a single channel analyzer with a low level discriminator and its own 20 bit counter, allowing each pixel to perform photon counting at rates up to 1 MHz. This approach gives rise to a dynamic range and maximum count rate many orders of magnitude higher than is possible using conventional x-ray CCDs or multi wire proportional counters. Count rates of up to $\sim 1 \times 10^5/s$ have been measured on pixels exposed to line radiation from centrally viewing chords, while combined count rates for the three He-like viewing modules as high as $1 \times 10^9/s$ have been recorded. For comparison, a recently constructed state-of-the-art 2D multi-wire proportional counter [21] has a maximum count rate of $\sim 5 \times 10^5/s$ over an area of $10cm \times 30cm$.

The thermal noise that gives rise to dark current in conventional detectors is at energies well below the lower level discriminator threshold. As a result, this thermal noise does not increment the pixel counters and no dark current is recorded. The detectors were fabricated in the UMC (Taiwan) 0.25 micron radiation tolerant process [22]. Unpublished tests have demonstrated that the devices show no significant degradation after exposures to well beyond 10 MRad of 8 keV x-rays. All the modules can be read out simultaneously in less than 3ms, which allows for a frame rate of 200 Hz at a 40% duty cycle. The key detector specifications are summarized in the table below.

3.3.3 Detector Mounting

The spatial and viewing constraints imposed by other diagnostics and the reactor meant that the detector modules were not quite wide enough to image the entire He-like argon spectrum using the alignment scheme described in the previous chapter. The full spectrum could be imaged, however, if the detectors were arranged in the manner shown in figure 3-3.

This figure shows how the detector arrangement can be modified to increase the acceptance angle of the detector (and hence increase the spectral coverage). The increased spectral coverage comes at the cost of an increase in focusing error. In this

Table 3.2: Detector Specifications

Sensor Type	Reverse biased silicon diode array
Sensor Thickness	320 μm
Pixel Size	$172\mu m \times 172\mu m$
Format	$487 \times 195 = 94,965$ pixels
Area	$83.8mm \times 33.5mm$
Dynamic Range	20 bits (1:1,048,576)
Count Rate Per Pixel	$> 2 \times 10^6$ x-rays/s
Energy Range	3-30 keV
Energy Resolution	$\sim$ 500eV
Adjustable Threshold range	2-20 keV
Readout Time	2.7 ms
Maximum Frame Rate	300 Hz
Point Spread Function	1 pixel
External Trigger/gate	5V TTL
Power Consumption	15 W
Dimensions	$275 \times 146 \times 85mm$
Weight	1 kg

particular case, the advantage of imaging the entire He-like argon spectra warrants the modest reduction in spectral resolution associated with this alternative detector arrangement. 3D CAD drawings and a photograph of the mounting structure for the He-like detectors is shown in figure 3-4. This alignment gives rise to the slight gaps between detector visible in figure 3-4.

3.3.4 Alignment Stages

The crystals and detectors require alignment with sub millimeter precision. This was accomplished through a combination of manual and computer controlled positioning stages, a summary of which is given in table 3.3.

3.3.5 Base Plate & Housing

All of the spectrometer's optical components and detectors are mounted directly onto a 1" thick aluminum base plate. This base plate was precision planed and serves

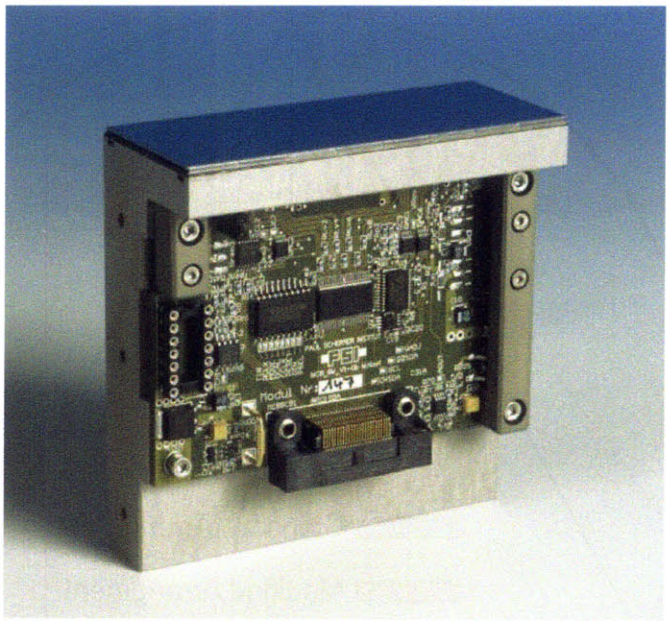

Figure 3-2: A single Pilatus 100k x-ray detector module

as an optical table to allow for the precise alignment of the spectrometer's optical components. Although this spectrometer was optimized to measure spectra of H- and He-like argon, the base plate was designed to allow for a wide range of Bragg angles ($45\,° < \theta_b <\sim 65\,°$, see figure 3-5).

For the energy range of interest ($\sim 3keV$), x-rays are strongly attenuated by air. Conventionally this problem is overcome by evacuating the spectrometer housing, however, due to the large size of the spectrometer a vacuum housing would have been extremely bulky. Furthermore, operating in vacuum would put a great deal of stress on the baseplate complicating optical alignment. To avoid these problems the spectrometer was designed to operate in a helium atmosphere. For the average path length through the spectrometer ($\sim$ 1.2 m), a mixture of 99% helium and 1% air absorbs about 20% of the incident $\sim$ 3 keV x-rays. More details on this topic can be found in appendix B. To minimize the level of air impurity, helium is continuously flowed through the spectrometer at a slight over pressure. This ensures the helium

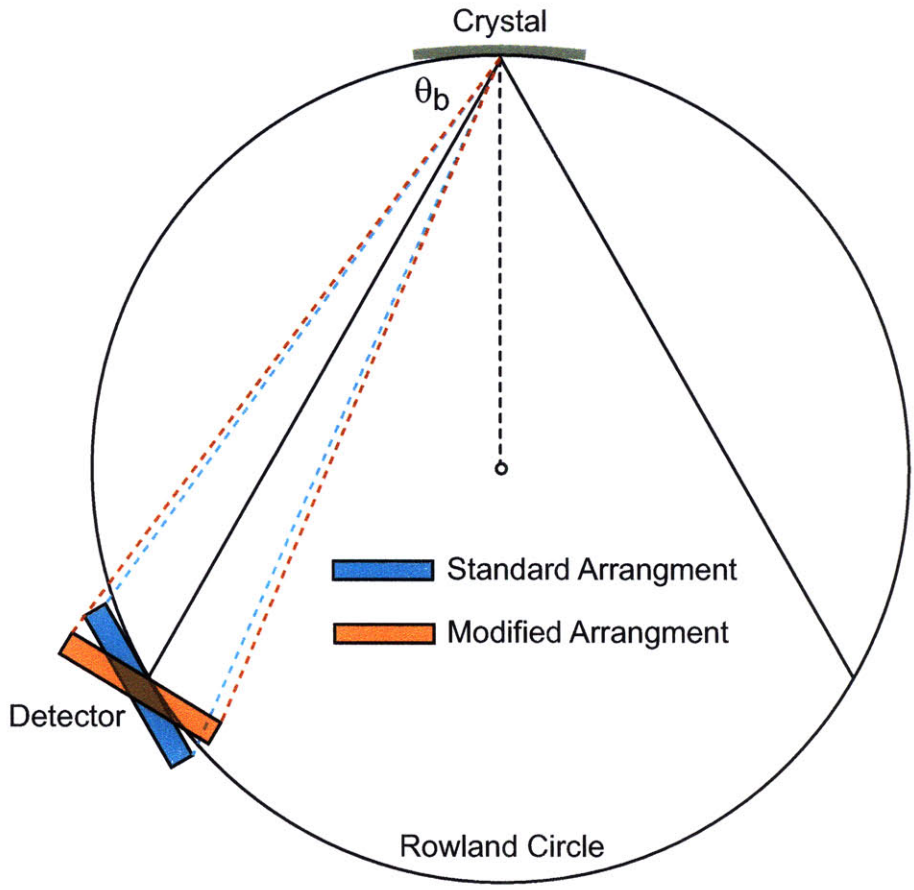

Figure 3-3: Modified detector arrangement to increase spectral coverage

will be flowing out of any leaks in the housing (as opposed to air leaking in). The seal between the housing and the base plate is provided by a single O-ring that lies in a groove machined into the base plate (see figure 3-6).

The helium inflow valve is located at the top of the housing while the out flow valve is located at the bottom. Since helium is lighter than air this arrangement does not require an inefficient "pump and purge" approach to obtaining a high purity He environment. In practice it was possible to reduce the air impurity to $< 1\%$ with only slightly more than one replacement volume of helium. In addition to the helium flow valves, the spectrometer housing was fitted with a release valve to guard against over pressurization. The spectrometer lid has 4 ports that allow for access to the various internal components, electronics feedthroughs and the mounting of an isolation glove.

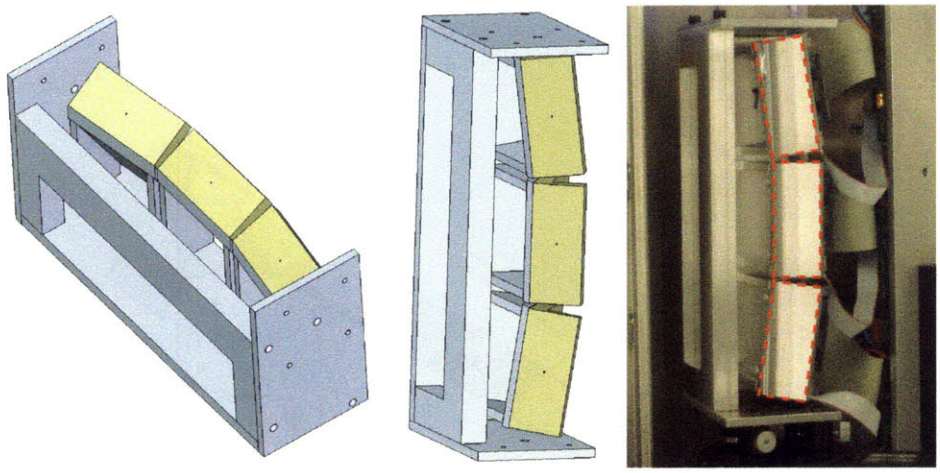

Figure 3-4: CAD drawings and a photograph of the He-like argon detectors and their support structure.

Table 3.3: Alignment Stages

Component	**Direction of Motion**	**Control Type**	**Comments**
Crystals	Vertical	Manual	Vertical alignment control
	Yaw	Computer	Bragg Angle control
	Pitch/Roll	Manual	Vertical angular alignment control
Detectors	Vertical	Manual	H-like module only
	Horizontal	Computer	Controls crystal-detector distance
	Yaw	Computer	Controls tangency to Rowland Circle

3.3.6 Spectrometer-Reactor Interface

A beryllium window is used to separate the ultra high vacuum environment of the fusion reactor from the helium atmosphere of the spectrometer. Beryllium was chosen for it high strength and excellent x-ray transmission characteristics. The beryllium window is 4" in diameter and 0.001" thick. This window is mounted on a 0.02" thick beryllium hexagonal support grid which is in turn mounted on 6" stainless steel conflat flange. It has been calculated that this window has a transmission coefficient of $\sim$ 40 % for 3.1 kev x-rays.

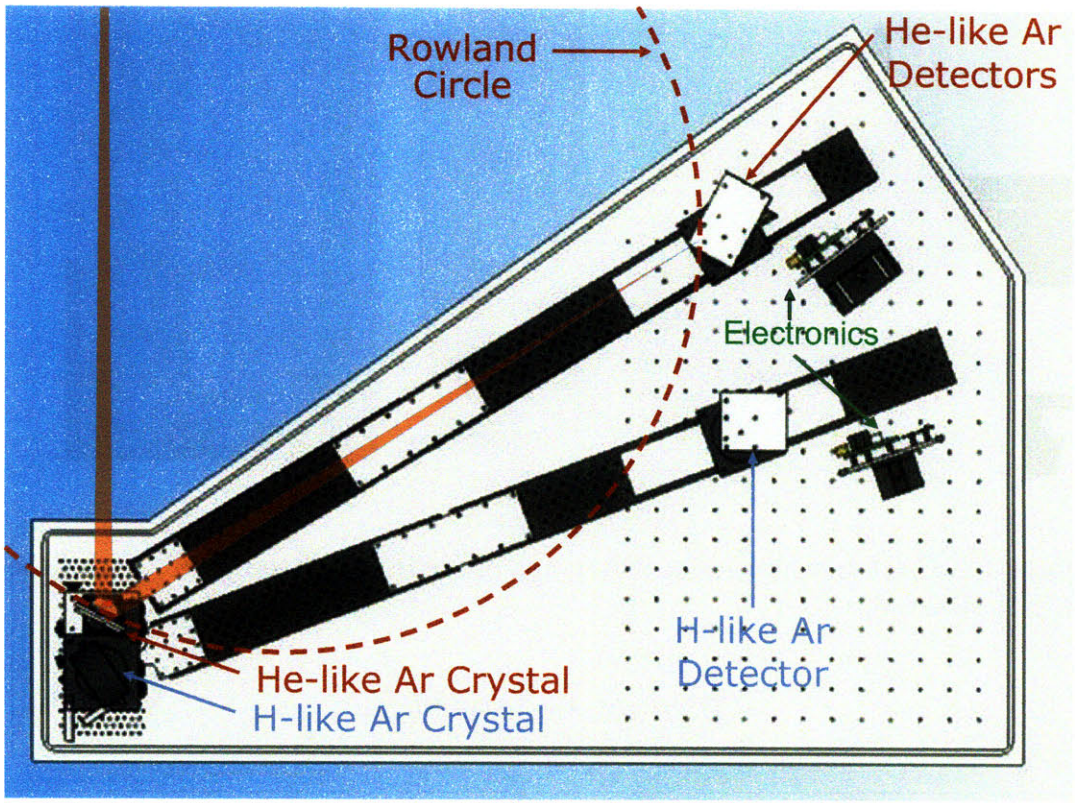

Figure 3-5: A top down view of the spectrometer showing all of the optical components and their arrangement on the base plate.

An engineering drawing of the window assembly is shown in figure 3-7. This assembly is leak tight to 1x10e-9 std cc/sec He, is bakeable to 150°C, and capable of supporting a differential pressure of 1 atm from either side.

In the event of a sudden failure of the Be-window, the helium from the spectrometer would rush into the reactor. This could both damage the spectrometer and lead to air contamination of the reactor. To guard against this possibility a 10" gate valve was installed between the beryllium window and the reactor. The gate valve was programmed to close when the local pressure rose above 10 mTorr. Figure 3-8 shows a CAD drawing of the spectrometer as installed on B-port.

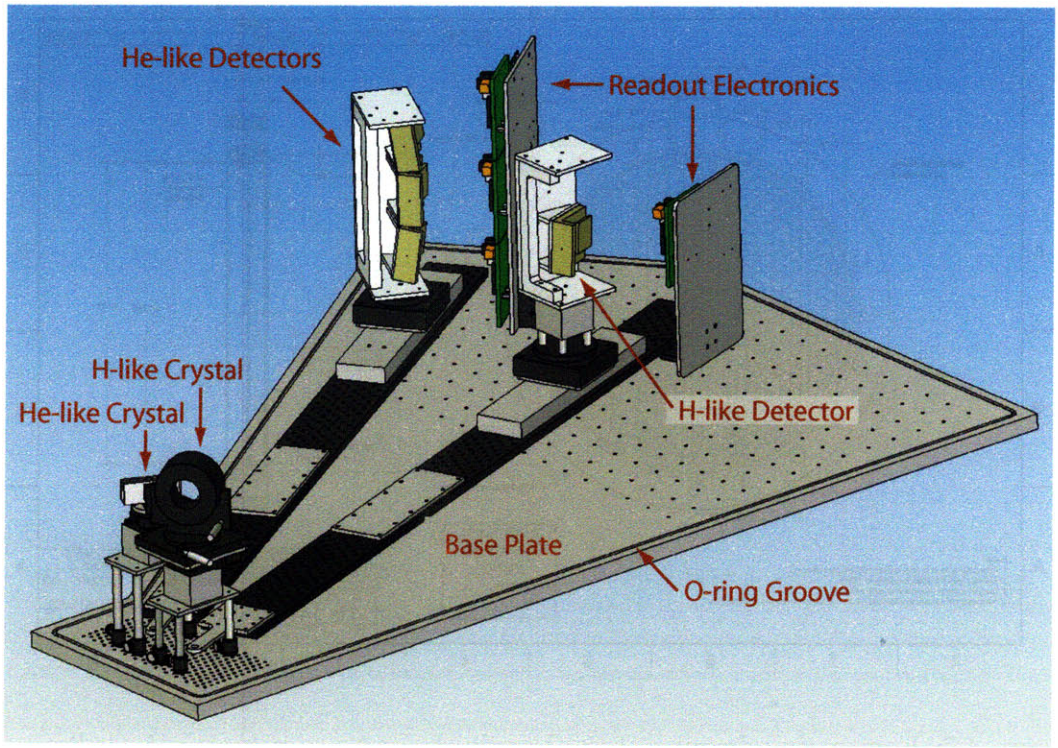

Figure 3-6: Isometric view of the spectrometer's optical components

3.4 Chapter Summary

This chapter has given a brief overview of a prototype high resolution imaging x-ray crystal spectrometer that has been installed on the Alcator C-Mod tokamak. This spectrometer is the most technologically advanced of its kind ever built, and (as will be described in the next chapter) the first capable of producing tomographically inverted profiles of various plasmas parameters.

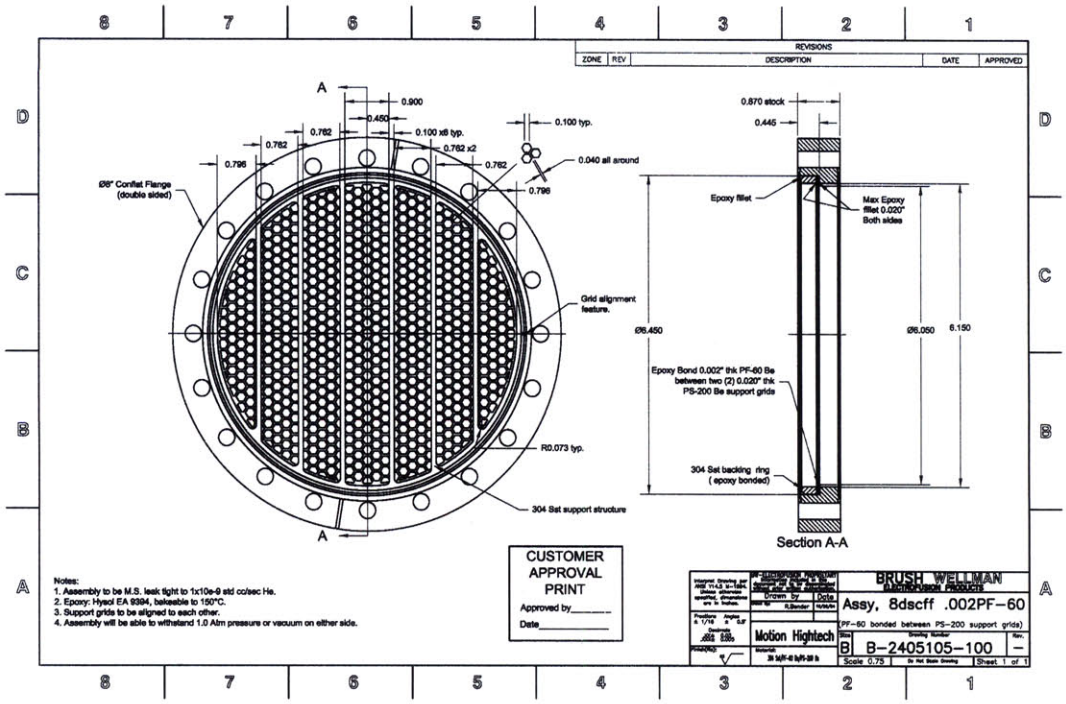

Figure 3-7: Engineering drawing of the beryllium window separating the helium atmosphere of the spectrometer from the vacuum environment of the reactor.

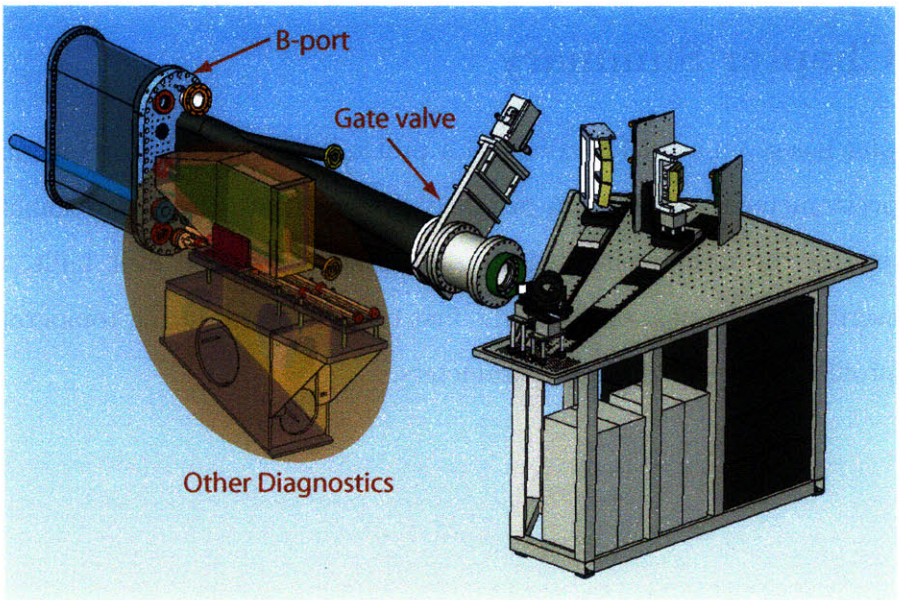

Figure 3-8: The Hirex-Sr spectrometer on B-port

Chapter 4

Inferring Plasma Parameters from Line Emission Radiation

The previous chapter was concerned with how a spherically bent crystal spectrometer can be used for high resolution measurement of line emission. This chapter will focus on methods used to infer various plasma parameters based on line emission spectra.

4.1 Doppler Shifts

When an electron transitions from an excited state to a lower energy level a photon is emitted. The frequency of this photon is proportional to the difference in energy between the initial and final state of the transitioning electron. If the emitting atom is moving with respect to the spectrometer, then the wavelength of the measured photon will be Doppler shifted such that

$$\lambda_m = \sqrt{\frac{1+v/c}{1-v/c}}\lambda_o \tag{4.1}$$

where λ_m is the measured wavelength, λ_o is the rest wavelength, c is the speed of light in vacuum and v is the relative velocity between the source & detector.

For the temperature range of interest in Alcator C-Mod plasmas ($< 6keV$) the thermal speeds of ion and impurities are of order a 100 km/s. Since these speeds are

much less than c the following non-relativistic approximation to equation 5.16 can be used

$$\frac{\Delta\lambda}{\lambda_o} = \frac{v}{c} \tag{4.2}$$

where $\Delta\lambda$ is the difference between the measured and rest wavelengths. The speed of light is so large that even seemingly high velocities of order 10km/s give rise to very small fractional changes in frequency, hence the need for high resolution spectroscopy.

Equation 4.2 indicates that there is a one-to-one correspondence between wavelength and velocity. Therefore the shape of an emission line spectrum provides a direct measurement of the distribution function of the emitting atoms in the direction along the line of sight of the spectrometer. By taking moments of this distribution function one can calculate the density, velocity and temperature of the population of emitting atoms using the following equations,

$$n = \int f(\vec{v}) d^3\vec{v} \tag{4.3}$$

$$\vec{V} = \frac{1}{n} \int \vec{v} f(\vec{v}) d^3\vec{v} \tag{4.4}$$

$$T = \frac{2}{3n} \int m v^2 f(\vec{v}) d^3\vec{v} \tag{4.5}$$

where f is the distribution function, n is the density, $\vec{V}$ is the fluid velocity, and T is the scalar temperature. It would be highly desirable to have such information for the bulk hydrogen in a fusion plasma. Unfortunately, since hydrogenic species have only one proton, they can not be simultaneously magnetically confined and have a bound electron. One way to circumvent this problem is to inject a small amount of impurity atoms into the plasma. Since impurity atoms can be partially ionized it is possible for them to be both magnetically confined (due to their net positive charge) and still have bound electrons that will give rise to line emission.

4.2 Line Ratio Measurements

For the range of temperatures and densities in tokamak plasmas the emissivity of a given line can often be approximated by:

$$\epsilon = \sum_i n_i n_e F_i(T_e)[ph/m^3/s] \tag{4.6}$$

where ϵ is the emissivity of the line, n_e is the electron density, n_i is the density of the i^{th} charge state and F_i is a function that captures the electron temperature dependence associated with all the atomic physics processes that give rise to the excited states in question. If the emissivity of an emission line is dominated by a single charge state then equation 4.6 simplifies to

$$\epsilon \cong n_i n_e F_i(T_e) \tag{4.7}$$

If two lines can be found for which the emissivity is dominated by the same charge state then the ratio of their emissivities is give by

$$R = \frac{\epsilon_1}{\epsilon_2} \approx \frac{n_i n_e F_1(T_e)}{n_i n_e F_2(T_e)} = F(T_e) \tag{4.8}$$

In such cases the dependence on charge state density cancels and the ratio only depends on the functions F_1 and F_2 both of which are functions of only electron temperature. These functions can be determined by atomic physics modeling and are well known for many atomic systems over a wide range in temperatures. If there happens to be a one-to-one relationship between R (the ratio of the local emissivities) and T_e then it is then possible to infer the electron temperature.

This approach can be generalized by taking the ratio of sums of lines that all depend on the same charge state. For example:

$$R = \frac{\sum_j \epsilon_j}{\sum_k \epsilon_k} \approx \frac{\sum_j F_j(T_e) n}{\sum_k F_k(T_e) n} = \frac{\sum_j F_j(T_e)}{\sum_k F_k(T_e)} \tag{4.9}$$

Again, the ratio R depends only on known functions of T_e. These measurements have typically lacked accuracy because they are often based on the ratio of the line averaged emission instead of the ratio of local emissivities. By using the ratio of the local emissivities determined by a tomographic inversion (described in the next section), it is possible to make measurements of the electron temperature much more accurately than would otherwise be possible.

4.3 Data Analysis

The previous two sections describe how information about a plasma can be inferred by the line radiation that it emits. There are many steps, however, that are required to extract local plasma parameters from the raw spectral data. These steps are: wavelength calibration, multi-line fitting, and spectral tomography, brief summaries of which are given below.

4.3.1 Wavelength Calibrations

Due to the nature of spherically bent crystal optics, lines of constant λ trace out elliptical curves on the detector plane (see figure 4-1). This curvature results from the intersection of the Bragg cone of a given wavelength with the planar surface of the x-ray detector modules. The first step toward calculating plasma parameters from raw spectra is correcting for this curvature, i.e. obtaining a spectral calibration. The standard way to calibrate a spectrometer is to expose the instrument to a radiation source with 2 or more lines of known wavelength in the spectral range of interest. The location of the lines on the detector can then be used to define a wavelength calibration.

The lack of convenient x-ray sources in the wavelength regions of interest (3.1 keV) requires that the plasma itself be used as a calibration source. Wavelength calibrations are obtained by running locked mode discharge in which non-rotating tearing modes act as a brake on toroidal rotation[23]. In the absence of rotation, emission lines are not Doppler shifted and an accurate spectral calibration can be

obtained by using previously published wavelength of known emission lines. That the locked mode breaking drives the toroidal rotation to zero on Alcator C-Mod plasmas has been verified by independently calibrated spectrometers[24].

The wavelength calibration is accomplished by fitting an ellipse to two emission lines on each detector. To fit an ellipse to the curve of an emission line it is first necessary to generate a set of points that represents the location of the emission line centroids in the plane of the detector. This is accomplished by performing a multi line least squares fit to each row of the image. Figure 4-1 shows a raw image from the central module of the He-like detector array, taken during a locked mode discharge. The dashed lines represent the ellipse of best fit to the w and z lines.

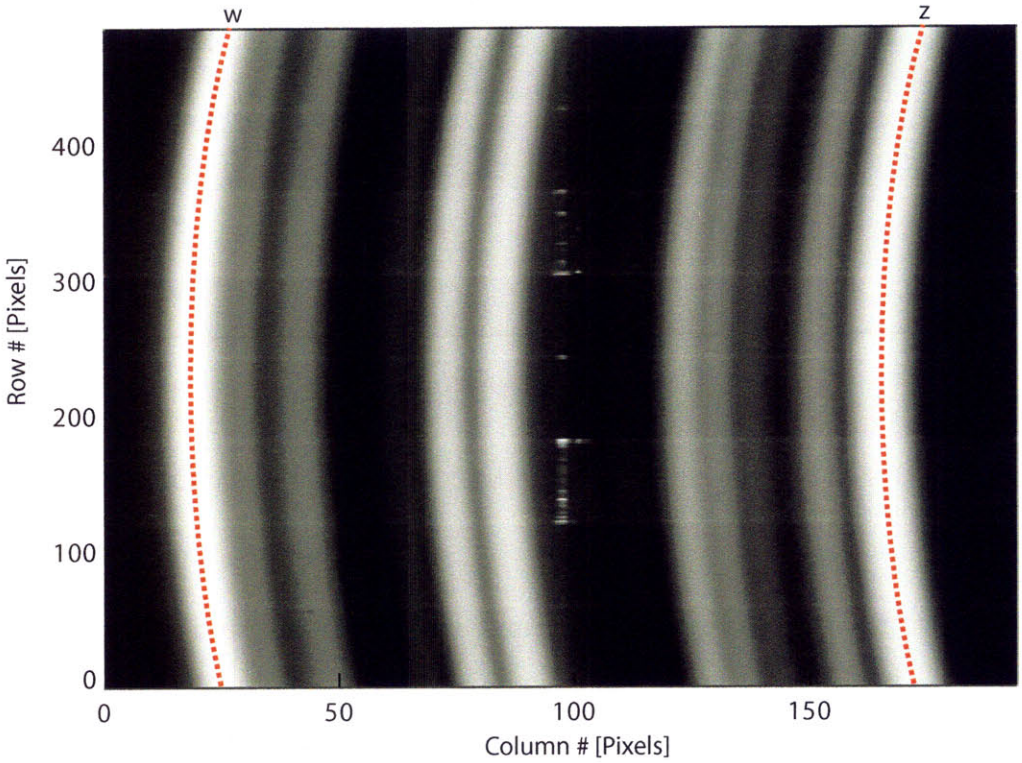

Figure 4-1: Raw image of the He-like argon spectra showing the elliptical curve of lines of constant λ

Figure 4-2 shows the residual of one of these elliptical fits. From this figure we see that the standard deviation of the residual is on the order of $1/100^{th}$ of a pixel. It is also clear that the residual is dominated by coherent structure, rather than photon

statistics. The cause of this structure has yet to be determined but may be due to variation in pixel sensitivity, artifacts introduced by the multi-line fitting routine or non-zero rotation profiles during locked mode discharges. A shift of $1/100^{th}$ of a pixel corresponds to a central plasma rotation velocity of approximately 500 m/s or equivalently ~ 10 μÅ.

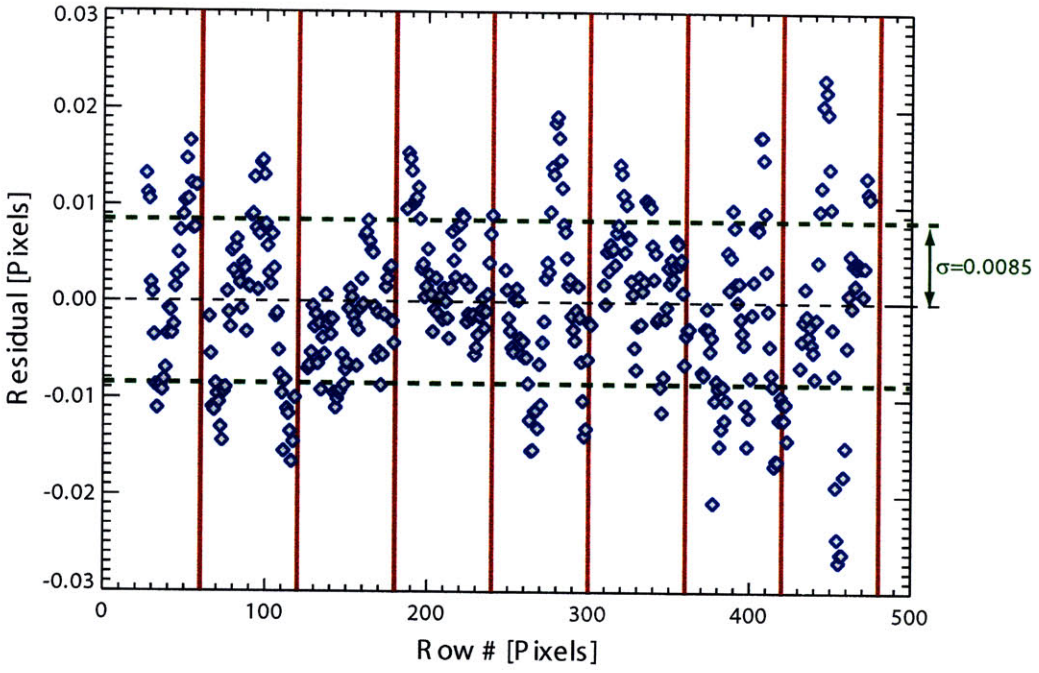

Figure 4-2: Residual of the elliptical fit to the 'z' line from the central module of the He-like detector array

The fact that the centroid of a line can be determined to such a small fraction of a pixel is interestingly (and counter-intuitively) due to finite line widths. If the width of an emission line is much smaller than a pixel, then all of the intensity from that line will be deposited onto a single pixel. In this case the centroid of the line can only be determined to within $\pm$ half a pixel. If, however, the intensity of a line is distributed over many pixels, then the uncertainty in the centroid will be dominated not by the pixel width but by statistical considerations. Given enough photons, the error in the centroid of a line associated with counting statistics can be driven well below the $\pm$ half a pixel level, as is shown here.

Once each pixel has been assigned a wavelength, the intensity data is mapped from the $[x, y]$ pixel space to the $[\lambda, Z]$ space, where λ is the assigned wavelength and Z refers to the height of the pixel in the spectrometer reference frame. Figure 4-3 shows the data from figure 4-1 remapped to $[\lambda, Z]$ space. Note that in the $[\lambda, Z]$ space the curvature of the line has been removed, while the boundaries of the image are now ellipses.

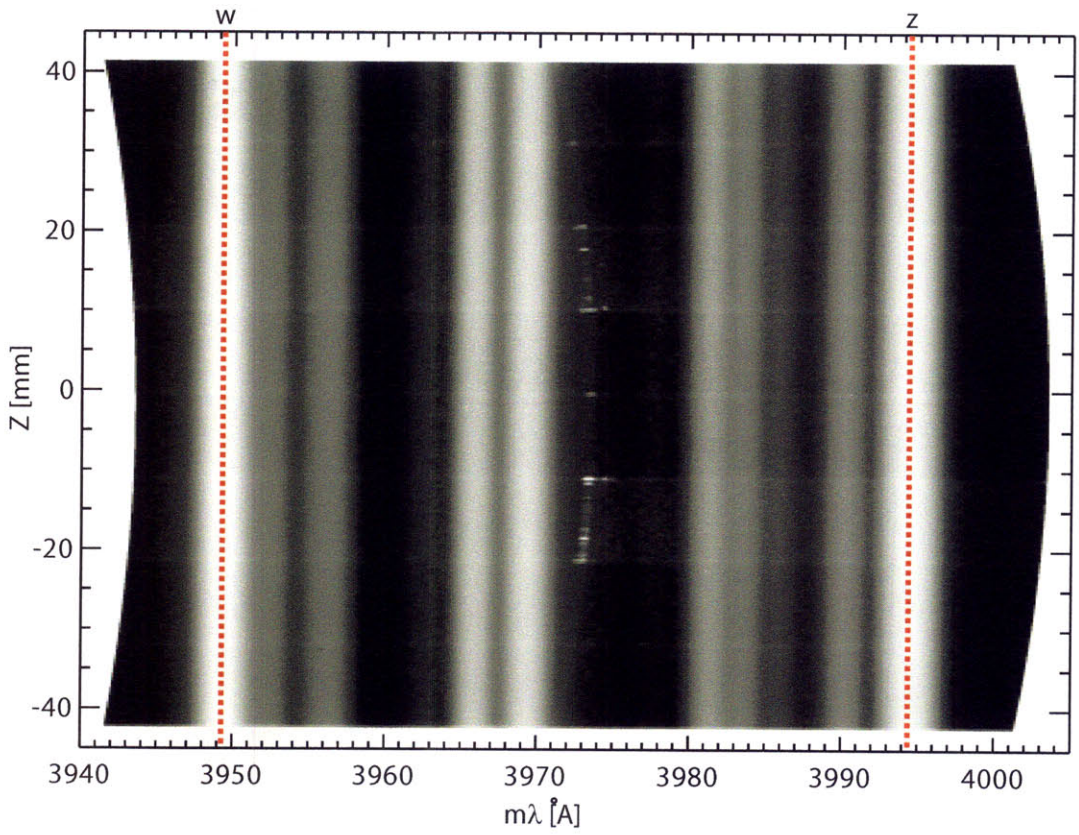

Figure 4-3: Curvature correction: Remapping of raw data from $[x, y]$ pixel space to $[\lambda, Z]$ space.

4.3.2 Multi-line Fitting

Before spectral tomographic techniques can be applied one must first isolate the signal of an emission line from the signal of any neighboring lines. This can be accomplished by performing multi-line least squares fits to the spectral data.

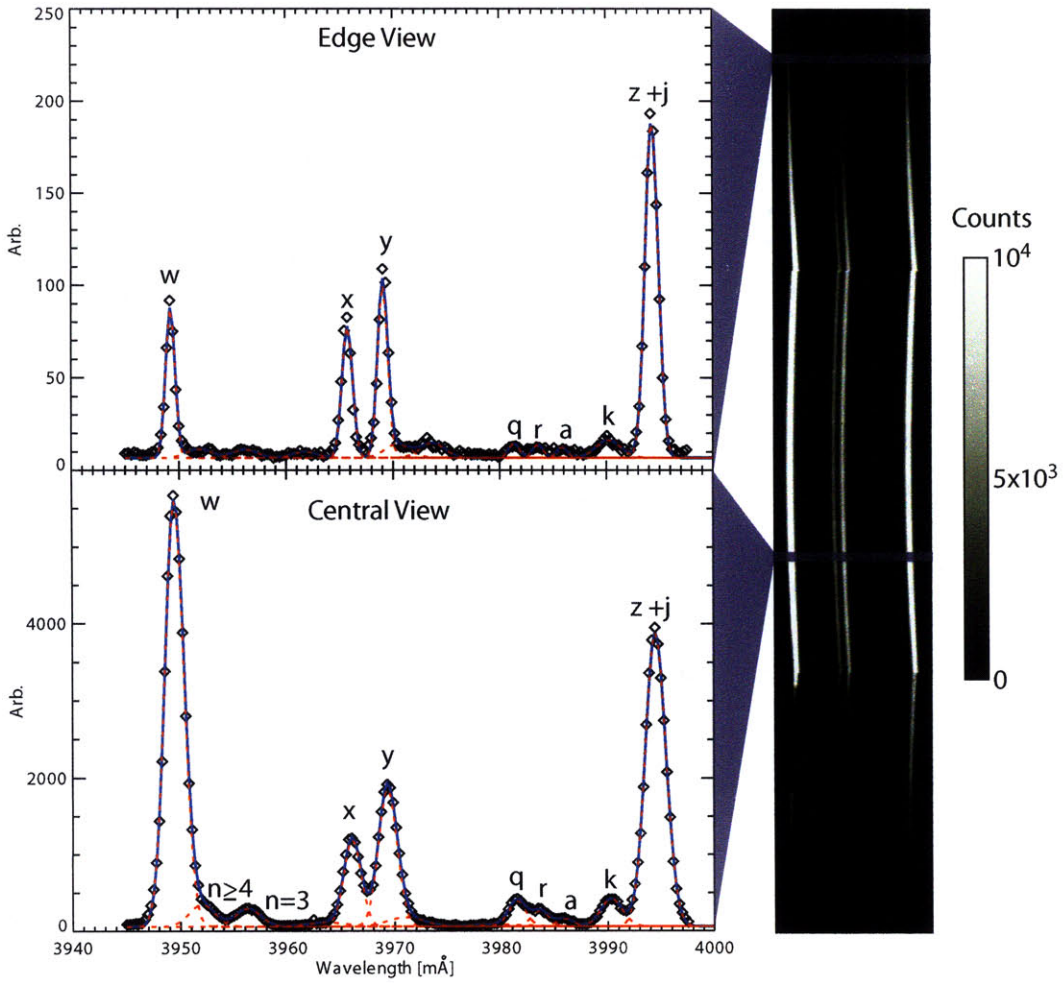

Figure 4-4: Examples of multi-line fits to He-like argon spectra

Figure 4-4 shows chord integrated He-like argon spectra (and satellites) from two sight lines through the plasma (left) and raw images from the 3 detector modules viewing the He-like spectra (right). The total multi-line fits are shown in solid blue while the intensities associated with individual lines are shown in dashed red. The greater widths of the lines in the centrally viewing spectrum compared to those in the

edge spectrum reflect the difference in ion temperature between these two locations in the plasma. More details on both the H- and He-like argon spectra can be found in appendix A.

The He-like detector array has a total of 1461 rows of pixels (487 per module) but these rows do not all provide independent views through the plasma. This is the result of the finite spatial resolution of the spectrometer described in chapter 2. An upper estimate of the number of independent spatial chords can be calculated by dividing the height of the plasma by the spatial resolution of the spectrometer. For the He-like Argon arm of Hirex-Sr the spatial resolution is ~7 mm (see equation 2.4 with $f_s = 2.43$ m, $L_{cp} = 3.06$ m and $d = 28$mm). Since the height of the plasma is ~70 cm, this gives approximately ~100 independent lines of sight (considerably less than the number of pixel rows). In this situation, binning the data in the spatial direction will improve the quality of the multi-line fits[1] without significant reductions in spatial resolution. In practice, it has been found that less than 100 spatial channels are required to capture the spatially varying features of the central portions of Alcator C-Mod plasmas. It has been found that having two spatial channels per sub-module, for a total of 48 spatial channels, generally provides a good balance between spatial resolution and the amount of signal per spectra.

4.3.3 Spectral Tomography

Spectral tomographic techniques can be used to infer local plasma quantities from the measured chord integrated spectra. For the densities and temperatures typical in magnetic confinement fusion plasmas, the Doppler effect dominates the broadening of soft x-ray emission lines. If the electron and ion distribution functions are Maxwellian, then the spectral brightness measured at the spectrometer can be expressed as:

$$B_j^{\lambda} = \int dl \frac{\epsilon_o(l)}{\sqrt{2\pi}w(l)} exp\left[\frac{\lambda - \lambda_o - \frac{\lambda_o}{c}(\hat{l}\cdot\vec{v}(l))^2}{2w(l)^2}\right] \tag{4.10}$$

[1]Multi-line fitting is non-linear in the sense that the sum of spectral fits is not equal to the fit of spectral sums. In general, one obtains more accurate results by first summing spectra and then fitting them. This constitutes a trade-off between spatial resolution and signal per spectra.

where B_j^λ is the spectral brightness of the j^{th} chord, l is the distance along the line of sight, $\hat{l}$ is the unit vector along the line of sight, ϵ_o is the emissivity, w is the full width half maximum (FWHM), λ_o is the unshifted wavelength, c is the speed of light, and $\vec{v}$ is the impurity velocity. As described in more depth in references [10] and [11], it is possible to generate a set of linear equations relating the spectral moments of chord integrated spectra to the kinetic profiles of the emitting species. The n^{th} spectral moment is defined as

$$M_{n,j} \equiv \int d\lambda (\lambda - \lambda_o)^n B_j^\lambda \tag{4.11}$$

Using this definition, the first three moment equations (i.e. n=0,1,2) are given by

$$M_{0,j} = \int dl \cdot \epsilon_o(l) \tag{4.12}$$

$$M_{1,j} = \frac{\lambda_o}{c} \int dl \left[\hat{l} \cdot \vec{v}(l)\right] \epsilon_o(l) \tag{4.13}$$

$$M_{2,j} = \int dl \left[\frac{\lambda_o^2}{c^2}\left(\hat{l} \cdot \vec{v}(l)\right)^2 + w(l)^2\right] \epsilon_o(l) \tag{4.14}$$

The $n = 0$ equation, or the zeroth equation, relates the line integral of emissivity to the measured brightness. The $n = 1$ equation relates the centroid of the measured line shape, $M_{1,j}$, to the line integral of the emissivity weighted by the dot product of the impurity velocity with the line of sight. The second moment of the spectral shape (n=2) is also a weighted line integral of the emissivity. The weighting in this case depends both on line shift and line broadening, $w(l)$, given by

$$w(l)^2 = \frac{\lambda_o^2 k T_i(l)}{m_i c^2} \tag{4.15}$$

where T_i and m_i are the temperature and mass, respectively, of the emitting species. Equations 4.12 through 4.14 constitute a coupled set of linear equations relating the first three spectral moments to the emissivity, velocity and temperature of the emitting species. A completely general 3D tomographic scheme would require a very

large number of lines of sight from multiple directions. The fact that tokamak plasmas are toroidally symmetric and that ϵ_o, $\vec{v}$ and T_i can be expressed in terms of flux functions reduces the complexity of the problem tremendously. In particular, these considerations make it possible to perform spectral tomographic measurements with a single fan of views.

A general approach has been developed to solve the system of moment equations described above for the case of a toroidally symmetric plasma [2]. The starting point for this approach is to project all lines of sight onto a poloidal plane thereby reducing the problem from three spatial dimensions to two. The integral equations are then recast as matrix equations by dividing the poloidal plane into rectangular volume elements. For each line of sight, a spatial weighting is then calculated for all the volume elements. Using magnetic flux surface reconstructions it is then possible to remap the spatial weightings from [R,Z] coordinates[3] in the poloidal plane to normalized minor radius, $\rho \equiv r/a$. This step effectively reduces the problem from two spatial dimensions to one. The spatial weightings only need to be calculated once since the spectrometer is not moving with respect to the reactor. The mapping from [R,Z] to ρ, however, needs to be recalculated at every time step due to the temporally evolving nature of magnetic flux surfaces throughout a discharge. The majority of computation time is spent on this flux surface remapping although the weightings for all 48 spatial channels, on a 100x100 grid, for 100 time points can be completed in under a minute on a personal workstation. Since an Alcator C-Mod shot cycle is typically $\sim$ 20 minutes this relatively short computation time allows for between shot analysis of the data.

For an arbitrary three dimensional velocity field the 1^{st} moment equation would be impossible to solve with a single fan of views. However, for a plasma satisfying radial force balance, with no radial velocity and a divergence-free flow, the velocity field is constrained to the following form [25]

[2]The spectral tomographic inversion algorithm described here was developed and implemented by M. L. Reinke as part of the GENIE (GENeral Impurity Emissivity) Code.

[3]Here R is the major radius, Z is the vertical distance with respect to the horizontal mid-plane, a is minor radius and r is the distance to the magnetic axis when mapped to the outboard mid-plane.

$$\vec{v} = u(\psi)\vec{B} + w(\psi)R\hat{\phi} \tag{4.16}$$

where $\vec{B}$ is the magnetic field vector, R is the major radius, $\hat{\phi}$ is the toroidal unit vector, ψ is poloidal magnetic flux, and u and w are arbitrary functions of ψ. The Hirex-Sr spectrometer has mixed toroidal and poloidal views which allows for the simultaneous measurement of both toroidal and poloidal rotation. This can be understood by first considering the line of sight directly viewing the magnetic axis. The line shifts for this spatial channel will always be dominated by toroidal flows (since the line of sight is effectively perpendicular to the poloidal direction). Spatial channels viewing above and below the magnetic axis, however, will observe line shifts in opposite directions for poloidal flows but in the same direction for toroidal flows. It is this difference that makes it possible to distinguish between the two types of flows.

4.4 Example Profiles

Applying the techniques described in the previous section it is possible to infer profiles of emissivity, charge-state densities, electron temperature, rotation velocities, ion temperature and radial electric field. Examples of such inversion are presented in the subsections that follow.

4.4.1 Emissivity Profiles

Local emissivity profiles are generated based on the inversion of the 0^{th} moment (i.e. brightness) of an emission line. Figure 4-5 shows a contour plot of emissivity inversions of the He-like argon 'z' line for an entire discharge. Early in the discharge we see that the emissivity profile of this line is peaked on axis and is core localized (i.e. the bulk of emission is at a normalized minor radius of $\rho < 0.5$). The application of ICRF heating (t = 0.7 s) raises the plasma temperature leading to a substantial broadening of the emissivity profile. Additionally, the peak of the emissivity profile is seen to shift off-axis. This hollowing out of the emissivity profile results from the core

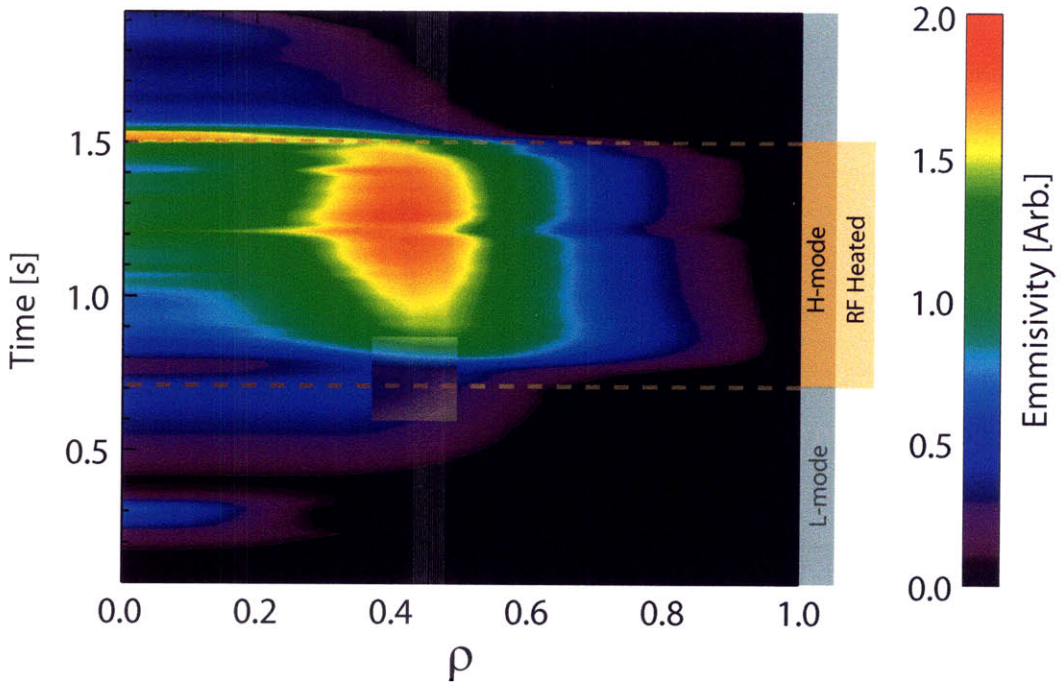

Figure 4-5: Emissivity contour plot of the w line from the He-like argon spectra.

temperature being so hot that the He-like charge state is "burning through". Figure 4-6 shows the same data as figure 4-5 in the form of a surface plot. This surface plot highlights the extent of the hollowing out of the emissivity profile during the high temperature portion of the discharge.

The tomographic inversion method described in the previous section assumes that emissivity is constant on magnetic flux surfaces. If this assumption is violated the resulting emissivity inversions represent flux surfaced averaged emissivities. It is possible to partially test the assumption that emissivity is a flux function by comparing inverted emissivity profiles of the top and bottom of the plasma. This test is only partial because it is only sensitive to up/down, as opposed to in/out, asymmetries. Figure 4-7 compares inverted emissivity profiles with data from just the top (red) and just the bottom (blue) of the plasma. An inversion based on all the data (i.e. the top and bottom) is also plotted (dashed black). The fact that all the curves are in close agreement suggests that there is no significant up/down emissivity asymmetry in this discharge.

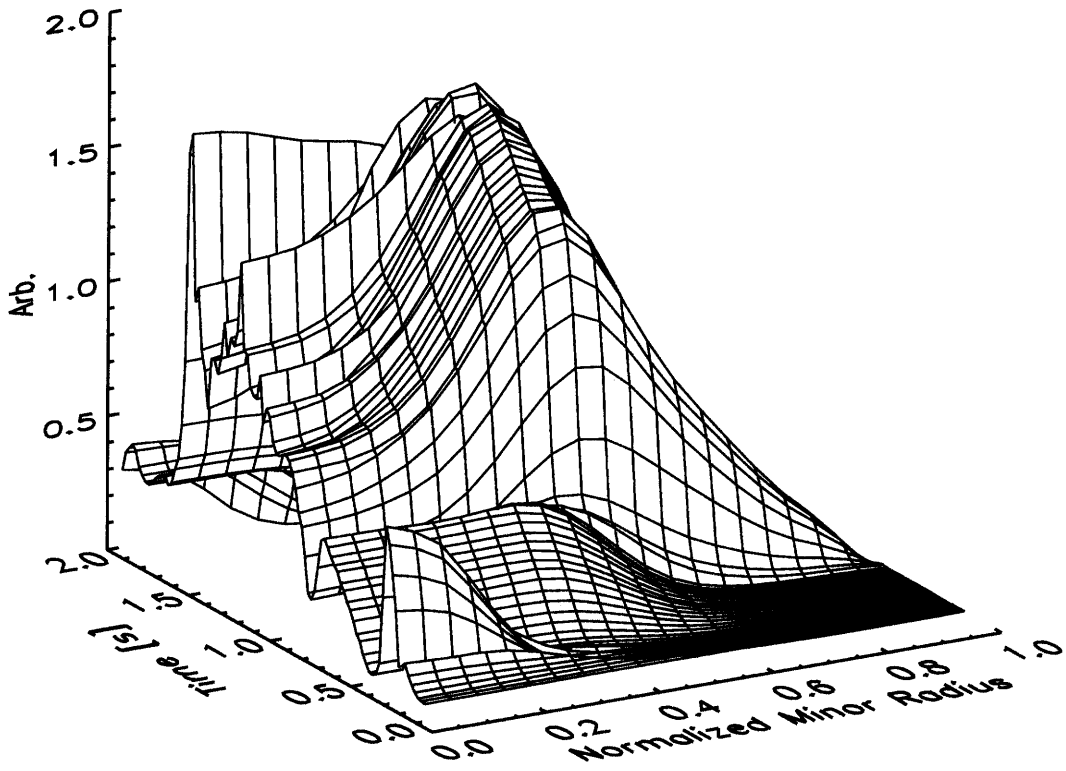

Figure 4-6: Emissivity surface plot of the w line from the He-like argon spectra.

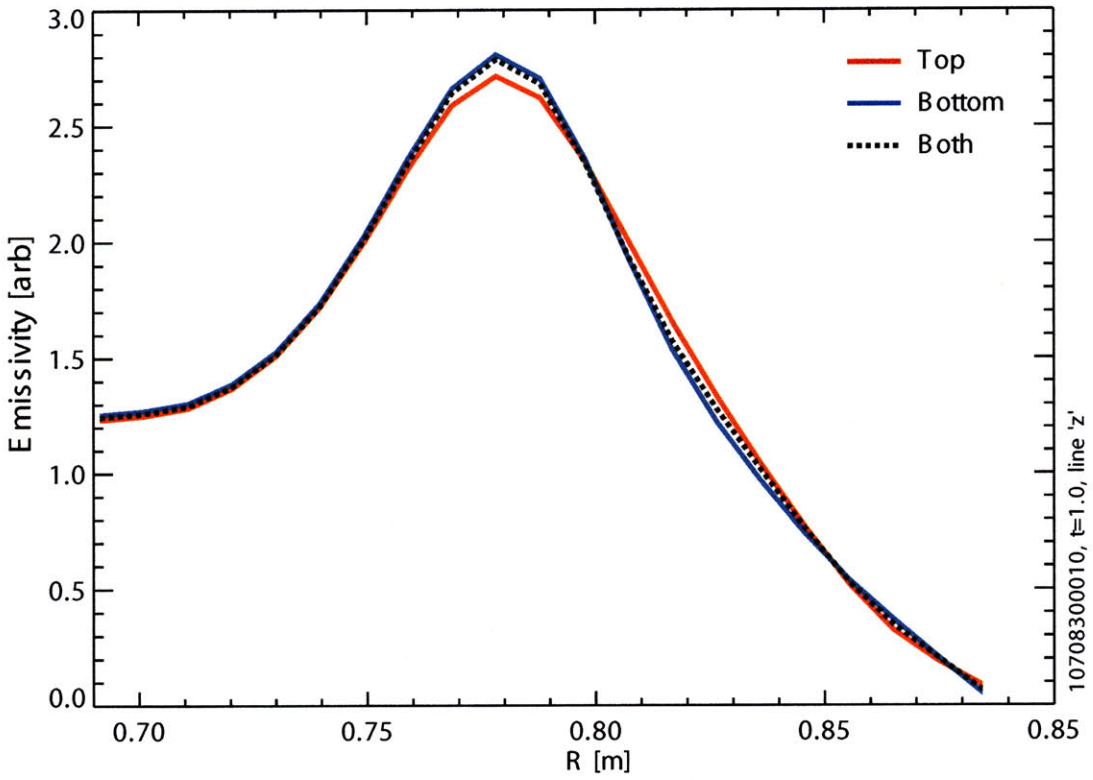

Figure 4-7: Comparison of inverted 'z' line emissivity profiles of the top (solid red) and the bottom (solid blue) of the plasma. The dashed black line is the result of an emissivity inversion of all the data.

4.4.2 Charge State Density Profiles

Given profiles of emissivity, electron density and temperature, one can use atomic physics modeling to calculate the density of the charge state that gives rise to measured emission lines. For the density and temperature ranges present in Alcator C-Mod plasmas collisional radiative models are a reasonable approximation. Example emissivity and charge state density profiles calculated using this method are shown in Figure 4-8 (The atomic physics rates used were generated by the Flexible Atomic Code[26]). In this figure we see that both the Li- and He-like argon density profiles are hollow (i.e. peaked off-axis). This is another example of a charge state being "burned through", as described in the previous section. The evolution of charge state density profiles such as these can be used to determine impurity transport coefficients.

4.4.3 Electron Temperature Profiles

As discussed in the previous chapter, the emissivity ratio of judiciously chosen emission lines can be used to infer electron temperatures. In practice, a "judicious" choice has the following characteristics:

1. The relationship between electron temperature and the emissivity ratio of the lines in question should be single valued.

2. The emission from all of the lines in question should be dominated by the same charge state.

3. To avoid introducing cross calibration errors all lines in the chosen ratio (both numerator and denominator) should be measured on the same detector.

4. There should be as little overlap as possible between the spectral ranges of the line(s) in the numerator and denominator.

For the He-like argon spectra the ratio of the w & $n \geq 4$ satellite lines to that of the $n = 3$ satellite lines provides the optimal balance between the often conflicting criteria summarized above. The satellite lines are populated predominantly by dielectronic

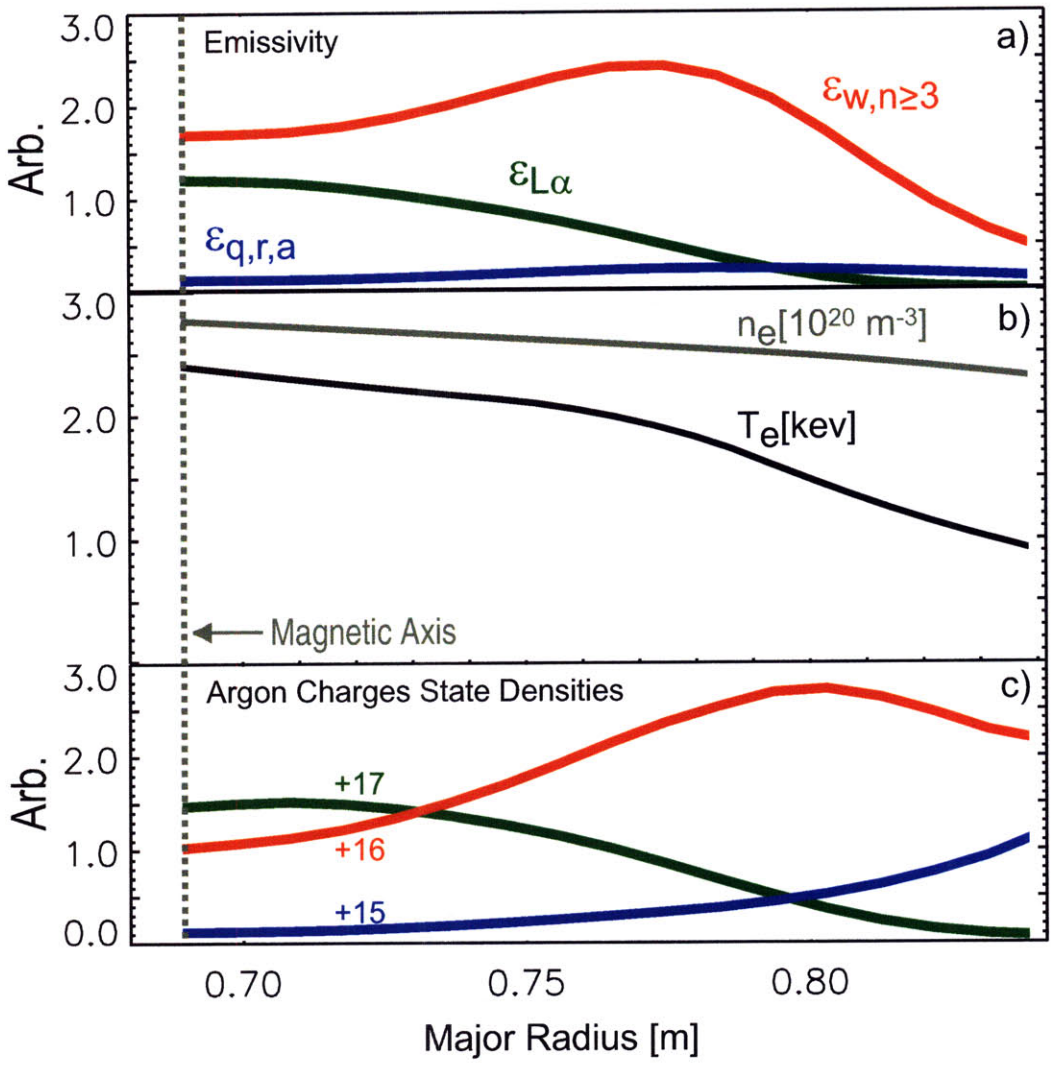

Figure 4-8: Emissivity a), electron density and temperature b), and argon charge state density c) vs major radius. By combing the emissivity profiles from multiple lines with electron density and temperature measurements, it is possible to estimate charge state densities profiles (+17 from the Lyman-α doublet, +16 from w, & $n \geq 3$ satellites and +15 from q, r & a). Figure reproduced from reference [27].

recombination from He-like argon whereas the w line is populated predominantly by electron impact excitation of the same charge state. Figure 4-9 shows the regions of the He-like spectra associated with this particular line ratio measurement. The relationship between this ratio and electron temperature is shown in figure 4-10. Note that the analysis presented here does not included radiative recombination rates. Therefore using this approach when radiative recombination is important can lead to inaccuracies in the inferred electron temperature.

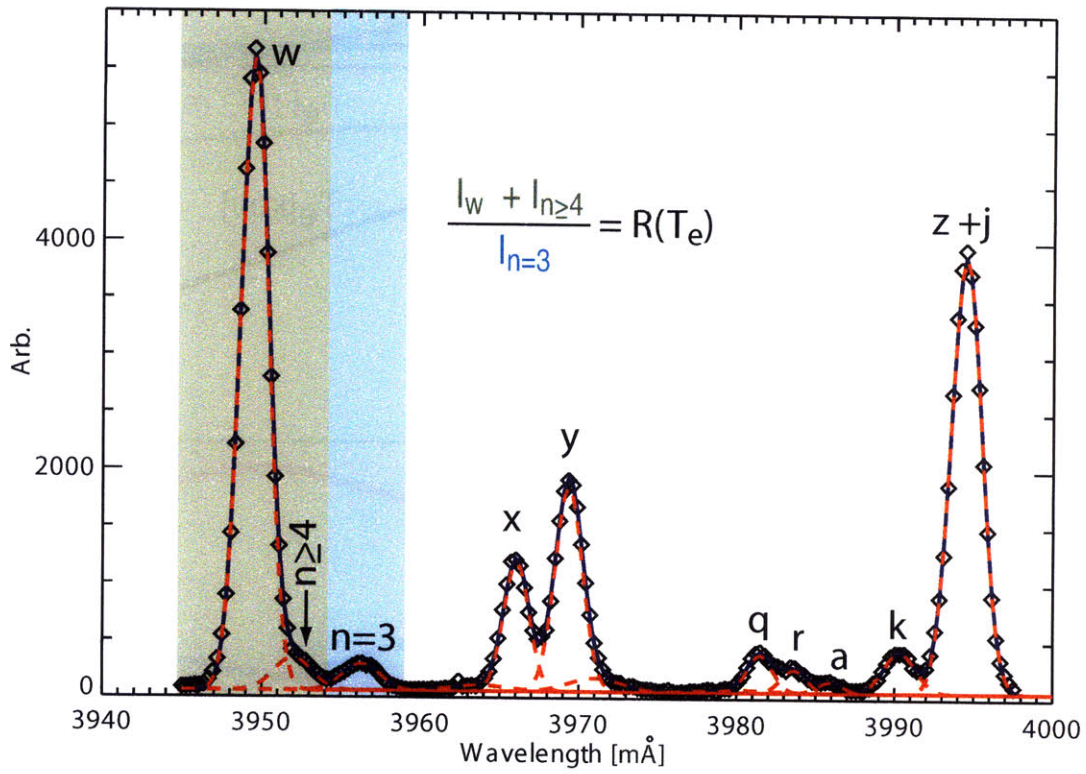

Figure 4-9: Line ratios from He-like argon spectra for electron temperature measurements.

Using the function shown in figure 4-10, one can readily calculate the electron temperature based on measured intensity ratios. To get an accurate local measurement of the electron temperature it is necessary to take the ratio of local emissivities as opposed to the line integrated brightnesses. Figure 4-11 compares the inferred electron temperature profiles based on line integrated brightnesses (open circles) and local emissivity profiles (solid blue). The large difference between the line integrated

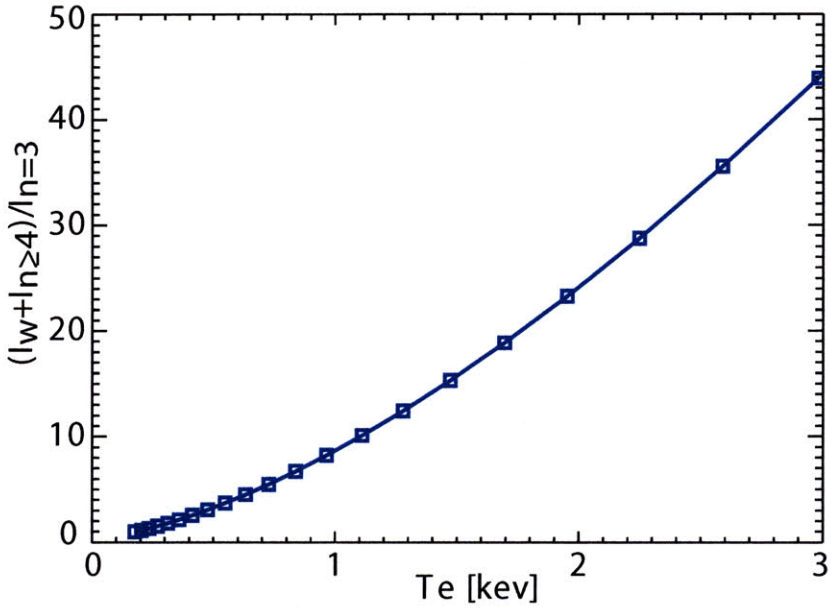

Figure 4-10: Ratio of the intensity of the w & $n \geq 4$ satellite lines to the $n = 3$ satellite lines as a function of electron temperature[28].

brightness data and independent electron temperature measurements demonstrates the value of performing the tomographic inversion. The difference between the line-integrated and tomographically inverted data may explain the long standing discrepancies between some line ratio measurements from Electron Beam Ion Traps (EBIT) and tokamak plasmas [29]. It should be noted that accurate T_e inversions from the particular line ratios used here become impractical at electron temperatures above ~3 keV due to the blending of the n=3 lines with the n≥4 lines.

4.4.4 Toroidal Rotation Profiles

Figure 4-12 shows an example of inverted toroidal rotation profiles in a discharge with strong radio frequency (RF) heating. Shortly after the application of the RF heating, a reversal of toroidal rotation is observed, from the counter-current to co-current direction. Later in the discharge, the plasma transitions into a regime of higher confinement (H-mode) and an increase in core rotation is observed. Figure 4-13 shows the toroidal rotation frequency evolution for a different RF heated discharge

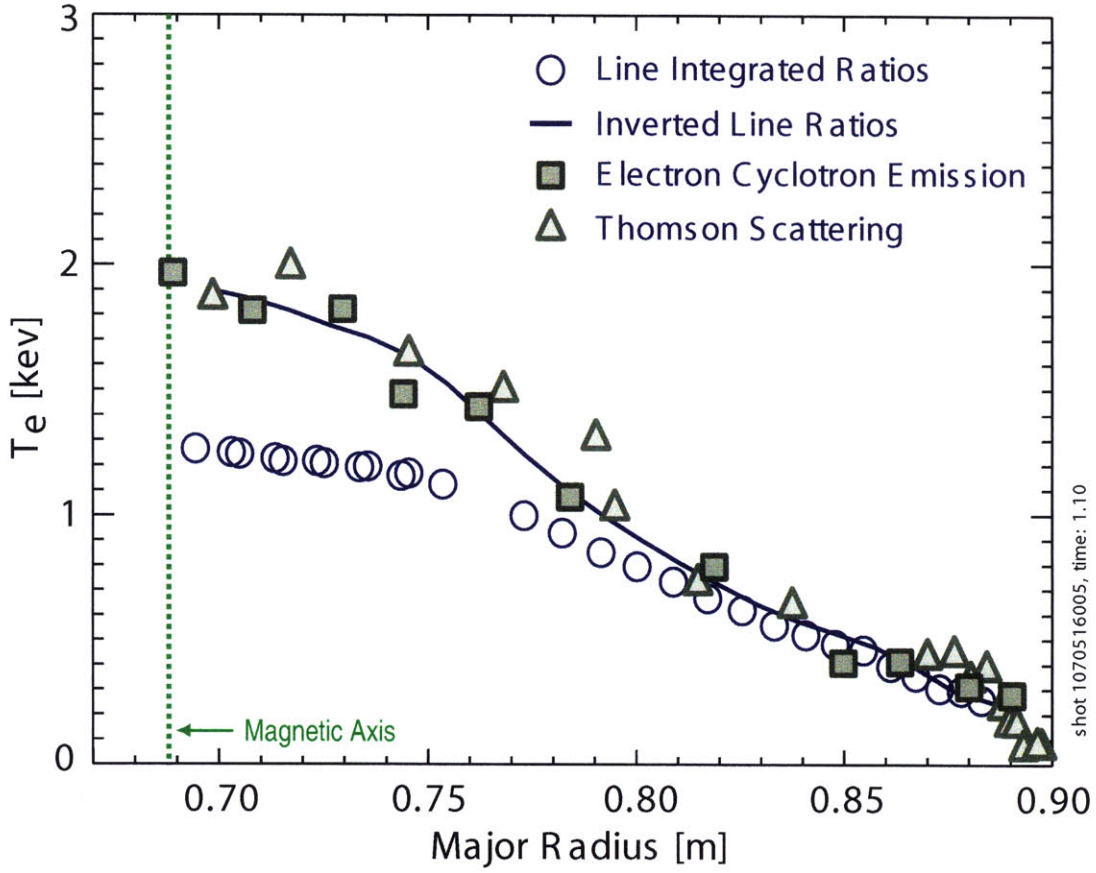

Figure 4-11: Electron temperature profiles based on line integrated brightness ratios (open circles) and inferred local emissivities (solid blue line). Independent measures of the electron temperature profile from electron cyclotron emission (squares) and Thomson scattering (triangles) are also shown. Figure reproduced from reference [27]

in the form of a surface plot. Again we see the characteristic rotation inversion from the counter- to co-current direction after the application of strong heating. Chapters 6, 7 and 8 provide much more detail on a variety of toroidal rotation phenomena observed in Alcator C-Mod and other tokamaks.

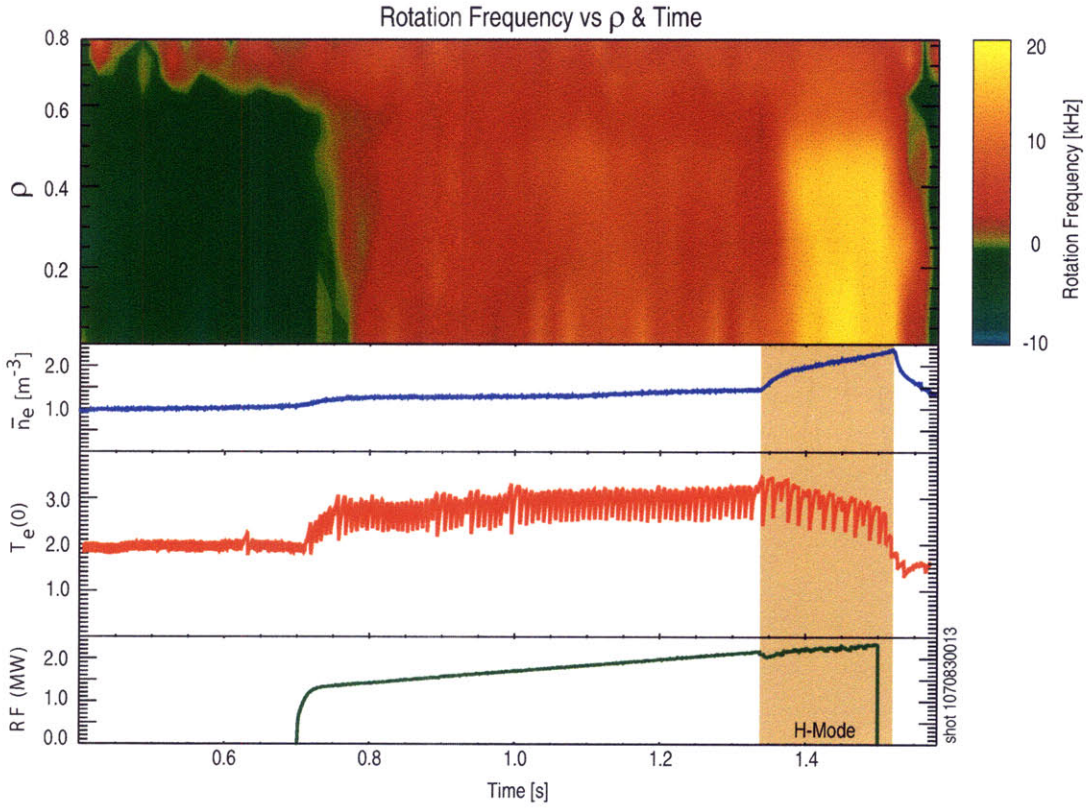

Figure 4-12: Contour plot showing the rotation profile evolving during an RF heated plasma. Time histories of the line averaged density, central electron temperature and RF heating power are also shown. Figure reproduced from reference [27]

4.4.5 Ion Temperature Profiles

In Alcator C-Mod plasmas the deuterium-argon energy equilibration time ($\sim$ 10s of μs) is much shorter than the energy confinement time ($\sim$10s of ms). This implies that the argon and deuterium temperatures are well coupled and therefore, the measured argon temperature is also a measure of the main ion temperature. A more comprehensive treatment of impurity-ion thermal coupling is given in appendix C. Figure

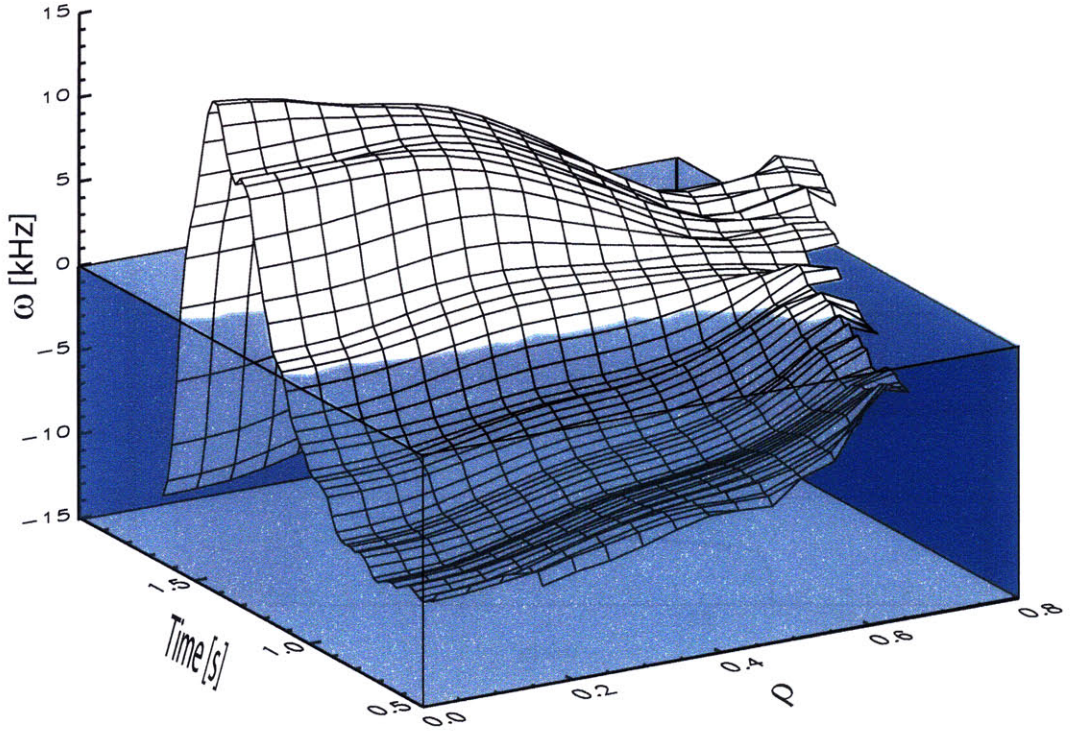

Figure 4-13: Surface plot of the toroidal rotation frequency evolution in an RF heated discharge. The "water level" in this plot indicates where the rotation frequency is zero (i.e. portions of the surface plot above the water level indicate co-current rotation).

4-14 shows an example of inferred ion temperature profiles based on the inversion of argon line emission. In this discharge the application of ICRF power at 0.7 s leads to rapid heating of the plasma, a transition to H-mode and the onset of large sawtooth oscillations. The ion temperature profile is seen to peak strongly at the beginning of the H-mode and then gradually decrease. At 1.5 s the RF power is switched off and shortly thereafter the plasma back transitions into L-mode at which point the plasma cools rapidly. Figure 4-15 shows the same ion temperature data as figure 4-14 in the form of a surface plot. This figure helps to highlight the difference in profile shape between the L-mode and H-mode portions of the discharge.

Figure 4-16 shows a comparison of temperature profiles for a plasma in which the electrons and ions are well coupled thermally. The solid red line is the result of consolidating the independently measured temperature profiles from 4 different emission lines (w and z from He-like argon and the Lyman-doublet from H-like argon).

Figure 4-17 a) shows T_i profile data from the He-like w line based on line averaged data (blue diamonds) and a tomographic inversion (red line). The normalized emissivity profile for the w line is shown in panel b). This figure is an example of the general principle that the error associated with line averaged data is substantially larger in regions of the plasma where the emissivity profile is hollow (i.e $\frac{\partial \epsilon}{\partial r} < 0$). Conversely, the good agreement in the outer portion of the plasma demonstrates that line averaged data can give accurate results in regions of the plasma where the emissivity profile is peaked ($\frac{\partial \epsilon}{\partial r} > 0$).

4.4.6 Radial Electric Field Profiles

Direct measurement of the radial electric field is possible using heavy ion beam probes[30], however, these measurements are very difficult and have only been performed on a limited number of tokamaks. An alternative approach to determining the radial electric field is to use the radial pressure balance equation,

$$E_r = \frac{\nabla P}{Z_i e n_i} + V_\phi B_\theta - V_\theta B_\phi \tag{4.17}$$

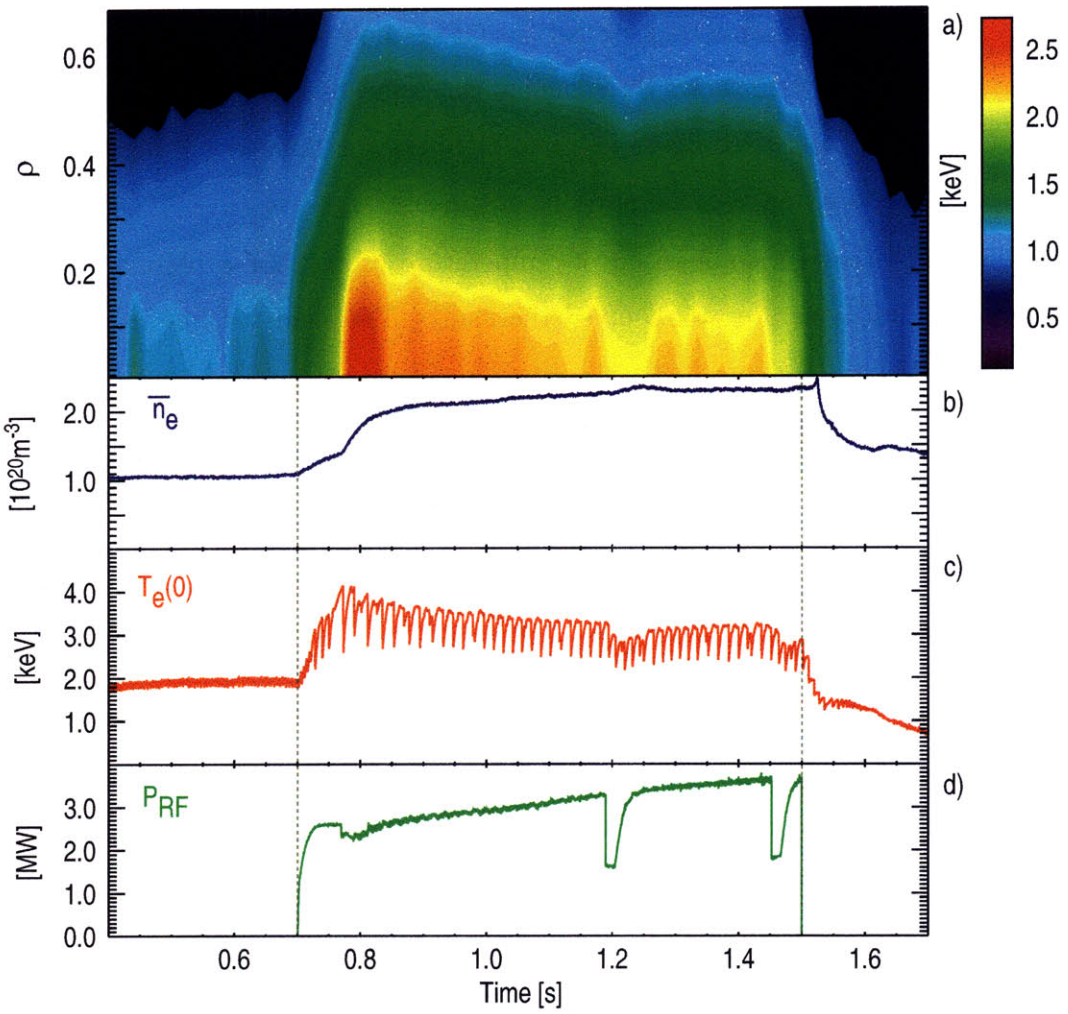

Figure 4-14: Contour plot showing the ion temperature as a function of normalized minor radius and time in an RF heated plasma. Time histories of the line averaged density b), central electron temperature c), and RF heating power d) are also shown.

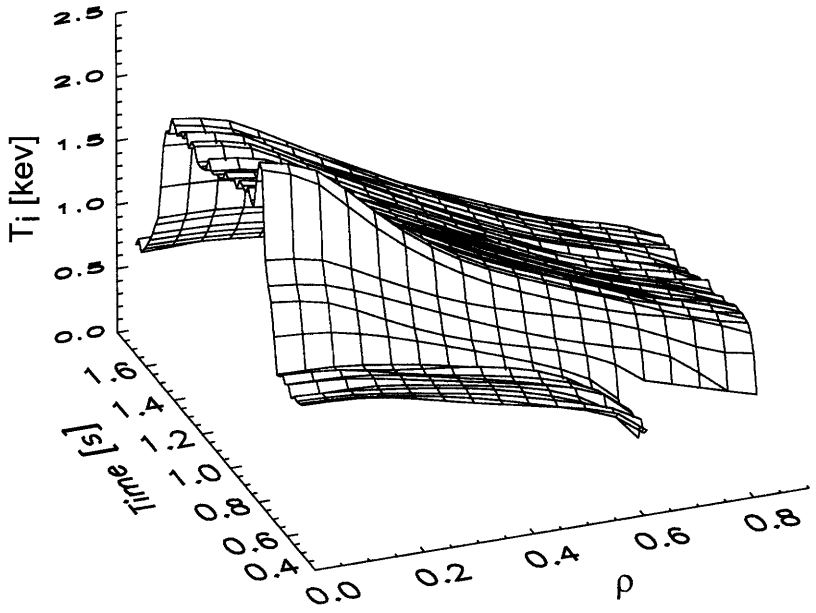

Figure 4-15: Surface plot of the ion temperature profile for the same discharge depicted in 4-14.

where E_r is the radial electric field, P_i is the pressure, n_i is the density, Z_i is the charge of the species in question, V_θ and V_ϕ are the poloidal and toroidal rotation, respectively, and B_θ and B_ϕ are the poloidal and toroidal magnetic field, respectively. Since radial pressure balance is satisfied for all species in the plasma, measurement of impurity flows and pressure, coupled with magnetic measurements, can be used to calculate the radial electric field. This technique has been used successfully with charge exchange recombination diagnostics on a number of tokamaks [31]. In general all three terms in equation (4.17) can contribute significantly to the radial electric field. In the particular case of He-like argon in the central region of Alcator C-Mod plasmas it has been found that the toroidal rotation term ($V_\phi B_\theta$) dominates the diamagnetic ($\frac{\nabla p}{Z_i e n i}$) and the poloidal rotation ($V_\theta B_\phi$) terms. The relative contribution of the diamagnetic term can be more clearly seen by rewritten it as,

$$\frac{\nabla p}{Z_i e n_i} = \frac{T_i}{Z_i e} L_{P_i}^{-1} \tag{4.18}$$

where $L_{P_i}^{-1}$ is the inverse pressure gradient scale length. The combination of a large Z_i

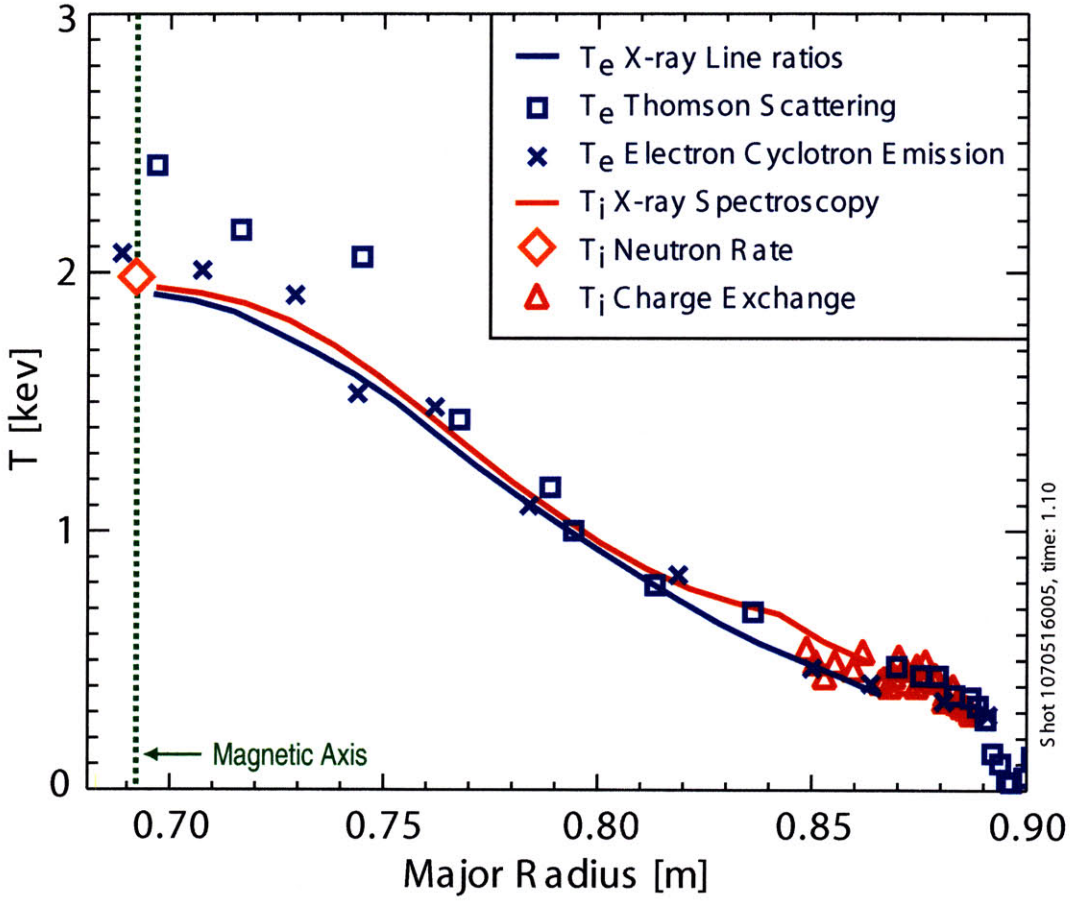

Figure 4-16: Impurity and electron temperature profiles in a high density discharge with good thermal equilibration between ions and electrons. Figure reproduced from reference [27].

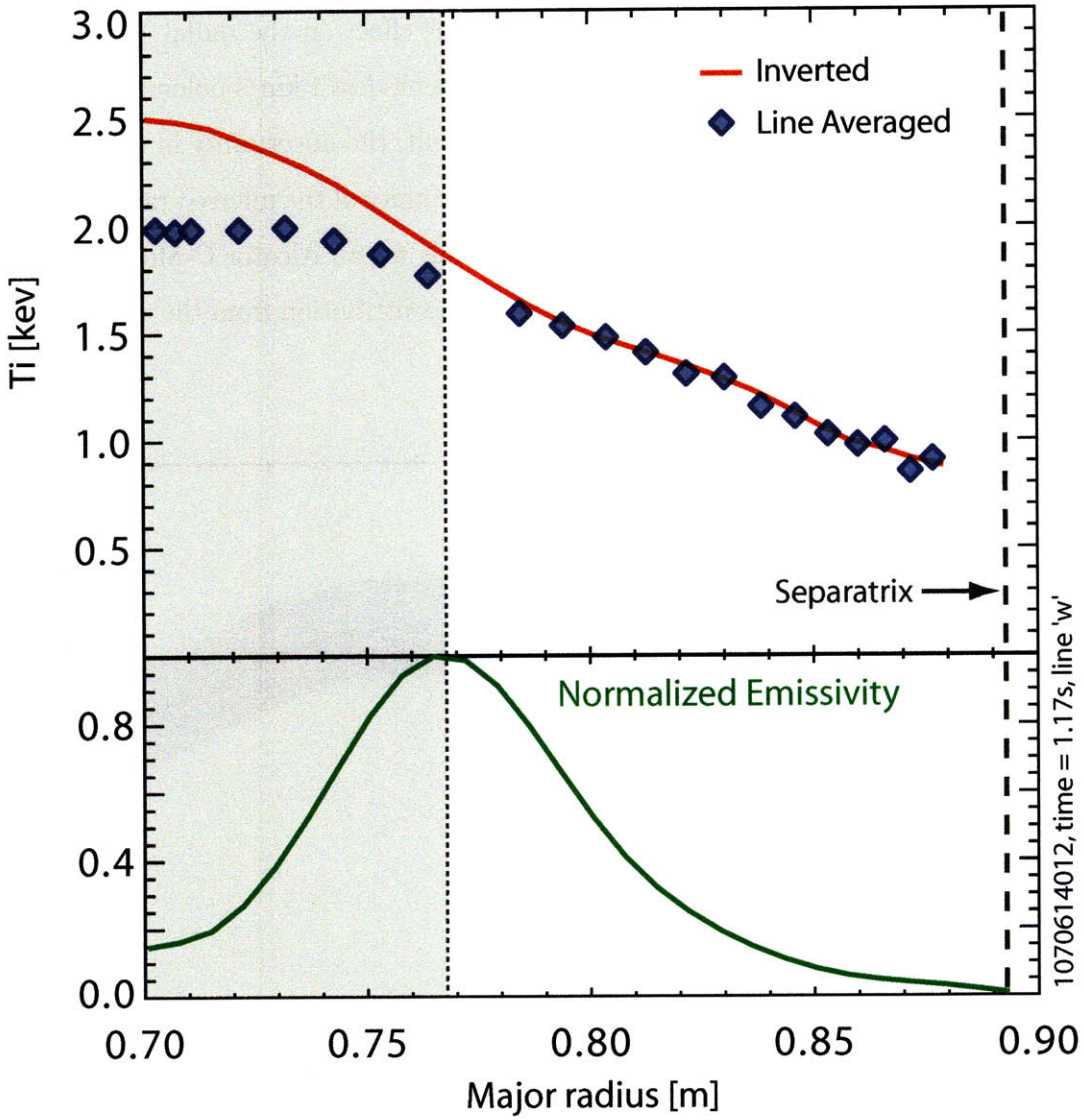

Figure 4-17: Comparison of T_i based on line averaged (blue diamonds) and inverted (red line) data. The normalized emissivity profile is shown in panel b).

for highly ionized argon and moderate gradient scale lengths means that the diamagnetic term tends to be relatively small. In almost all discharges the measured argon poloidal rotation velocity is within error bars of zero and therefore, as stated above, the toroidal rotation term tends to dominate radial pressure balance. Although the poloidal rotation is small, it can have a significant effect on the radial electric field because it is multiplied by the toroidal field. Even a modest 1 km/s poloidal flow gives rise to a contribution of ~ 5 kV/m to E_r. As a result, the uncertainty in the poloidal rotation measurement tends to dominate the uncertainty of the inferred radial electric field. Figure 4-18 shows a radial electric field profile for an Alcator C-Mod discharge based on the method outlined above. The modest contribution from the diamagnetic term is plotted on the same scale for comparison.

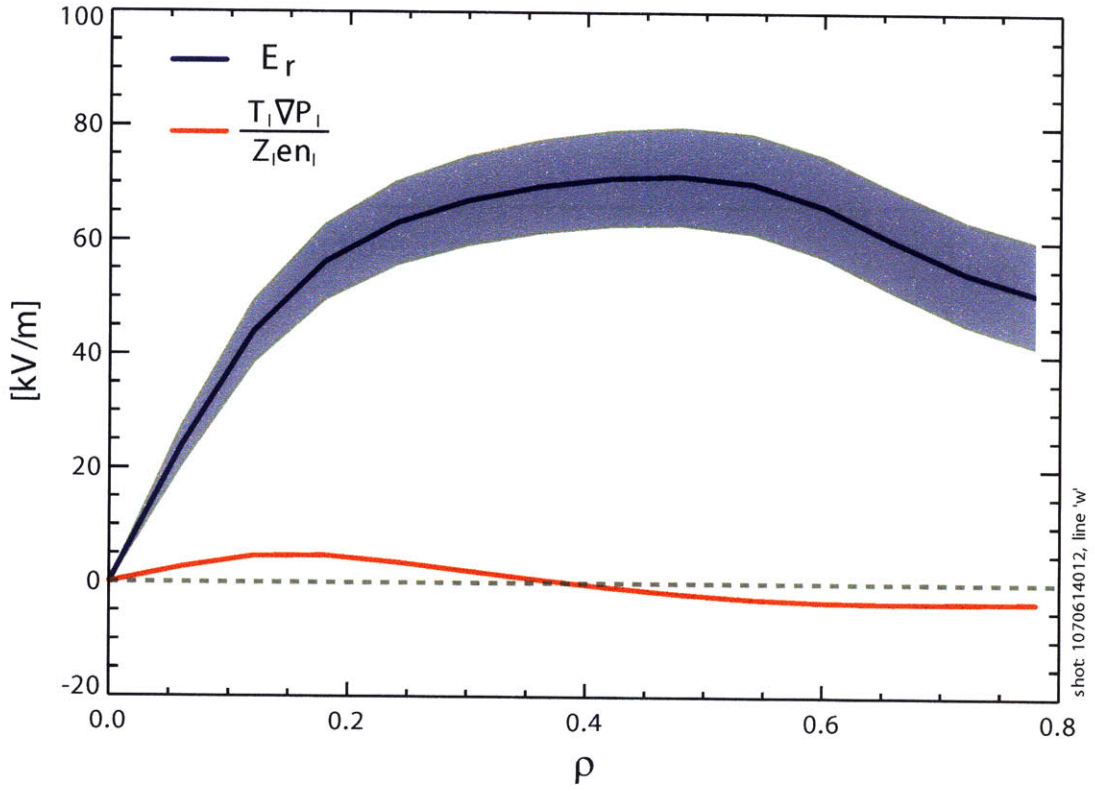

Figure 4-18: Plot of the radial electric field profile. The total radial electric field is shown in blue, while the contribution from the diamagnetic term is shown in red.

Figure 4-19 shows the radial electric field profile based on x-ray argon data in the

core region and boron charge exchange data in the pedestal. The error bars on the x-ray data are based on a characteristic uncertainty of 3 km/s of poloidal rotation. The fact that measurements from two different impurities agree so well is strong evidence that the various assumptions that went into this analysis are valid. Figure 4-20 shows the evolution of the E_r profile for an entire discharge. Shortly after the application of ICRF heating ($\sim$ 0.7 s), the plasma transitions from L-mode to H-mode. As this transition takes place the radial electric field is seen to change from negative (radially inward) during the L-mode phase to positive (radially outward) during the H-mode phase.

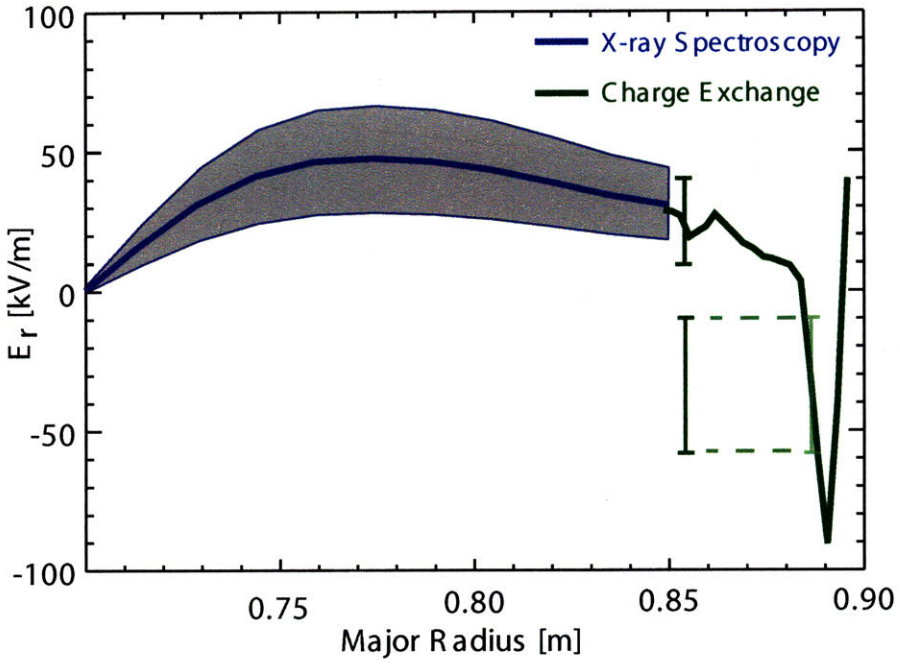

Figure 4-19: Comparison of radial electric field measurements from Hirex-Sr and charge exchange spectroscopy (CXRS).

4.5 Chapter Summary

This chapter has outlined the basic physical mechanisms that imbue spectra of line radiation with a wealth of information about the plasma from which it is emitted. Specifically, Doppler shifted x-ray line radiation provides detailed information on the

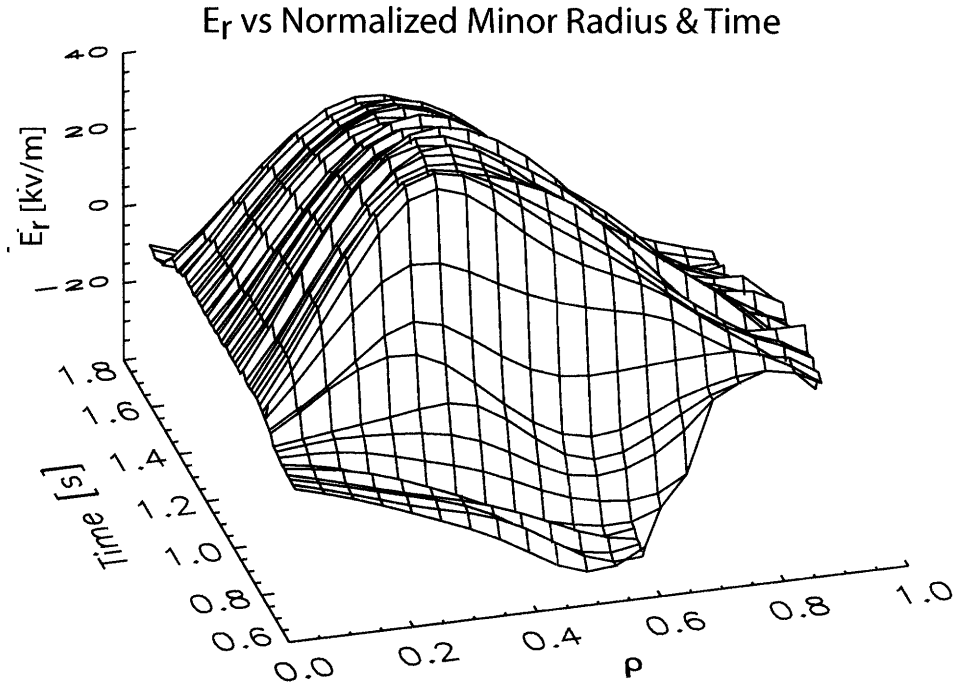

Figure 4-20: E_r Profile evolution Through An L-H transition

distribution function of the emitting impurity. Knowledge of the impurity distribution function can be used to determine charge state density profiles, impurity rotation velocities and ion temperatures. Electron temperature profiles can be determined by taking advantage of the temperature dependence of emission lines from the same charge state. These quantities when combined with magnetic field measurements and the radial pressure balance equation allow for the calculation of the radial electric field. Obtaining localized (as opposed to line averaged) measurements of these quantities requires spectral tomographic techniques be used. The profiles shown in this chapter represent the first ever demonstration of spectral tomographic inversions of x-ray line emission data.

Chapter 5

Rotation Theory

Many theories have been developed to explain the wide variety of rotation phenomenology that has been observed in tokamak plasmas. These theories can be broadly grouped into three categories: Classical, wave induced and turbulence based. Here classical refers to theories in which Coulomb collisions are responsible for all cross field transport. Wave induced rotation refers to those theories that are based on interactions between plasmas and externally applied waves, such as ion cyclotron range of frequency waves (ICRF). Turbulence based flow theories, as the name suggests, rely on plasma turbulence to drive and/or redistribute momentum in a plasma. A brief overview of the main theories in each of these categories is given in the sections that follow.

5.1 Neoclassical Rotation Theory

Neoclassical rotation theory has the distinction of being the most cited and most frequently contradicted of all rotation theories. There have been many publications in which non-neoclassical rotation and/or momentum transport has been reported[24][32]. The discrepancy between neoclassical theory (NCT) and experiment is not due to errors in the derivation of the theory, but rather our inability to produce plasmas in which the assumptions of NCT are valid. Specifically, NCT does not take into account turbulence effects which typically dominate cross field transport nor does it allow for

radial gradients on the same spatial scale as the gyroradius. If future devices are capable of producing plasmas in which turbulence is largely suppressed, then we may expect the rotation to be approximately neoclassical in regions of modest plasma gradients.

Expressions for the neoclassical poloidal and toroidal rotation can be derived using the moment approach of Hirshman and Sigmar [33]. The neoclassical poloidal rotation velocities for the main ions and a trace impurity are given by (equations 33 and 34 in reference [25]):

$$V_\theta^i = \frac{1}{2} v_{T_i} \rho_i \left[K_1 \frac{1}{L_{T_i}} \right] \frac{B B_\phi}{\langle B^2 \rangle} \tag{5.1}$$

$$V_\theta^I = \frac{1}{2} v_{T_i} \rho_i \left[\left(K_1 + \frac{3}{2} K_2 \right) \frac{1}{L_{T_i}} - \frac{1}{L_{p_i}} + \frac{Z_i}{Z_I} \frac{T_I}{T_i} \frac{1}{L_{p_i}} \right] \frac{B B_\phi}{\langle B^2 \rangle} \tag{5.2}$$

where L_x^{-1} is the gradient scale length of x (i.e. $d \ln x / dr$), v_{T_i} is the ion thermal velocity ($\equiv \sqrt{2T_i/m_i}$), ρ_i is the ion Larmor radius ($\equiv m_i v_{T_i} / Z_i e B$) and K_1 and K_2 are viscosity matrix coefficients given by the comically nested set of equations below.

$$K_1 = D^{-1} \mu_{01}^i \left(\sqrt{2} + \alpha - \alpha\beta \right) \tag{5.3}$$

$$K_2 = D^{-1} \left[\mu_{00}^i \mu_{11}^i - \left(\mu_{01}^i \right)^2 \right] \tag{5.4}$$

where

$$D = \mu_{00}^i \left(\mu_{11}^i + \sqrt{2} + \alpha - \alpha\beta \right) - \left(\mu_{01}^i \right)^2 \tag{5.5}$$

and

$$\alpha = \frac{n_I Z_I^2}{n_i Z_i^2} \tag{5.6}$$

$$\beta = \left(\frac{27}{4} \right)^2 \left(\frac{m_i}{m_I} \right)^2 \left(\frac{15}{2} + \sqrt{2\alpha} \frac{v_{T_i}}{v_{T_I}} \right)^{-1} \tag{5.7}$$

An approximate formula for μ_{00}^a and μ_{11}^a valid over a range of collisionality regimes is given by

$$\mu_{ii}^a = \frac{g\hat{\mu}_{ii}^B}{\left(1 + 2.92\nu_{*a}\hat{\mu}_{ii}^B/\hat{\mu}_{ii}^P\right)\left[1 + \hat{\mu}_{ii}^P/\left(6\omega_{ta}\tau_{aa}\hat{\mu}_{ii}^{PS}\right)\right]} \tag{5.8}$$

The off-diagonal μ's (i.e. μ_{01} and μ_{10}) are then given by

$$\mu_{01}^a = \frac{5}{2}\mu_{00} - K_{01} \tag{5.9}$$

where $\mu_{01} = \mu_{10}$ and

$$K_{01} = \frac{g\hat{K}_{01}^B}{\left(1 + 2.92\nu_{*a}\hat{K}_{01}^B/\hat{K}_{01}^P\right)\left[1 + \hat{K}_{01}^P/\left(6\omega_{ta}\tau_{aa}\hat{K}_{01}^{PS}\right)\right]} \tag{5.10}$$

Here ω_{ta} is the thermal transit frequency,

$$\omega_{ta} = v_{Ta}/R_o q \tag{5.11}$$

where R_o is the major radius and q is the safety factor. τ_{ab} is the Braginskii collision time and is given by

$$\frac{1}{\tau_{ab}} = \frac{16\sqrt{\pi}}{3}\left(\frac{Z_a Z_b e^2}{4\pi\epsilon_o}\right)^2 \frac{n_b \ln\Lambda}{m_a^2 v_{T_a}^3} \tag{5.12}$$

g is the ratio of the trapped particle fraction, f_t, to the circulating particle fraction, f_c, i.e. $g = \frac{f_t}{f_c} = \frac{1-f_c}{f_c}$. An approximation for f_c when $0 \leq \epsilon \leq 1$ is given by,

$$f_c \approx 1 - 1.46\sqrt{\epsilon} + 0.46\epsilon\sqrt{\epsilon} \tag{5.13}$$

The collisionality parameter, ν_{*a}, in equations 5.10 and 5.8 is given by

$$\nu_{*a} = \frac{g}{1.46}\frac{\omega_{ta}}{v_{ta}^2\tau_{aa}}\frac{\langle B^2\rangle}{\left\langle(\mathbf{b}\cdot\nabla\mathbf{B})^2\right\rangle} \tag{5.14}$$

where $\langle\ldots\rangle$ is the flux surface average of the quantity in the brackets, $\mathbf{B}$ is the vector magnetic field and $\mathbf{b}$ is the magnetic field unit vector. The expressions for the

quantities $\hat{\mu}_{ii}$ and $\hat{K_{01}}$ for various collisionality regimes are summarized in table 5.1.

Table 5.1: Summary of the asymptotic dimensionless viscosity coefficients, where $d \equiv 2.23 + Z_{eff} + 2.40 Z_{eff}^2$. Reproduced from table I in reference [25].

Collisionality	**Banana** $\hat{\mu}^B$ or $\hat{K^B}$	**Plateau** $\hat{\mu}^P$ or $\hat{K^P}$	**Pfrisch-Schluter** $\hat{\mu}^{PS}$ or $\hat{K^{PS}}$
$\hat{\mu}_{00}$	$0.52 + Z_{eff}$	3.54	$(3.02 + 4.25 Z_{eff})/d$
$\hat{K}_{01}$	$0.71 + Z_{eff}$	10.63	$(12.43 + 20.13 Z_{eff})/d$
$\hat{\mu}_{11}$	$1.39 + 13 Z_{eff}/4$	11.52	$(15.38 + 26.97 Z_{eff})/d$

Gyroviscous effects are ignored in NCT which leads to identical expressions for the electron and ion radial particle flux. This so-called "automatic ambipolarity" means that the radial electric field can not be calculated using NCT. As a result the toroidal rotation velocities of both the main ions and the impurities can only be written in terms of the unspecified E_r profile (via radial pressure balance) as shown below.

$$V_\phi^I = \frac{1}{B_\theta}\left[E_r + V_\theta^I B_\phi - \frac{\nabla p_I}{Z_I e n_I}\right] \tag{5.15}$$

$$V_\phi^i = \frac{1}{B_\theta}\left[E_r + V_\theta^i B_\phi - \frac{\nabla p_i}{e n_i}\right] \tag{5.16}$$

If nothing else, the collection of equations above gives some sense of the complexity of even the simplest of analytic transport theories.

5.2 Sub-Neoclassical Theory

One of the fundamental limitations of NCT is the assumption that all macroscopic scale lengths are of the same order[34]. These macroscopic lengths include the connection length (qR typically of order several meters), the minor radius (typically an order of magnitude less than qR), and gradient scale lengths (typically $\sim$ 1cm or smaller within transport barriers). More over, NCT assumes that all gradient scale lengths are large compared to the gyroradius, which is often not the case in the edge region of enhanced confinement regime plasmas. As mentioned in the previous section,

standard NCT also ignores gyroviscosity which leads to a degenerate ambipolarity constraint. These notions can be formalized by considering the ratio of the parallel energy transport time to the perpendicular diamagnetic transit time[34]:

$$\Lambda_1 = \frac{q^2R^2}{\chi_{||,i}/N}\frac{\partial T_i}{eBr\partial r} = 0.255\frac{1}{\Omega_i\tau_i}\frac{q^2R^2}{rL_{T_i}} \tag{5.17}$$

where Ω_i is the Larmor frequency, and $\chi_{||,i}$ and τ_i are the Braginskii parallel heat conductivity and ion collision time respectively [35]. Standard NCT is derived assuming $\Lambda_1 = 0$ while sub-neoclassical theory (SNCT) considers Λ_1 small but finite. Substitutions and simplification of equation 5.17 gives

$$\Lambda_1 = 0.019\frac{A_i^{1/2}\left(Z_{eff}n_i\right)_{19}}{BT^{3/2}}\frac{q^2R^2}{rL_{T_i}} \tag{5.18}$$

where B is the magnetic field in Tesla, n_i density is in 10^{19} particles/m^3, T_i is temperature in electron volts, A_i is the atomic mass of the main ions, and R, r, and L_{T_i} are all in meters. Substituting typical values for the edge region of an Alcator C-Mod H-mode plasma (R = 0.7 m, r = 0.2 m, A_i =2, B = 5 T, q = 4, $Z_{eff}n_i = 4 \times 10^{19}m^{-3}$, T_i = 200 ev, L_T = 0.005 m) gives $\Lambda_1 = 0.06$. It can be shown that the SNCT correction to the neoclassical heat flux is of order $O(\Lambda_1^2)$, which in this case is quite small, suggesting that the added complexity of (SNCT) is unnecessary. However, it can also be shown that the difference between the ion and electron radial particle flux is proportional to Λ_1 (specifically, $\Gamma_i - \Gamma_e = \Lambda_1\gamma_i$ with $\gamma_i \approx \Gamma_i$). Since this flux difference is what determines the radial electric field, retaining a finite Λ_1 allows one to obtain a non-degenerate ambipolarity constraint. Put another way, it is the implicit assumption that $\Lambda_1 = 0$ made in standard NCT that gives rise to the degenerate ambipolarity constraint.

While it is possible to write out complete expressions for the sub-neoclassical toroidal rotation velocities and radial electric field[34] they are even longer and more complicated than their neoclassical counterparts and so they will be omitted (see reference [34] for full details). Comparison of the predictions of SNCT to experiment have had mixed results [36][37]. SNCT has had some success predicting the sign and

magnitude of flows, but it consistently under-predicts (by orders of magnitude) the time scales on which these flows develop. It is believed that the anomalously short momentum confinement times observed in experiment are due to plasma turbulence.

5.3 ICRF Induced Rotation

Many theories have been developed to explain the observation of co-current plasma rotation in ICRF heated plasmas [38] [39][40]. While each of these theories differ in detail, they all rely on a combination of direct momentum exchange between waves and particles and an ICRF wave induced non-ambipolar radial current. This radial current leads to charge separation which in turn causes changes to the radial electric field profile. Since E_r and V_ϕ are related through the radial force balance equation, a change in E_r can induce a change in V_ϕ, hence ICRF flow drive.

Comparison of these theories with experiment has had mixed results. For example, the theory put forward by Perkins et. al[38] predicted a toroidal rotation inversion when the ICRF resonance was scanned from the low field side to the high field side. In dedicated experiments on Alcator C-Mod this inversion was not observed[37]. Other theories have faired somewhat better, but the fact that very similar co-current rotation is seen in purely ohmic plasmas suggests that ICRF heating is only indirectly responsible for the rotation[41]. This possibility is discussed at greater length in chapter 6.

5.4 Accretion Theory

Accretion theory suggests that the observed intrinsic rotation in tokamaks results from an interaction between plasma particles and edge localized collective modes[42]. Specifically, particles traveling at the phase velocity of these collective modes are preferentially scattered to the wall. If the phase velocities have a preferred toroidal direction then scattered particles lost to the wall will take with them net angular momentum. In order for total angular momentum to be conserved, the plasma must

rotate in the direction opposite the phase velocity of the collective modes.

The theory seeks to explain the observed rotation inversion from L-mode to H-mode (counter current in L-mode, co-current in H-mode)[43][44] by the phase velocity direction of the dominant turbulence mechanism in each regime. It is argued that turbulence in L-mode plasmas is primarily due to ion temperature gradient modes (ITGs). These modes tend to have phase velocities in the co-current direction which leads to counter-current plasma rotation[45][46]. Conversely, it is argued that in H-mode plasmas ITG modes are largely suppressed and turbulence is driven by strong density gradients in the edge of the plasma. It is stated that these density driven modes have phase velocities in the counter-current direction which in turn gives rise to co-current rotation.

In addition to flow drive from edge localized turbulence, a momentum pinch mechanism is identified by considering electrostatic modes in slab geometry. The calculation begins by considering modes of the form

$$\hat{\phi} \approx \bar{\phi}(x_o) \exp(-i\omega t + ik_y y + ik_{||} z) \tag{5.19}$$

localized around a surface $x = x_o$. The perturbed parallel momentum conservation equation is then used to determine the dispersion relation for these modes. This calculation leads to the following form for the perpendicular momentum flux

$$\Gamma_k \approx -\frac{2\gamma_k}{\bar{\omega}_k^2} \langle |\hat{v}_{Ex}^{(k)}|^2 \rangle \left[m_i n \frac{dv_{||}}{dx} + 2\frac{k_{||}}{\bar{\omega}_k} \frac{dp_i}{dx} \right] \tag{5.20}$$

where $\bar{\omega} \equiv \omega - k_{||} v_{||}(x_o)$ is the Doppler shifted frequency, $v_{||}$ is the parallel flow velocity (assumed subsonic, i.e. $v_{||}/v_{thi} << 1$), $\gamma_k = \text{Im } \bar{\omega}_k$ is the mode growth rate and $D \equiv (2\gamma_k/\bar{\omega}_k^2)\langle |\hat{v}_{Ex}^{(k)}|^2 \rangle$ is the quasi-linear diffusion coefficient. In the equation above, the first term in the brackets gives rise to momentum diffusion, while the second term gives rise to a momentum pinch proportional to the ion pressure gradient[1].

[1] A similar theory has been put forth K.C. Shaing in which electrostatic fluctuations lead to a momentum pinch[47]

In summary, accretion theory puts forth a explanation for the rotation inversion observed during L-H transitions based on the phase velocity direction of turbulence at the plasma boundary. Additionally, it identifies a momentum pinch term proportional to the ion pressure gradient capable of giving rise to peaked rotation profiles.

5.5 Flow Drive via Reynolds Stress

Reynolds stress refers to off-diagonal terms in the pressure tensor induced by turbulent fluctuations. The turbulence based stresses are typically defined by considering each fluid quantity as composed of an average and fluctuating part, for example

$$v_{||} = \langle v_{||} \rangle + \tilde{v_{||}}. \tag{5.21}$$

where '$\sim$' represent fluctuating quantities and $\langle \cdot \rangle$ represent fluctuation averaged quantities. When the fluid equations are averaged on time scales large compared to the turbulence fluctuations one ends up with terms proportional to the average of the product of fluctuating quantities (i.e. $\langle \tilde{v}_{||} \tilde{v}_r \rangle$). It is terms such as this, related to the cross phase of fluctuating quantities, that give rise to Reynolds stresses.

Although the average of each fluctuating quantity is zero by definition, the product of two fluctuating quantities can be non-zero. In order for the Reynolds stress terms to be non-zero there needs to be a symmetry breaking mechanism. In their 2007 paper, Gurcan et al.[48] proposed radially sheared $\mathbf{E} \times \mathbf{B}$ velocity profiles as a potential source of symmetry breaking. They proceed to calculate both the diffusive and non-diffusive flux of parallel momentum driven by ITG turbulence in a cylindrical plasma. To their credit, the calculation is performed with a self-consistent radial electric field by taking into account the interaction between momentum transport via turbulent Reynolds stress and turbulence suppression via velocity shear. The calculation begins by considering the equation for the parallel mean velocity,

$$\frac{\partial}{\partial t} \bar{v}_{||} + \frac{\partial}{\partial x} \langle \tilde{v}_{Ex} \tilde{v}_{||} \rangle = \nu \frac{\partial^2}{\partial x^2} \bar{v}_{||} \tag{5.22}$$

where $\bar{v}_{||}$ is the mean parallel flow velocity, $\tilde{v}_{||}$ is the fluctuating parallel flow velocity, $\tilde{v}_{Ex}$ is the radial component of the fluctuating $\mathbf{E} \times \mathbf{B}$ velocity and ν is the collisional parallel viscosity. Following a quasi-linear closure scheme and assuming a linear response based on ITG turbulence the parallel stress is calculated to be

$$\langle \tilde{v}_{Ex} \tilde{v}_{||} \rangle = -Re \sum_k i v_{ti}^2 \rho_i k_y \left[\frac{v_{ti} k_y}{\omega_k} \frac{\rho_i}{v_{ti}} \frac{\partial}{\partial x} \bar{v}_{||} + \frac{v_{ti} k_y}{\omega_k} \frac{v_{ti} k_{||}}{\omega_k} \frac{\rho_i}{\bar{P}} \frac{\partial}{\partial x} \bar{P} - \frac{v_{ti} k_{||}}{\omega_k} \right] \left| \frac{e\tilde{\Phi}_k}{T_i} \right|^2 \tag{5.23}$$

The first term in this equation is the standard diffusion term. The second and third terms are so-called "off diagonal terms". Note that both of the off-diagonal terms are proportional to $k_{||}$, therefore if the the fluctuation spectrum is symmetric in $k_{||}$ the off-diagonal contribution to the sum will be zero. The fundamental result of this calculation is that the $\mathbf{E} \times \mathbf{B}$ shear causes the modes to shift off the x=0 resonant surface which gives rise to a breaking of the $k_{||}$ symmetry and hence an off-diagonal component of the parallel momentum flux.

In addition to $\mathbf{E} \times \mathbf{B}$ shear, magnetic curvature has been put forward as a mechanism for breaking $k_{||}$ symmetry[49]. Specifically it has been proposed that Reynolds stress can develop due to imperfect cancellation of curvature and grad-B drifts when fluctuation intensity varies on a flux surface. The calculation proceeds by considering the electrostatic toroidal non-linear gyro-kinetic equations with the assumption that $E_r' = 0$ and ignoring the effect of turbulence driven zonal flows. After a lengthy calculation, the radial component of the turbulent driven flux, Π_{ang}, of the ion parallel angular momentum density, $m_i n_0 U_{||} R$, is found to be of the form

$$\left\langle \Pi_{Ang}^{Turb} \cdot \nabla \psi \right\rangle = -\chi_{Ang} \left\langle (RB_\theta)^2 \frac{\partial}{\partial \psi} (m_i n_o U_{||} R) \right\rangle + V_{Ang}^{TurCo} \left\langle RB_\theta m_i n_0 U_{||} R \right\rangle \tag{5.24}$$

where the radial coordinate is designated by the poloidal flux ψ, χ_{Ang} represents the angular momentum diffusivity, and V_{Ang}^{TurCo} represents a novel turbulence driven convective pinch velocity. V_{Ang}^{TurCo} is shown to be composed of two different pinch

velocities. The first, V_{Ang}^{TEP}, is based on turbulence equipartition and is driven by $\nabla(1/B)$. This pinch term can be expressed as

$$V_{Ang}^{TEP} \approx -\frac{2F_{balloon}}{R_0}\chi_{Ang} \tag{5.25}$$

where $F_{balloon}$ is a dimensionless coefficient of order unity. For outward ballooning fluctuations $F_{balloon}$ is > 0 and therefore V_{Ang}^{TEP} gives rise to an inward pinch of angular momentum. The second novel pinch velocity, V_{Ang}^{CTh}, is based on curvature driven thermal flux from ion temperature fluctuations and is given by

$$V_{Ang}^{CTh} \approx -\frac{4F_{balloon}}{R_0}\left(\frac{\delta T_i}{e_i \delta\phi}\right)\chi_{Ang} \tag{5.26}$$

Since $\delta T_i/\delta\phi$ can be positive or negative, the sign of V_{Ang}^{CTh} depends on the cross phase between ion temperature and electric potential.

In summary, the Reynolds stress theories outlined above represent an important step forward in our understanding of momentum transport in tokamak plasmas. Given the anomalously high momentum diffusivities observed in experiment, it seems reasonable to assert that any theoretical treatment of momentum transport that ignores the role of turbulence could not possible be complete. However these turbulence effects depend sensitively on the magnitude and phase of fluctuating quantities that are extremely difficult to measure. As a result it will be very difficult to test them experimentally.

5.6 Summary of Rotation Theories

This chapter has sought to give a brief overview of the main theories being put forward to explain intrinsic rotation in tokamak plasmas. These theories can be broadly grouped into three categories: Theories based on Coulomb collisions, wave induced rotation theories, and theories based on plasma turbulence. The Coulomb collision theories are unable to predict accurately the time scale of momentum transport, typically overestimating them by an order of magnitude or more. The ICRF theories

do not explain why very similar co-current rotation is observed in ohmic H-mode discharges. The turbulence based theories depend sensitively on quantities that we are currently unable to measure. Therefore, despite progress in the theoretical description of plasma flows, the fact remains that our ability to make predictions of rotation in tokamak plasmas in the absence of strong NBI is based almost entirely on empirical grounds.

THIS PAGE INTENTIONALLY LEFT BLANK

Chapter 6

Intrinsic Rotation in Enhanced Confinement Regime Plasmas

Significant plasma rotation in both low and enhanced confinement modes has been studied on a number of tokamaks worldwide. A brief summary of the L-mode rotation results from these studies is made difficult by the tremendous variety of the phenomenology reported. Intrinsic rotation in L-mode has been shown to depend sensitively, and in complicated ways, on a number of parameters including magnetic topology, plasma density, magnetic field, plasma current, and ion temperature [50][24][51][52][53][54][55].

In contrast to the complexity of L-mode, intrinsic rotation in enhanced confinement regimes is relatively simple. On many machines, using a variety of heating techniques, intrinsic rotation in enhanced confinement regimes is observed to be in the co-current direction and positively correlated with plasma pressure. These results were first observed in JET[56] plasmas with ICRF heating in which a strong correlation between angular momentum density and ion pressure was observed. Shortly thereafter similar observation were made on Alcator C-Mod, showing a strong correlation between the change in rotation, ΔV, with the change in store energy, ΔW. Here Δ refers to the change in a quantity between the L-mode and H-mode portions of a discharge [43] and is illustrated in figure 6-1[43]. Further work on Alcator C-Mod demonstrated that this co-current change in toroidal rotation was seen not only with

ICRF heating but, also in purely ohmic discharges [43][57][58].

Similar results in ohmic plasmas have been observed on DIII-D [59][60] and COMPASS-D [61]. Taken together, these observations suggest that the observed co-current rotation in ICRF heated discharges is not the result of fast ion effects as is suggests by some theories[38][37].

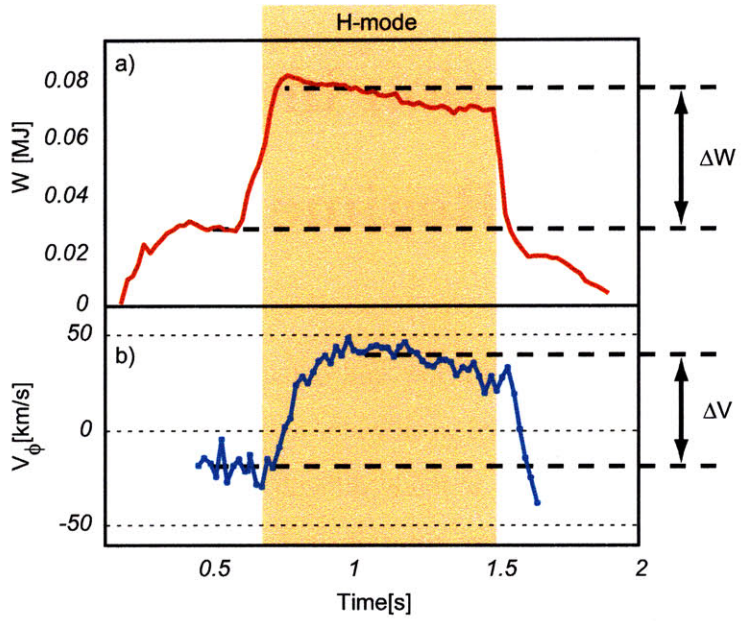

Figure 6-1: Traces of a) plasma stored energy, and b) central toroidal rotation showing the definitions of ΔW and ΔV.

Related experiments on Alcator C-Mod investigated the temporal evolution of intrinsic rotation during the transition from L-mode to H-mode. Three single-chord x-ray spectrometers were used to measure time histories of toroidal rotation at r/a $\approx$ 0.0, 0.3 and 0.6. Immediately following an L-H transition the co-current increase in toroidal rotation appeared on the outermost channel first, with the central channels lagging behind by tens of milliseconds (comparable to the energy confinement time)[62]. This result indicates that the rotation is generated by an edge localized source. Subsequent experiments on Alcator C-Mod using the Hirex-Sr spectrometer have confirmed this important result. Figure 6-3 shows an example toroidal rotation profile evolution through an L-H transition as measured by Hirex-Sr.

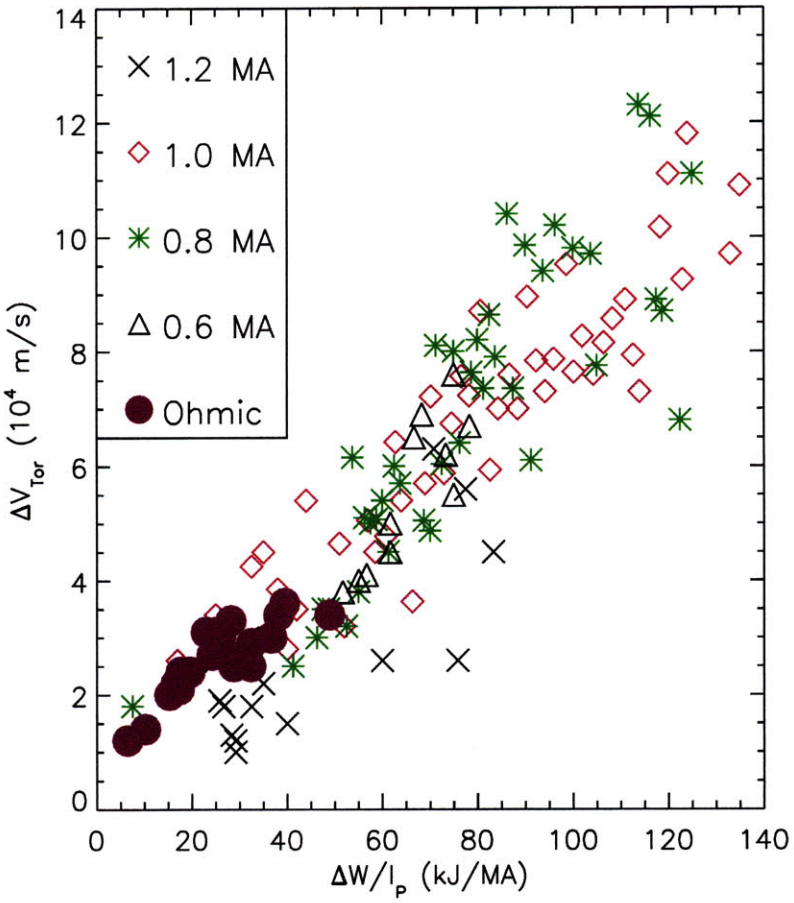

Figure 6-2: Change in toroidal rotation velocity (the difference between the H mode and pre-H mode values) as a function of the change in plasma stored energy normalized to plasma current for ohmic and ICRF (with on axis heating) H modes. The ohmic values are all shown as purple circles, unseparated in plasma current, while the ICRF points are indicated by different symbols for the various plasma currents: black crosses for 1.2 MA, red diamonds for 1.0 MA, green asterisks for 0.8 MA and black triangles for 0.6 MA. Figure and caption are reproduced from reference [41], figure 2.

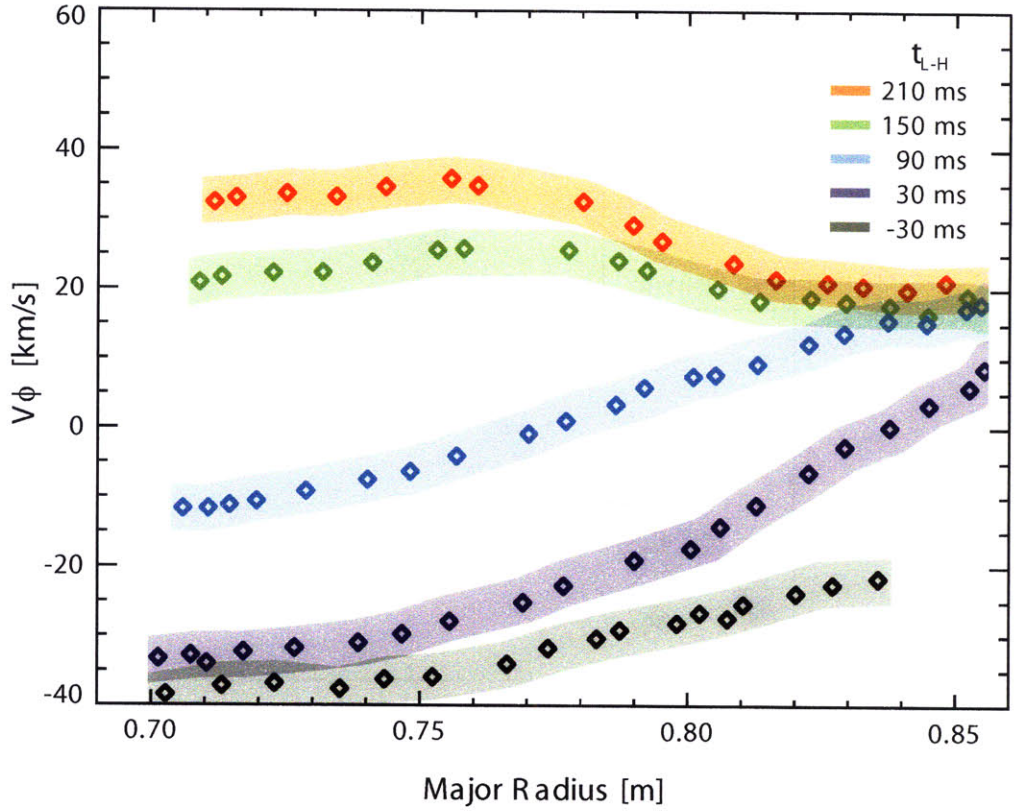

Figure 6-3: Toroidal rotation evolution through an L-H transition. The times associated with each profile are referenced to the L-H transition time, t_{L-H}.

Another important result to come out of the Alcator C-Mod studies was the inverse relationship between ΔV and plasma current, i.e. $\Delta V \propto \Delta W/I_p$. Figure 6-2 shows this scaling (often referred to as the Rice scaling) for both ohmic and ICRF heated C-Mod discharges with a wide range in plasma current[41]. The success of these experiments motivated similar studies on other tokamaks. Figure 6-4 shows the C-Mod data from figure 6-2 plotted along with rescaled data from subsequent DIII-D and Tore Supra publications[60][63]. Figure 6-4 shows that all three machines are well characterized by the Rice scaling however, each machine has a different scaling coefficient.

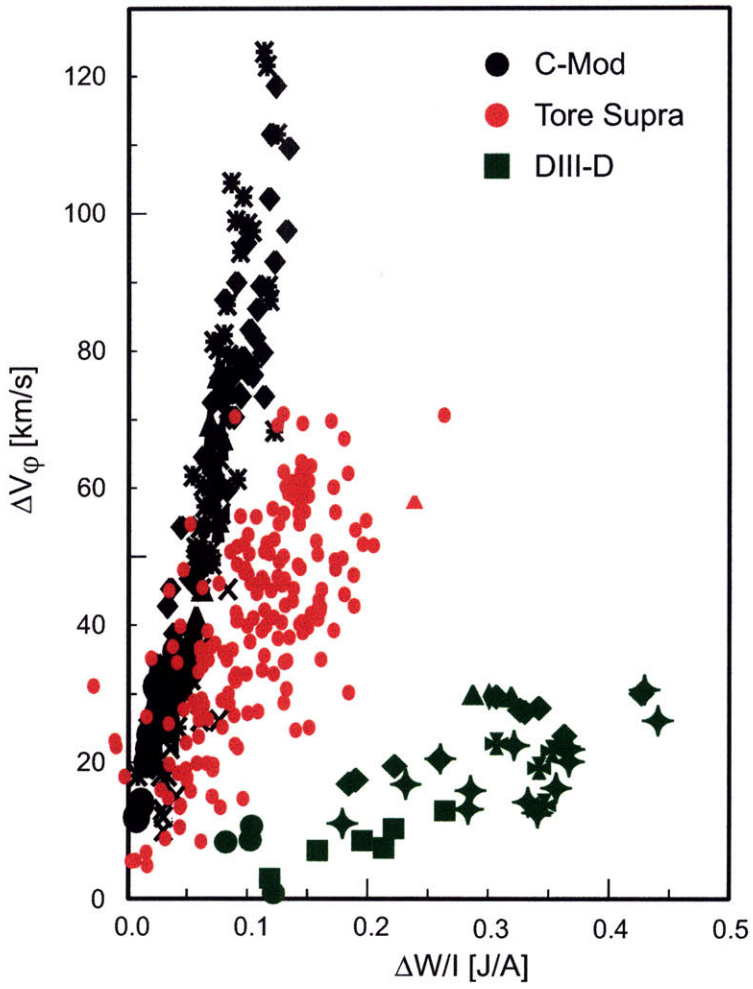

Figure 6-4: A synthesis of published results of the Rice scaling from 3 tokamaks (DIII-D [60] figure 8, Tore Supra [63] figure 3, and Alcator C-mod [41] figure 2

6.1 Multi-Machine Intrinsic Rotation Database

In an effort to characterize further intrinsic rotation in enhanced confinement regimes, a multi-machine database was constructed with results from six different tokamaks (JET, JT60-U, Tore Supra, DIII-D, TCV and Alcator C-Mod)[8]. The goal of this project was to determine an empirical scaling relation for intrinsic rotation based on statistical techniques similar to those used in energy confinement times studies[64][65]. The parameters chosen for this database were all global quantities (plasma current, stored energy etc.) even though the precise mechanism by which the intrinsic rotation is generated almost certainly depends on local quantities. This approach was taken because global quantities tend to be measured both more frequently and more accurately than local quantities. Table 6.1 shows the range of some of the parameters included in the database.

Table 6.1: Intrinsic Rotation Database Parameter Ranges

Device	**V** km/s	Ω kR/s	W_P MJ	**R** m	**a** m	B_T T	I_P MA	β_N	ρ^* $\times 10^{-3}$	**Notes**
C-Mod	0-130	0-200	0-0.23	0.67	0.21	5.4	0.6-1.2	0.5-1.2	5-8	ICRF, OH
DIII-D	0-30	0-20	0-0.6	1.66	0.67	1.8	1.0-1.5	0.2-1.4	2-4	ECH,OH r/a = 0.8
JET	0-60	0-20	0-4	2.96	1.25	2.8	3.0	0.5-0.7	2-3	ICRF
JT-60U	0-120	0-35	0-0.5	3.4	1.0	3.8	1.2	0.05-0.22	1-2	ECH/ LH(ITB)
TCV	0-35	0-40	0.04	0.88	0.25	1.4	0.3	0.8-2.0	9-14	ECH, OH
Tore Supra	0-80	0-35	0-0.8	2.34	0.78	3.6	0.8-1.5	0.5-1.2	2-4	ICRF
ITER	?	?	250	6.2	2.0	5.3	15	2.6	1.5	ICRF/ ECH

One common technique used when trying to unify seemingly disparate sets of data is to recast the problem in terms of non-dimensional quantities. For rotation velocity in a magnetized plasma there are four obvious normalizations; the electron thermal

speed, the ion thermal speed, the Alfvén speed and the ion acoustic speed. These normalizations give rise to the ion thermal Mach number ($M_i \equiv V_\phi/v_i$), the electron thermal Mach number ($M_e \equiv V_\phi/v_e$), the Alfvén Mach number ($M_i \equiv V_\phi/C_A$) and the ion acoustic Mach number ($M_S \equiv V_\phi/V_S$) respectively. Here C_A is the Alfvén speed ($\approx B_\phi/\sqrt{\mu_o n_e m_D}$), v_e is the electron thermal speed ($= \sqrt{T_e/m_e}$), v_i is the ion thermal speed ($= \sqrt{T_i/m_{ave}}$), C_S is the ion acoustic speed and $m_{ave} \approx m_D \left[1 - (Z_{eff} - 1)/Z_I\right]$ is the average ion mass, assuming a dominant impurity species of charge Z_I. A derivation of this expression and a definition of C_S can be found in appendix F. The expression $\left[1 - (Z_{eff} - 1)/Z_I\right]$ amounts to about a 20% correction for the highest Z_{eff} cases in the database. The stored energy (or plasma pressure) can be normalized with respect to the energy density of the magnetic field using the dimensionless quantity $\beta_T \equiv \frac{2\mu_o \langle p \rangle}{B_o^2}$, where $\langle p \rangle$ is the average pressure. Given the I_p^{-1} dependance of the Rice scaling, it is natural to consider the MHD stability parameter "normalized beta" given by $\beta_N \equiv \beta \frac{aB_o}{I_p}$. Figure 6-5 show the ion thermal Mach number as a function of β_N for the six machines included in the database[1].

From figure 6-5 it is clear that for all machines the ion thermal Mach number increases with β_N, although there is variation in the constants of proportionality. With the exception of the JT60-U data, the dimensionless scaling M_i vs. β_N (figure 6-5) seems to overlay the data to a greater degree than does the original Rice Scaling (figure 6-4). The particular JT60-U discharges used in the database were quite different from the plasmas generated on the other machines in that they had electron temperature ITBs, no edge pedestal, $T_e >> T_i$ as well as very low densities and βs. Scalings using the electron thermal Mach numbers, and ion acoustic Mach numbers gave very similar results to those displayed in figure 6-5.

Plotting the Alfvénic Mach number vs. β_N (figure 6-6) seems to do a better job unifying the data than does the ion thermal Mach number. It is worth mentioning at this stage that "normalized β", β_N, actually has units of $[\%Tm/MA]$. β_N can be made dimensionless simply be dividing by μ_o and motivates the following definition:

[1]The Alcator C-Mod data used in this database is from a single chord, tangentially viewing, cylindrically bent crystal spectrometer[43]

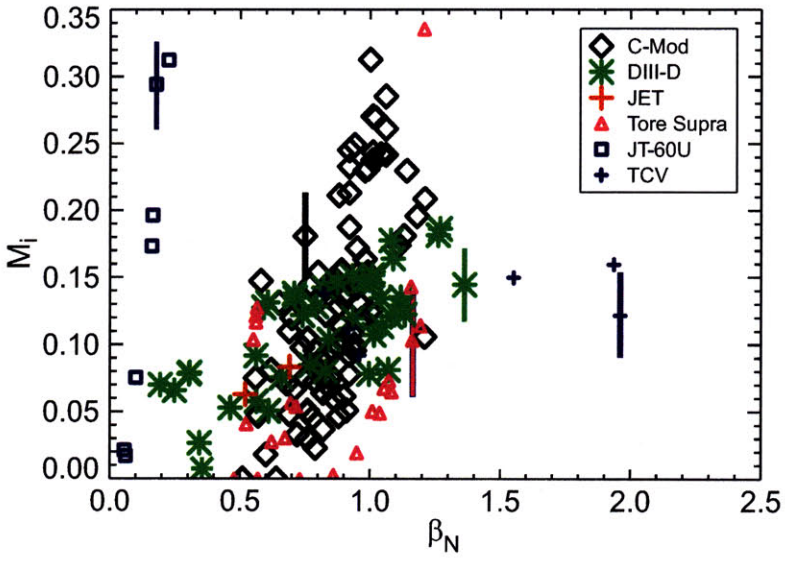

Figure 6-5: The ion thermal Mach number vs. β_N for C-Mod (black diamonds), DIII-D (green asterisks), JET (red + signs), JT-60U (blue squares), TCV (blue + signs) and Tore Supra (red triangles). Typical error bars are shown.

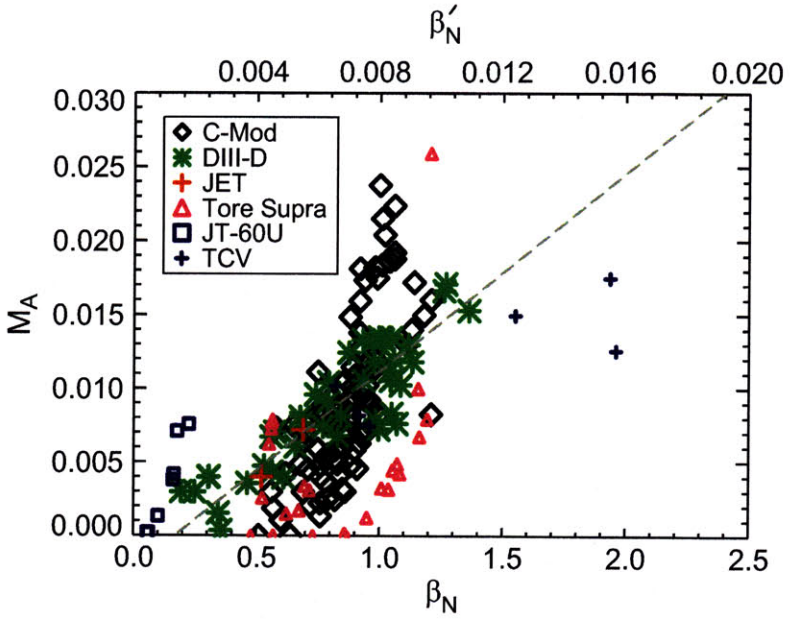

Figure 6-6: The Alfvén Mach number as a function of β_N (and β'_N), with the same legend as figure 6-5. The line represents the best linear fit with all points given equal weighting.

$$\beta_N' \equiv \beta_N/\mu_o = \beta\frac{aB_o}{\mu_o I} = \frac{1}{2\pi\kappa}\frac{B_o}{\bar{B}_\theta(a)}\beta \tag{6.1}$$

where $\bar{B}_\theta(a)$ is the average poloidal field at the plasma boundary. The variable β_N' can be evaluated numerically as $\beta_N' = \beta_N/40\pi$. Interestingly, when the Alfvénic Mach number is plotted vs. β_N' the line of best fit through the data has a slope of order unity (see top abscissa in figure 6-6). In addition to β_N, the relationship between various Mach numbers and normalized gryo-radius $\rho^*(\equiv r_L/a = 1.02 \times 10^{-4}\sqrt{\mu_{AMU}T_{eV}}/[B_{o,T}a_m)])$ were investigated (see figures 6-7 and 6-8). Since there is relatively little variation in $\sqrt{T}$, the data for any given machine in these figures are confined to a narrow region of ρ^*, with the machines being sorted in $B_o a$. Plots of various Mach numbers vs. collisionality ($\nu^* = 9.56\times10^3 n(10^{20}m^{-3})qZ_{eff}R(m)/[T(eV)^2a(m)^{3/2}]$) are similarly unhelpful in elucidating any broad trends in the data (see figures 6-9, 6-10). Taken together, figures 6-5 through 6-10 suggest that the intrinsic rotation does not depend directly on the dimensionless transport variables ν^* and ρ^*, but does scale strongly with the MHD quantity β_N. It remains an open question whether or not the strong scaling between intrinsic rotation and β_N is simply a coincidence or is indicative of fundamental connection with MHD activity.

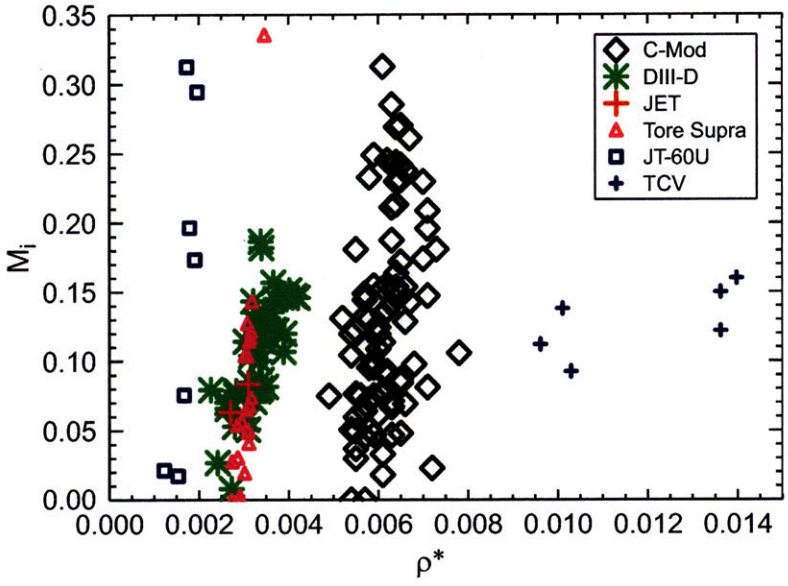

Figure 6-7: Ion Thermal Mach Number vs. Normalized Gyro-radius

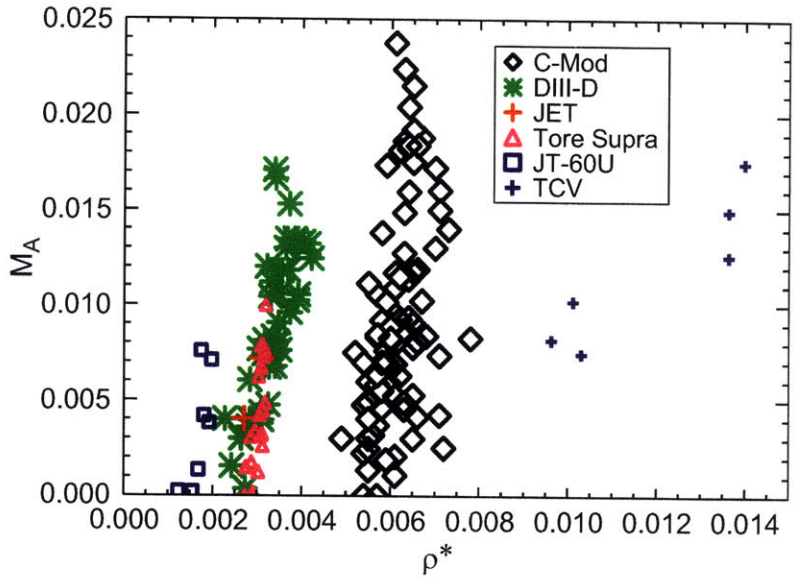

Figure 6-8: Alfvénic Mach Number vs. Normalized Gyro-radius

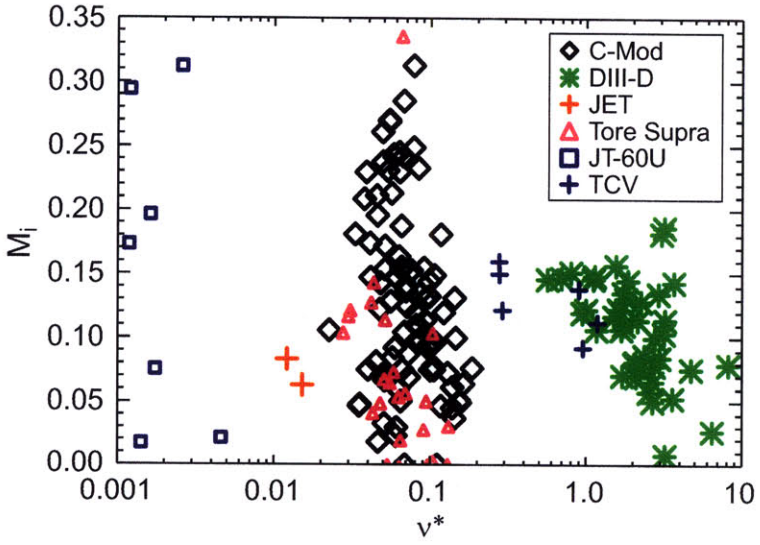

Figure 6-9: Ion thermal Mach number vs. collisionality

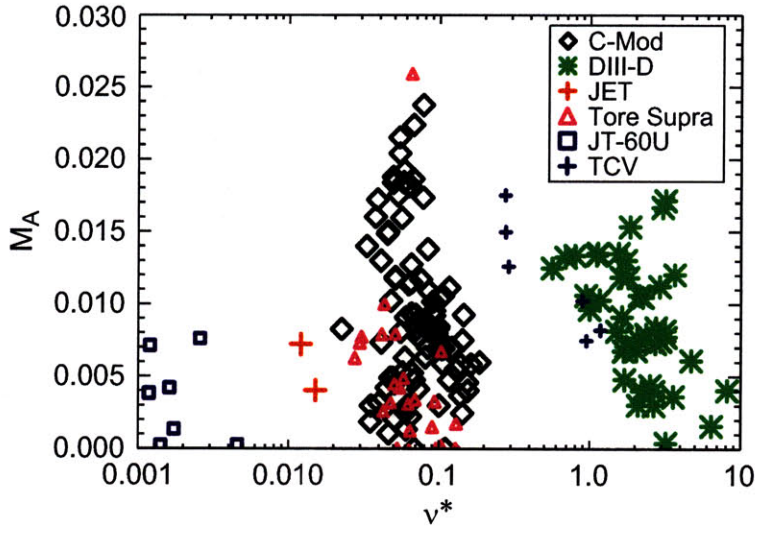

Figure 6-10: Alfvénic Mach number vs. collisionality

Plotting various dimensionless quantities against one another can give a general impression of the relationship between the variables in question, however, it only allows two quantities to be compared at a time. A more systematic approach involves using multivariate regression analysis to look for correlations between all variables simultaneously. This is accomplished by assuming that the dependent variable (in this case velocity or Mach number) can be expressed in the form of a power law:

$$y_i = \prod_j x_{i,j}^{\alpha_j} \tag{6.2}$$

where y is the dependent variable, x represents independent variables and α_j are constants to be determined. Here the subscript j refers to the j^{th} independent variable and i represents the i^{th} measurement. The advantage of assuming this form is that it can be readily linearized by taking the natural logarithm of equation 6.2. This gives

$$\ln(y_i) = \sum_j \alpha_j \ln x_{i,j} \tag{6.3}$$

If we now define new variables $y_i' \equiv \ln y_i$ and $x_{i,j}' \equiv \ln x_{i,j}$ we obtain

$$y_i^{'} = \sum_j \alpha_j x_{i,j}^{'} \tag{6.4}$$

Since this is the form of a linear system it is possible to use standard multivariate regression techniques to determine the values of the coefficients, α_i, that best fit the data in a 'least squares' sense. This type of analysis was performed on the intrinsic rotation database using dimensionless parameters and generated the scaling $M_A = 0.65\beta_T^{1.4} q_*^{2.3}$, where $q_* \equiv 2\pi\kappa a^2 B/\mu R I_p$. The measured Alfvénic Mach number vs this scaling is shown in figure 6-11. While there is clearly some variation in slope between the machines, almost all of the data fall within a factor of two of the scaling. Extrapolation of this scaling to ITER predicts $M_A \geq 0.02$ for both inductive and non-inductive scenarios.

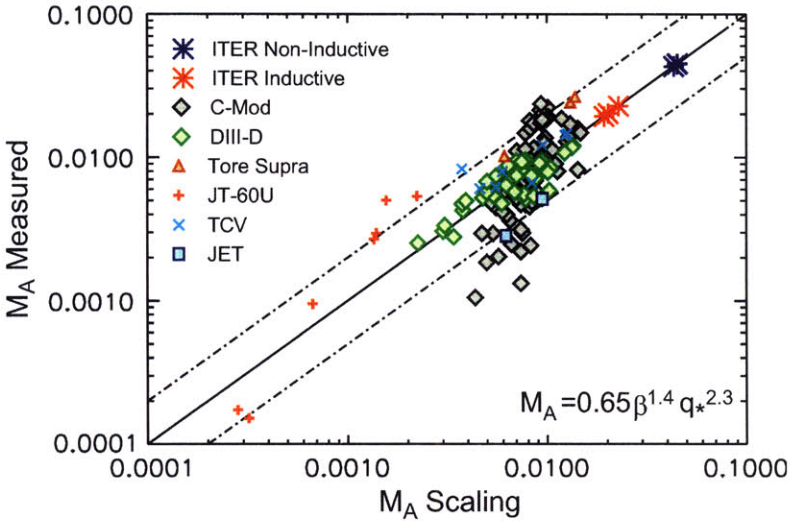

Figure 6-11: Measured Alfvénic Mach number vs. the scaling $M_A = 0.65\beta_T^{1.4} q_*^{2.3}$. Dashed lines show a factor of 2 difference from the scaling.

A similar analysis was performed using dimensional parameters and generated the following scaling: $\Delta V = 0.9 B_o^{1.1} \Delta \langle p \rangle^{1.0} I_p^{-1.9} R^{2.2}$, with ΔV in [km/s], B in [T], $\Delta \langle p \rangle$ in [kPa], I_p in [MA] and R in [m]. The results of this scaling are shown in figure 6-12. This scaling brings data of all machines into rather good agreement and with the exception of the JT60-U, all machines have approximately the same slope.

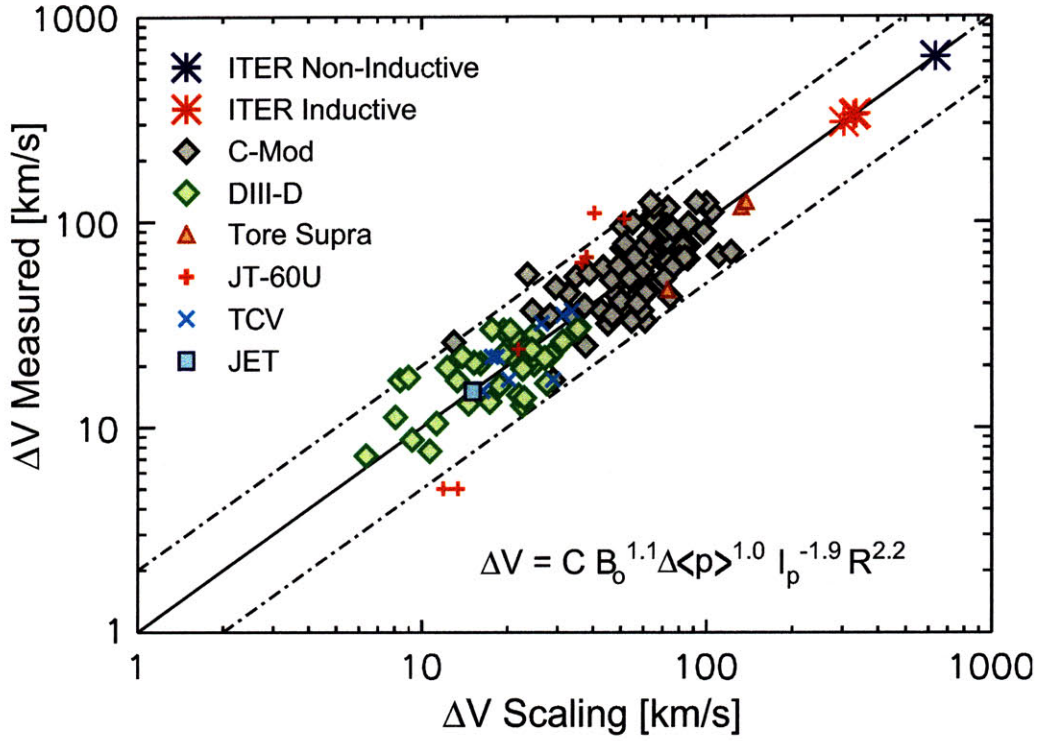

Figure 6-12: Measured change in toroidal rotation vs. the scaling $\Delta V = 0.9 B_o^{1.1} \Delta \langle p \rangle^{1.0} I_p^{-1.9} R^{2.2}$

Perhaps the most important implication of the dimensional and dimensionless scalings is that when extrapolated to ITER relevant parameters then both predict substantial intrinsic rotation (i.e. a few hundred km/s, or equivalently $\sim 2\%$ of the Alfvén speed). Theoretical predictions suggest that a few percent of the Alfvén speed is what is required for resistive wall modes (RWM) stabalization [66][67]. Recent results on DIII-D suggest that Alfvénic Mach numbers as low as 0.3% may be sufficent for RWM suppression[68]. These types of empirical scalings are undoubtedly crude tools, and predictions based on extrapolations should be viewed with some skepticism. That being said, even the most conservative extrapolations of any of the scalings presented here suggest Alfvénic Mach numbers well in excess of 0.03%.

6.2 Chapter Summary

This chapter has given a brief overview of the experimental characterization of intrinsic rotation in enhanced confinement modes of plasma operation. Unlike L-mode, plasma rotation in enhanced confinement regimes has a relatively simple dependence on macroscopic plasma parameters which can be quantified in terms of empirical scaling relations. A multi-machine database covering a wide range of plasma sizes, currents, field strengths, temperatures, densities, and heating types has demonstrated the universality of co-current rotation in enhanced confinement mode plasmas. The fact that such similar results are seen in plasmas all forms of heating suggests that it is the plasma gradients themselves that are responsible for the rotation. This intrinsic rotation will almost certainly help plasma performance in future machines through suppression of RWM and/or reduce turbulence through $\mathbf{E} \times \mathbf{B}$ shearing. There is, however, no obvious way to control the magnitude or shape of the rotation profile. Chapters 7 and 8 will discuss potential methods for achieving rotation profile control via the application of LH waves and ICRF mode conversion flow drive respectively.

Chapter 7

Lower Hybrid Wave Induced Rotation Profile Modification

Flows associated with lower hybrid current drive (LHCD) have been observed in both L-mode and H-mode discharges on Alcator C-Mod when lower hybrid waves are launched such as to drive positive current. These changes to the toroidal rotation profile are core localized ($r/a < 0.4$) and always in the counter-current direction. When the waves are launched against the inductive toroidal electric field, very little current is driven and no effect on the rotation profile is observed. This result indicates that it is the LHCD (as opposed to heating) that is responsible for the counter-current change in toroidal rotation. In discharges with sufficient LHCD, a region of high velocity shear forms concurrently with a negative increment in the radial electric field profile.

The lower hybrid system on Alcator C-Mod consists of an 88 wave guide launcher capable of delivering up to 1.2MW of power at 4.6 GHz with an $n_{||}$ range of 1.5-4 in either direction (Here $n_{||}$ is the refractive index of the injected LH waves parallel to the magnetic field).

7.1 Temporal Evolution

Shown in figure 7-1 are the temporal evolution of selected parameters for an L-mode discharge in which the injection of lower hybrid waves caused a strong counter-current change in the toroidal rotation (solid lines). The dashed lines in figure 1 represent a similar discharge in which no lower hybrid waves were injected. 600kW of lower hybrid power (with $n_{||}$ =1.6) was coupled to the plasma at t = 0.8 s. Immediately following the application of LH power, the central toroidal rotation began to evolve on a time scale considerably longer than the energy and momentum confinement times ($\sim$ 20 ms) but comparable to the current redistribution time[69] ($\tau_{CR} = 1.4\kappa a^2 T_{e,k}^{\frac{3}{2}}/Z_{eff} \sim 150ms$). The ability to sustain LHCD for many current redistribution times makes it possible to study the induced rotation in plasmas with fully relaxed current density profiles.

Modification of the toroidal rotation profile by LHCD has been observed over a range of electron density, plasma current, magnetic field, and lower hybrid power. Although the magnitude of the effect depends on these parameters, in every instance the change in toroidal rotation is in the counter-current direction. In discharges initially rotating in the co-current direction (as in figure 7-1) the application of LHCD can cause the rotation to change sign. While the precise mechanism by which the lower hybrid waves affect the rotation profile remains unclear, rotation inversions such as these can not be explained solely by changes in viscous damping (an increase or decrease in viscous damping would change the magnitude of the flow but not its sign).

7.2 LH Induced Rotation Modifications and Normalized Internal Inductance

Also of interest is the change in normalized internal inductance, l_i (a measure of the peakedness of the current density profile[70], given by the ratio of the volume averaged to surface averaged poloidal magnetic energy). The motional Stark effect (MSE) diagnostic was not available for these discharges and as a result, knowledge

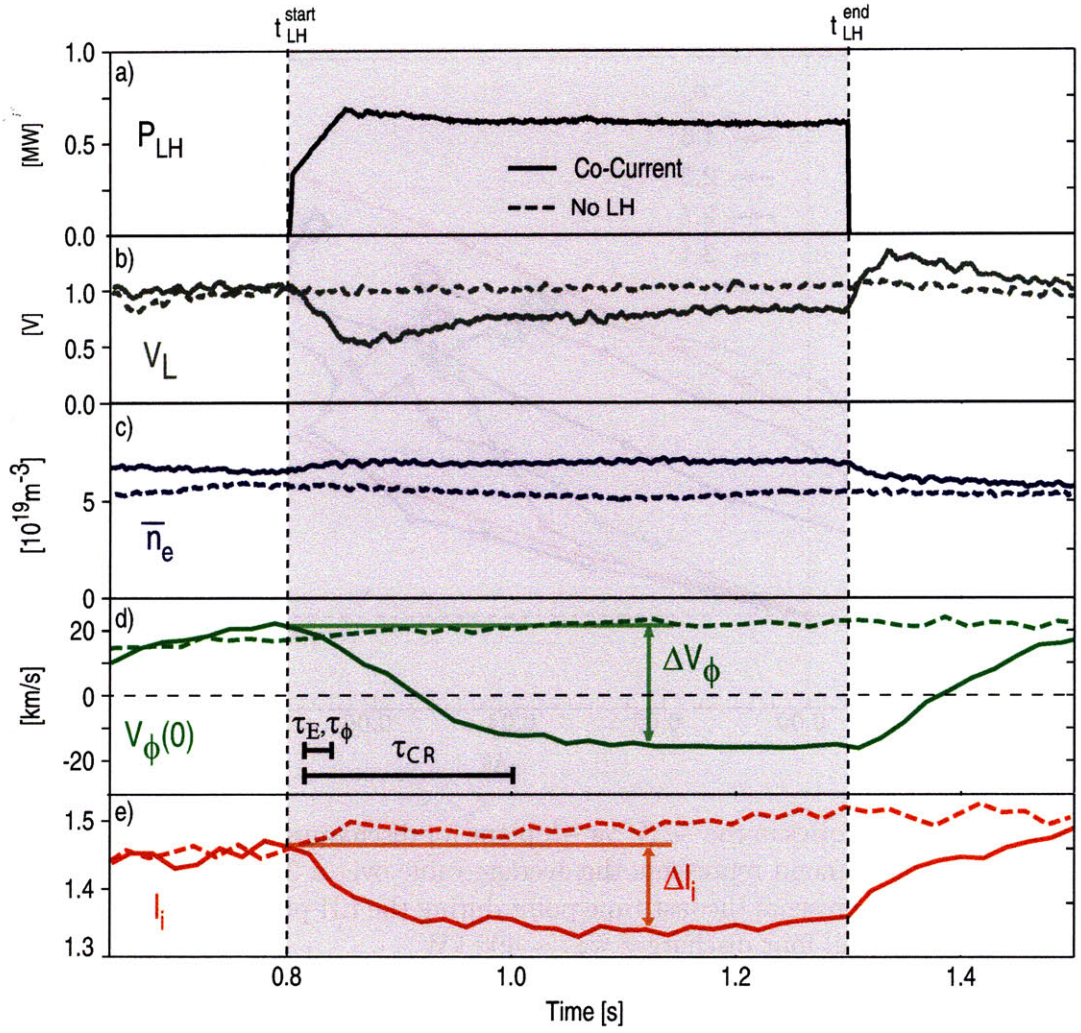

Figure 7-1: Time histories of a) lower hybrid power, b) surface loop voltage, c) line averaged density, d) central toroidal rotation velocity and e) the normalized internal inductance for discharges with LHCD (solid lines) and without LHCD (dashed lines). Both discharges had the same magnetic field (5.4 T) and plasma current (800 kA).

of the current density profile is limited to global quantities such as l_i and changes in loop voltage. The decrease in l_i from 0.8 s to 1.3 s indicates that the current density profile is becoming less peaked due to the off-axis current being provided by the lower hybrid waves.

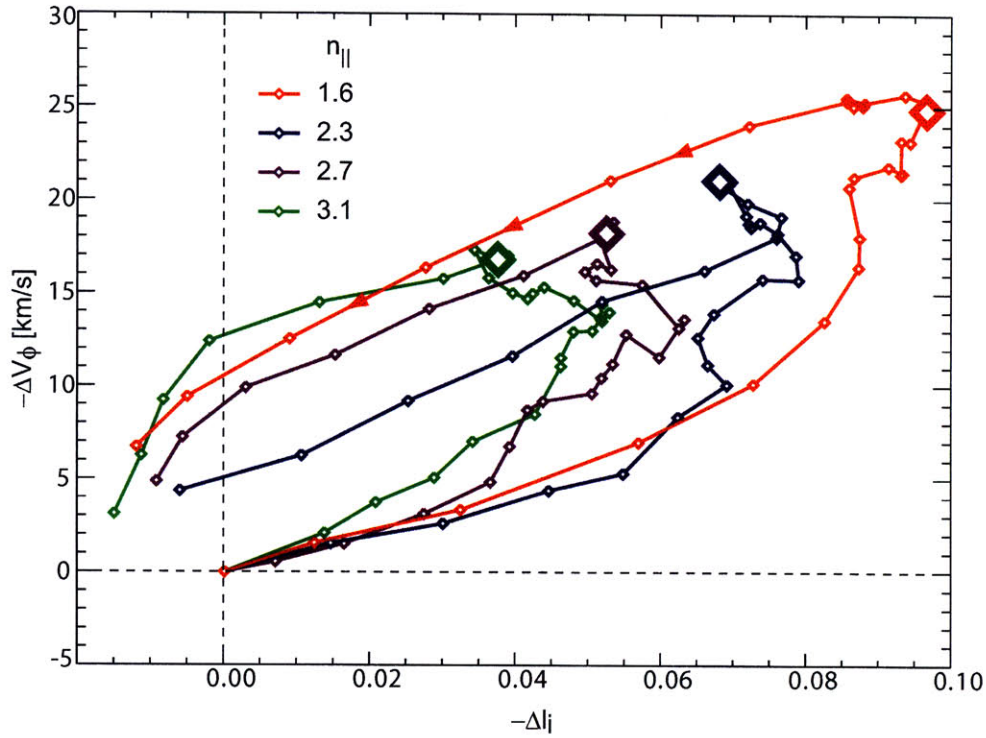

Figure 7-2: Trajectories in the $-\Delta V$ vs $-l_i$ plane for discharges with LHCD at varying $n_{||}$. Each small diamond represents the average value over a 20 ms time period. The large diamonds represents the last time point during the LH phase for each discharge. The LH power in all four discharges was $\sim$ 400 kW.

The quantity Δl_i shown in figure 7-1 is defined as the change in the internal inductance relative to the start time of the LHCD pulse (ΔV_ϕ is defined similarly). Figure 7-2 shows trajectories in the $-\Delta V_\phi$ vs $-\Delta l_i$ plane for identical target discharges with varying values of $n_{||}$ of the launched LH waves.

These trajectories all start at the origin (since $\Delta V_\phi(t_{LH}^{start}) = l_i(t_{LH}^{start}) = 0$ by definition) and progress in a counter-clockwise pattern indicating that ΔV_ϕ tends to lag behind Δl_i. There is also a clear trend in $n_{||}$, with smaller $n_{||}$ giving larger excursions in ΔV_ϕ and Δl_i. This trend can be explained by the fact that LHCD

efficiency is proportional to $1/n_{||}^2$. Thus waves launched with lower $n_{||}$ give rise to a larger change in Δl_i even though the associated LHCD profiles are less hollow.

The correlation between changes in central toroidal rotation and normalized internal inductance is observed in a wide variety of plasmas. This is illustrated in figure 7-3 in which ΔV_ϕ and Δl_i data are plotted for discharges with varying magnetic field, plasma current, density, magnetic topology, confinement regimes, lower hybrid power and launched $n_{||}$.

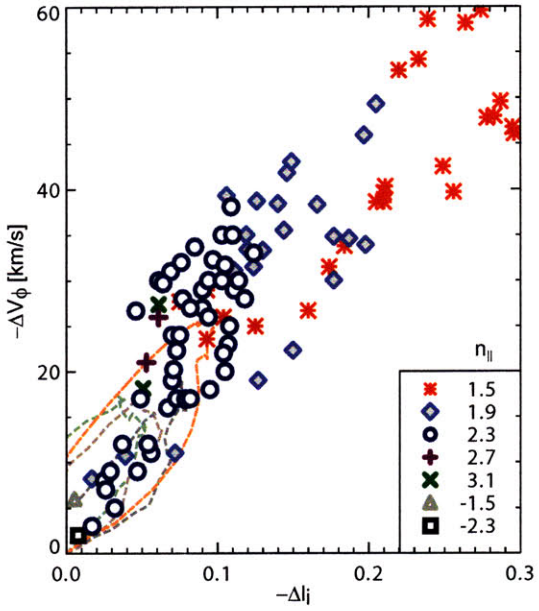

Figure 7-3: LH induced changes in central toroidal rotation and normalized internal inductance for a wide variety of plasmas (Each point represents a single discharge). The trajectories from figure 7-2 (dashed lines) are included for comparison.

7.3 LH Induced Rotation Modification in H-mode Plasmas

Modification of the toroidal rotation via the application of LH waves is also observed in H-mode plasmas. Time histories from just such a discharge are shown in figure 7-4. Shortly after the application of $\sim 1.5MW$ of ICRF power the plasma transitioned into H-mode ($t \sim 0.75s$). After this transition the central toroidal rotation is observed

to increment in the co-current direction by an amount consistent with the previously described Rice scaling of intrinsic rotation. At $t = 1.1s$ the lower hybrid system is turned on and the toroidal rotation is seen to increment in the counter-current direction. As in the L-mode case, this lower hybrid induced counter-current increment in toroidal rotation evolves on a time scale considerably longer than the energy and momentum time scales.

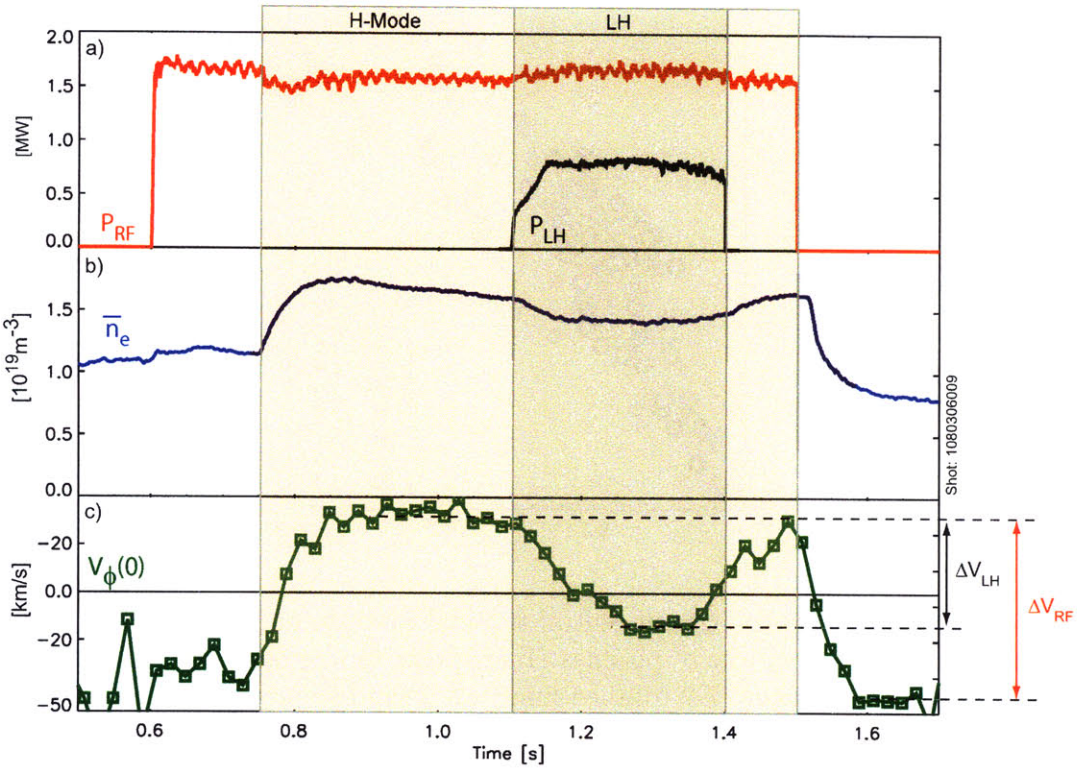

Figure 7-4: Time histories of a) LH and ICRF power, b) line averaged density, and c) central toroidal rotation velocity. Both the magnetic field ($B_\phi = 5.4$ T) and plasma current ($I_p = 600$ kA) were steady through the discharge.

This discharge suggests that the rotation drive associated with enhanced confinement regimes (co-I_p) and the rotation drive associated with LH (counter-I_p) can coexist. More over, it appears that the net toroidal rotation is simply a linear superposition of the rotation associated with each drive mechanism.

7.4 Spatial Extent of Rotation Modifications

The modification of the toroidal rotation profile by LHCD tends to be core localized, with the largest changes occurring in the range $0 < r/a < 0.4$. The sawtooth averaged radial profiles of n_e, V_ϕ , T_e, T_i and E_r both before and during the application of LHCD are shown in figure 7-5. The radial electric field, E_r, was calculated by measuring all other terms in the radial force balance equation as described in chapter 4. The change in the radial electric field profile indicates that there is a non-ambipolar radial current charging the plasma negatively with respect to its pre-LH state. Figure 7-6 compares the radial electric field profile evolution in discharges with and without LHCD.

7.5 Lower Hybrid Induced Fast Electron Pinch

A possible explanation of this negative charging of the core is a resonant trapped electron pinch[71], [72]. This pinch results from the canonical angular momentum absorbed by resonant trapped electrons while interacting with lower hybrid waves. Since the trapped resonant particles cannot on average carry toroidal mechanical angular momentum, the added momentum can only be realized by a change in the electron vector potential, and so they are forced to drift radially inwards. This mechanism can be thought of as a "Ware pinch"-like effect operating on resonant trapped electrons. The Ware pinch is automatically ambipolar because it is based on the $\mathbf{E} \times \mathbf{B}$ drift associated with the toroidal electric field and the poloidal magnetic field[73]. In the LHCD case, however, the resonant electrons experience a larger electric field than the ions and therefore a faster drift. This in turn, gives rise to a non-ambipolar inward radial drift of electrons, and therefore negative charging of the core. A pinch of resonant electrons is consistent with the observation that no change in radial electric field is seen when LHCD is applied in the counter-current direction. In this situation, virtually no fast electrons are produced because the LHCD is countered by the opposing Ohmic electric field. With no fast electrons there can be no fast electron pinch.

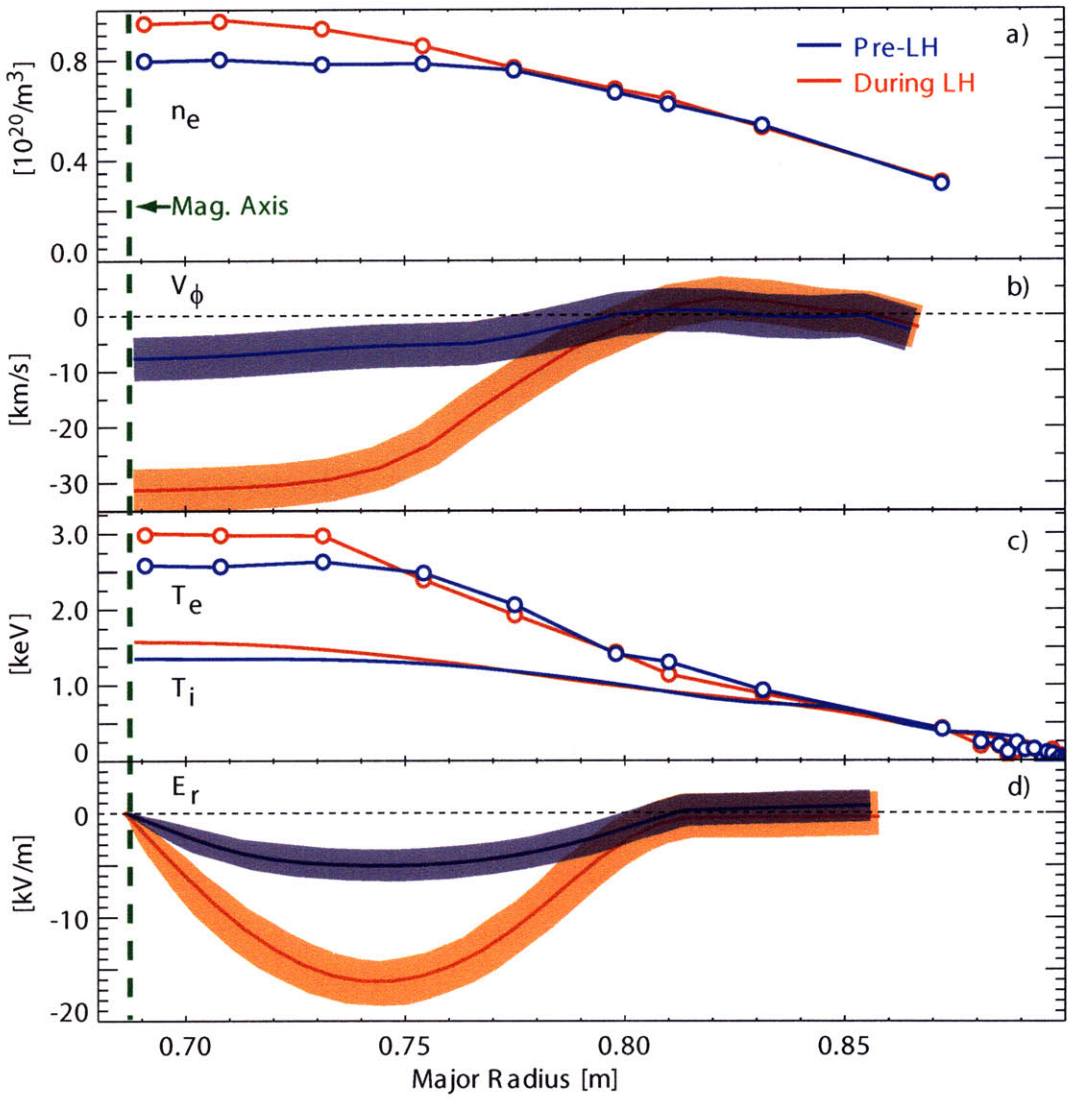

Figure 7-5: Profiles of a) electron density, b) toroidal velocity, c) electron and ion temperature and d) inferred radial electric field both before and during the application of LHCD.

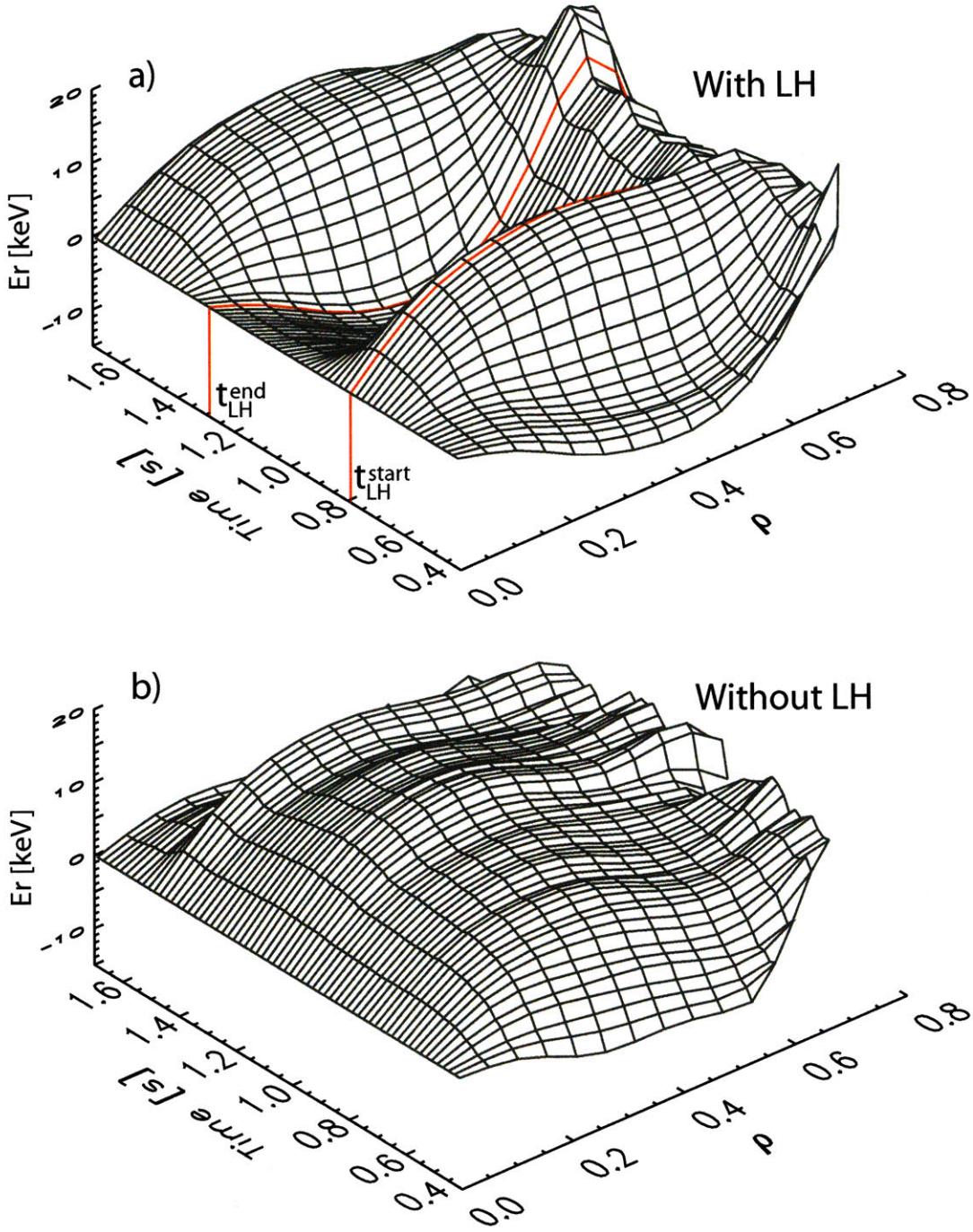

Figure 7-6: Comparison of the radial electric field profile evolution in a discharge with and without LHCD. The radial electric field at the start and stop times of the LH pulse are shown in red.

Regardless of the details of the electron pinch mechanism, as the plasma charges up negatively, the radial electric field is modified so as to oppose this charge separation. This negative increment in the radial electric in turn drives counter-current toroidal rotation via radial pressure balance. In steady state, the negative charging due to the electron pinch is balanced by a return current produced by the altered radial electric field.

7.6 Chapter Summary

Lower hybrid waves have been shown to induce strong modifications to the toroidal rotation profiles in both L-mode and H-mode discharges. These modifications evolve on a time scale comparable to the current redistribution time, are core localized ($r/a < 0.4$), scale linearly with lower hybrid power, and are well correlated with changes in normalized internal inductance. A counter-current modification of the rotation profile implies a negative increment in the radial electric field. This modification of the radial electric filed is consistent with an inward pinch of resonant trapped electrons.

Regardless of the precise mechanism that gives rise to this phenomenon, it is clear that lower hybrid waves can be used to modify toroidal rotation profiles. In terms of the implications for future devices, such as ITER and DEMO, it remains to be seen how the effect will scale. If there is a favorable scaling to large devices, this phenomenon could prove to be helpful for advanced scenario development by providing a method for tailoring the toroidal rotation and radial electric field profiles.

Chapter 8

ICRF Mode Conversion Flow Drive

Mode conversion (MC) refers to a process in which energy is transferred from one type of wave to another. This can occur when a wave is traveling through an inhomogeneous plasma and simultaneously satisfies the dispersion relation of two types of waves [74][75]. In a deuterium plasma with a small fraction of ^3He, fast magnetosonic waves can mode convert into short wavelength, slow waves, specifically ion cyclotron waves (ICW) and ion Bernstein waves (IBW)[76][77][78][79]. These waves are then absorbed (via ion cyclotron resonance for ICWs and electron Landau damping for IBWs) resulting in heating of both electrons and ions.

It has been predicted that in addition to heating, the absorption of mode converted waves can also drive plasma flows[80][81][82]. Experiments on TFTR showed some indication of mode converted IBWs driving poloidal flow, however it was not possible to exclude the possibility that these flows were driven by minority heating (MH) [83][1]. Recent experiments on Alcator C-Mod have produced the first unambiguous demonstration of flow drive via mode converted slow waves in a tokamak plasma.

For the experiments described here, plasma flows were measured in discharges with both MH and MC ICRF. The minority heating scheme involved launching fast waves at 80 MHz from the low field side into bulk deuterium plasmas with a minority H concentration of $n_H/n_e \leq 5\%$. The magnetic field in both the MC and MH discharges

[1] In an ICRF MH scheme a small amount of a second ion species is introduced into the plasma. Fast waves directly heat this minority population via the cyclotron resonance[84]. These high energy minority ions then slow down on, and heat, both the electrons and bulk ions.

was 5.1 T which puts the ion cyclotron resonance at $R_{IC,H} \approx 0.65$ m, slightly inboard of the magnetic axis ($R_o \approx 0.67$ m). In the mode conversion heating scheme 50 MHz fast waves were launched from the low field side into $D-^3He$ plasmas. These fast waves then mode convertered in the vicinity of the $D-^3He$ hybrid layer ($R_{IC,^3He} \approx 0.71$ m) into short wavelength ICWs and IBWs.

8.1 Toroidal Rotation

Figure 8-1 compares two discharges with the same current, magnetic field and line averaged density, but different RF heating schemes (MH in blue and MC in red). Although the amount of RF power coupled to both plasmas is almost identical, the change in central toroidal rotation, ΔV, is considerably larger in the MC case. It should be noted, however, that the change in stored energy, ΔW, is larger in MH plasmas than in the MC plasmas. These results are displayed graphically in figure 8-2 in which the Rice scalings for multiple MH and MC plasmas are compared. The slope of the Rice scaling for the MC data is about 2 times larger than the slope of MH data because the MC plasmas tend to have larger ΔVs and smaller ΔWs than their MH counterparts. Taken together, these results suggest that MC is less efficient (in a per MW sense) than MH ICRF at heating, but more efficient at driving rotation.

It is also interesting to note that the two heating schemes divide their power differently between the ions and the electrons. This can be inferred by comparing the ion and electron temperatures for the two types of discharges. In figure 8-1 we see that the $T_e(0)$ for the MH discharge is considerably larger than $T_i(0)$, suggesting that more of the ICRF wave energy is being deposited into the electrons. In the MC discharge $T_e(0) \approx T_i(0)$ suggesting that the ICRF wave energy is being divided more towards the ions.

The MC driven toroidal flow is most pronounced in the core of the plasma ($r/a < 0.5$). This is illustrated in figure 8-3 in which profiles of V_ϕ and T_i are shown for the same discharges depicted in figure 8-1. Profiles are plotted for two times during the discharge; pre-ICRF(open symbols) and during ICRF(closed symbols). Comparing

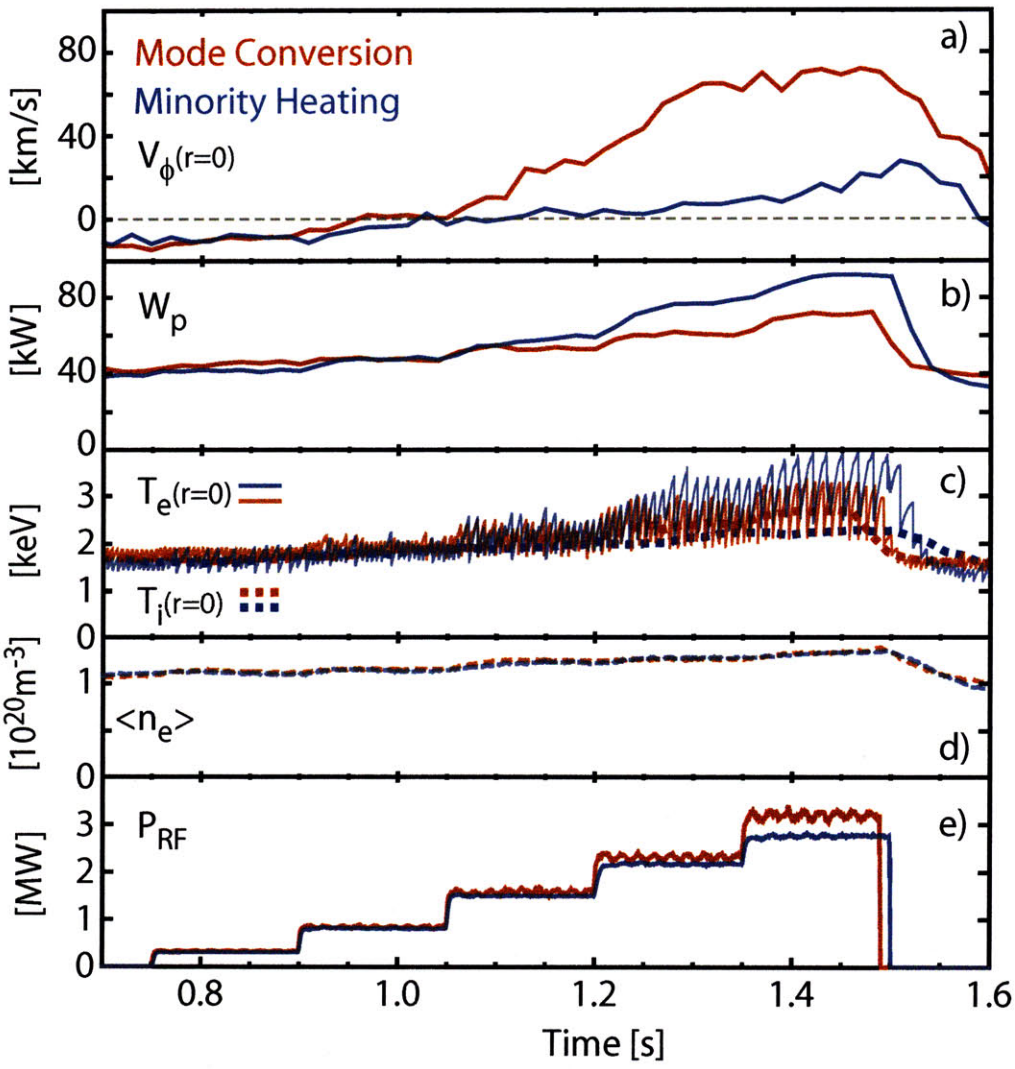

Figure 8-1: Comparison of similar discharges with different RF Heating schemes (MC in red, MH in blue). From top to bottom: a) central toroidal rotation, b) plasma stored energy, c) central electron temperature (solid lines) and central ion temperature (dashed lines), d) line averaged density, and e) RF power. Both discharges had I_p = 800 kA and B_T = 5.1 T.

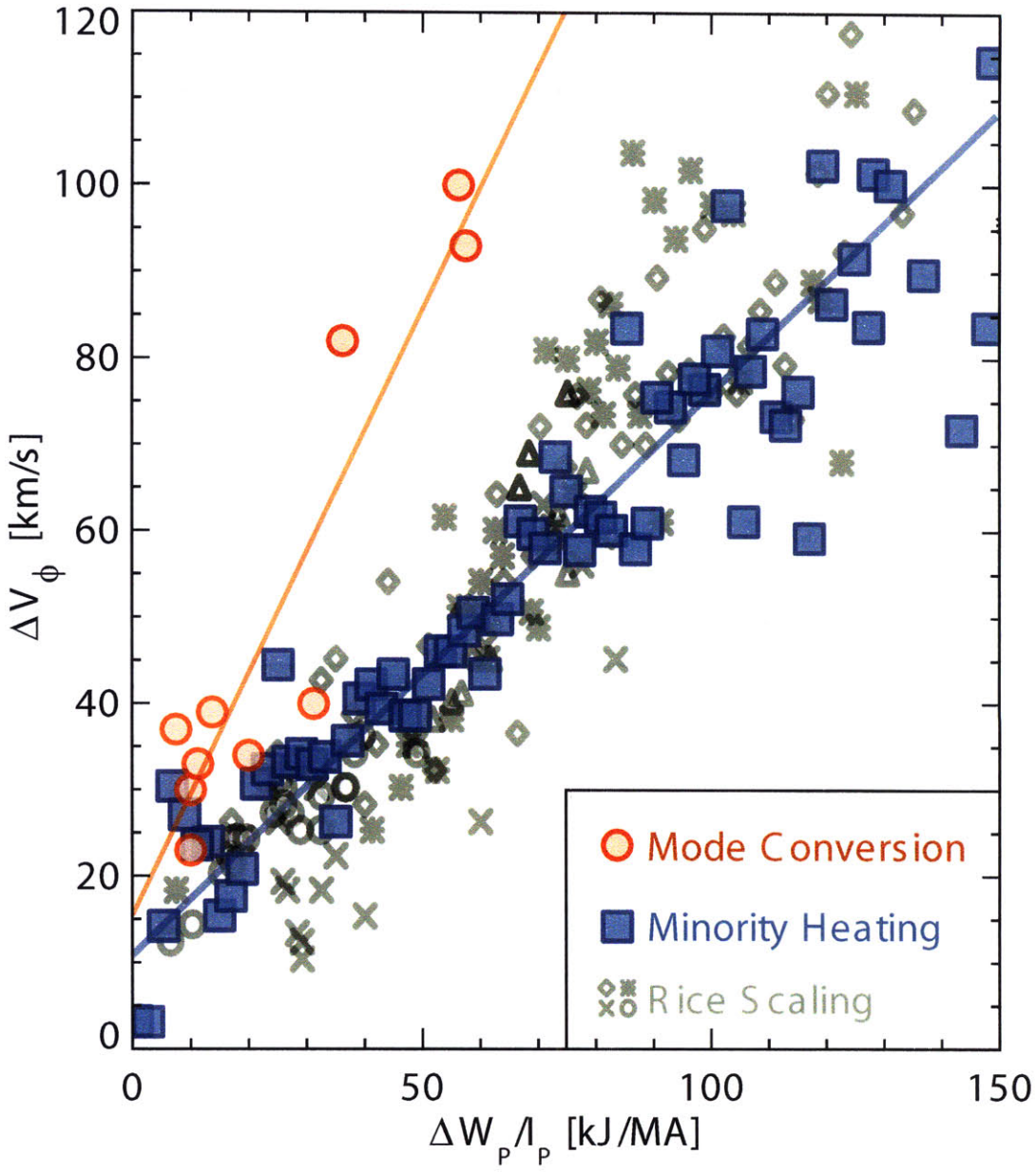

Figure 8-2: Comparison of the Rice scaling for discharges with MC (red circles) and MH (blue squares) ICRF. The data from the original Rice scaling (figure 6-2) has been over plotted in gray for comparison.

the pre-ICRF profiles, we see that the two discharges are well match (i.e. the rotation velocity of the two discharges are within error bars of one another, while the MC discharge has only a slightly higher ion temperature). Comparing the rotation profiles of the MH discharge before and during the ICRF phase we see that there is a ~30 km/s shift in the co-current direction, with the profile shape remaining relatively flat. In the MC discharge the central rotation increases by ~80 km/s and the profile shape changes from relatively flat to peaked on axis.

In general, the shape of a rotation profile in steady state results from a balance between torque density and momentum transport. Snapshots of rotation profiles, such as those in figure 8-3, can only provide information on the net result of these two effects. For example, the peaked rotation profile of the MC discharge could have been produced by an edge torque with a strong inward momentum pinch or simply a core localized effect. In order to distinguish between these two possibilities one must look at the temporal evolution of the rotation velocity profile. Figure 8-4 shows the time histories of toroidal rotation at three radial locations (r/a =0, 0.3, and 0.7) for the same MC discharge depicted in figure 8-3. The fact that the central channels experience an increase in toroidal rotation well before the outer channel indicates that the co-current spin up of the plasma resulted from a core localized effect and not from momentum propagating in from the edge.

8.2 Poloidal Rotation and Radial Electric Field

In addition to toroidal rotation, MC ICRF has also been observed to drive poloidal flows. Figure 8-5 shows ICRF induced poloidal rotation profiles as a function of source power for both MC and MH plasmas. For the MC discharges the poloidal rotation is in the ion diamagnetic direction, scales approximately linearly with RF power, and peaks at $r/a \approx 0.45$. In the MH cases the induced poloidal rotation is within error bars of zero for all ICRF power levels indicating no significant poloidal rotation drive. Figure 8-6 shows the total radial electric field in MC and MH plasmas. The three terms in radial pressure balance that sum to give the radial electric field are also

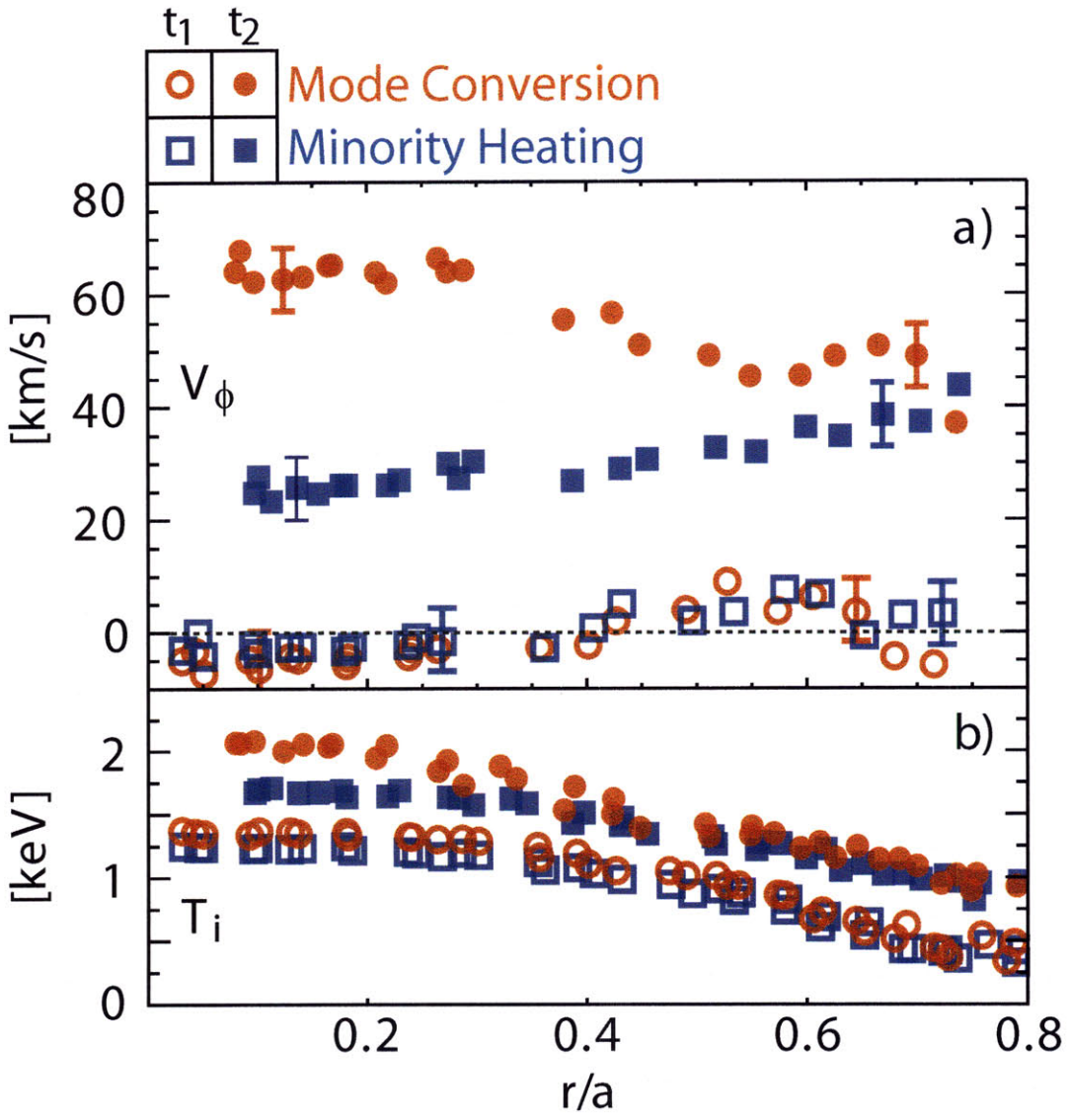

Figure 8-3: Comparison of toroidal rotation a) and ion temperature profiles b) between discharges with MC (red) and MH (blue) ICRF. Open symbols represent profiles before the application of ICRF ($t_1 = 0.7$ s in figure 8-1) while closed symbols represent profiles toward the end of the ICRF pulses ($t_2 = 1.4$ s).

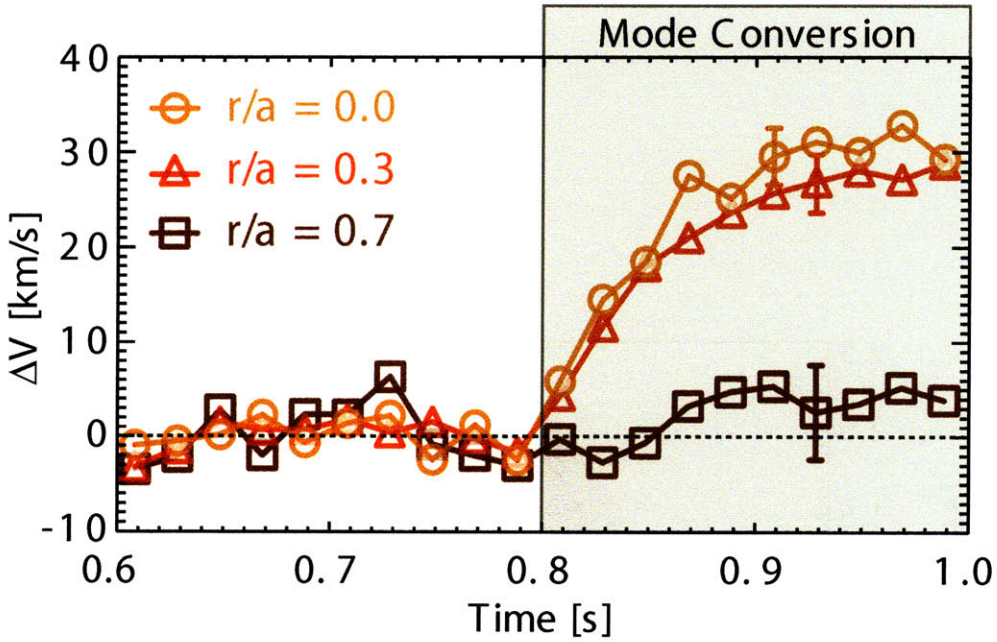

Figure 8-4: Temporal evolution of the toroidal rotation in a discharge with MC ICRF.

shown. It is clear from this figure that the radial electric field is substantially larger in the MC case. The diamagnetic term is similar in shape and magnitude for the two discharges, and so the difference in radial electric field profiles is almost entirely from the difference in $\vec{V} \times \vec{B}$.

These poloidal rotation profiles represent the flow of highly ionized argon impurities and not the bulk ions. In this particular case the ICRF flow drive of the impurities is indirect since it is the resonant ions that are absorbing the mode converted waves. As such, the impurity flows result from a combination of

1. Changes in frictional forces with the ions

2. Changes to the radial electric field profile

It is important to keep in mind that trace impurities do not significantly influence ion flow or the radial electric field (they simply respond to them). The toroidal flow of a trace impurity is closely tied to that of the main ions via strong parallel friction

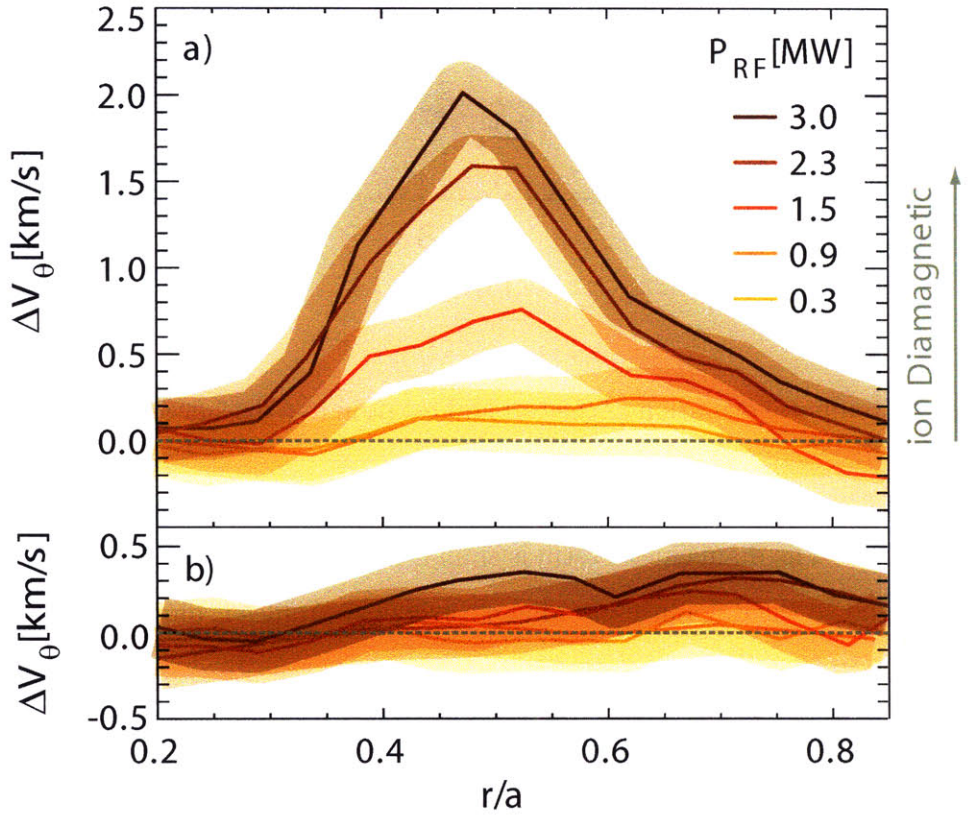

Figure 8-5: Comparison of poloidal rotation profiles in discharges with a) MC and b) MH ICRF at various power levels. Shaded error bars are based on statistical uncertainty.

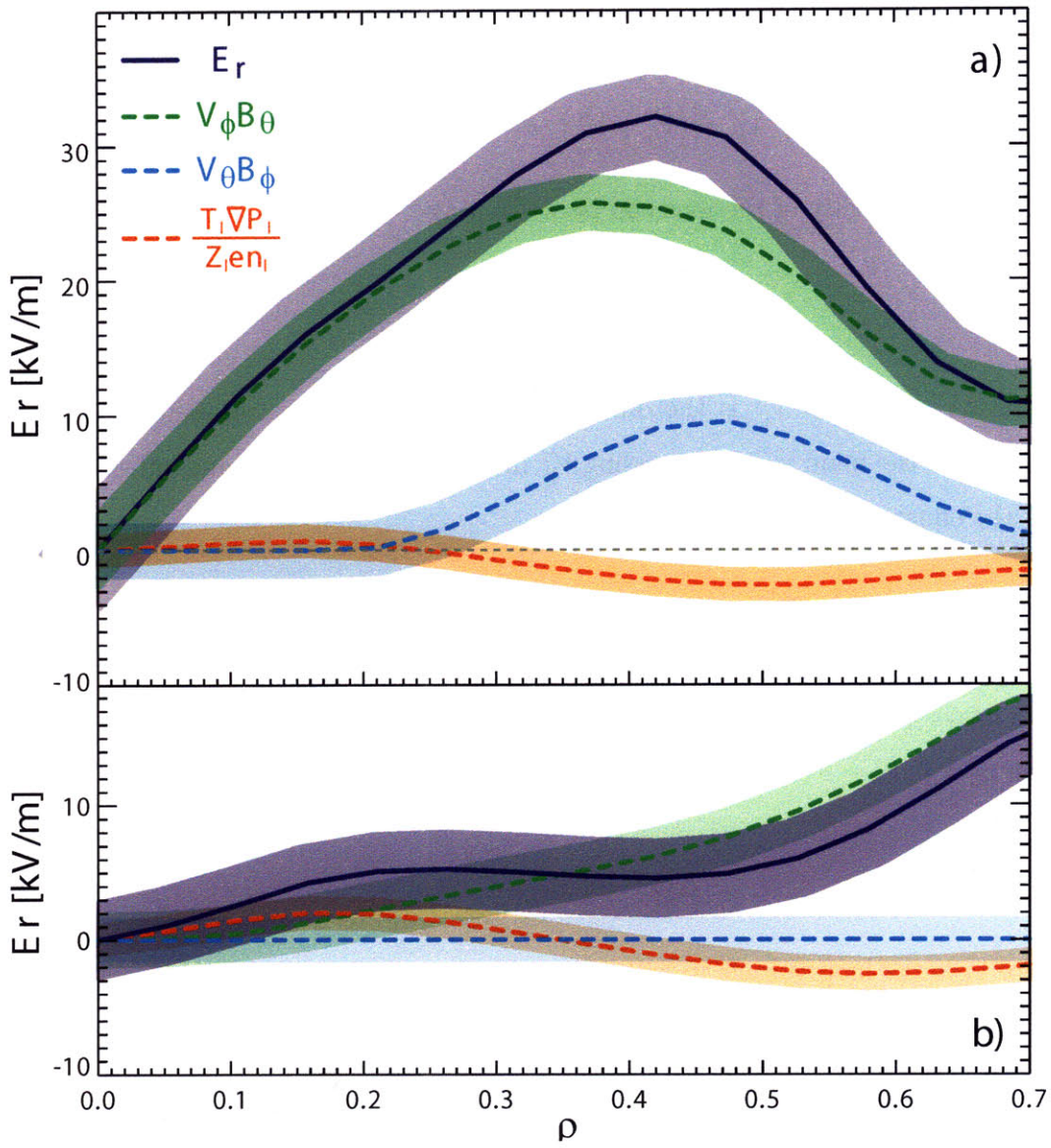

Figure 8-6: Profiles of the radial electric field in a discharge with a) MC , and b) MH ICRF. The total radial electric field is shown in solid blue while the velocity and diamagnetic terms are shown in dashed lines.

forces[25]. The poloidal velocities of impurities and ions, however, are less closely coupled because the poloidal damping associated with magnetic pumping can differ between species[25][85]. The poloidal rotation of the main ions can be estimated by relating the poloidal velocity to the parallel and perpendicular velocities:

$$V_\theta^i = \left(\vec{V}_{||}^i + \vec{V}_\perp^i\right) \cdot \hat{\theta} = \frac{B_\theta}{B} V_{||}^i + \frac{B_\phi}{B} V_\perp^i \tag{8.1}$$

The parallel velocity of the ions can be written as

$$V_{||}^i = \Delta V_{||}^{i,I} + V_{||}^I \tag{8.2}$$

where $\Delta V_{||}^{i,I} \equiv V_{||}^i - V_{||}^I$ is the difference in parallel velocity between an impurity species and the main ions. Expressing $V_{||}^I$ in terms of V_θ^I and V_ϕ^I and substituting it into the equation above gives

$$V_{||}^i = \Delta V_{||}^{i,I} + \frac{B_\theta}{B} V_\theta^I + \frac{B_\phi}{B} V_\phi^I \tag{8.3}$$

For a heavy trace impurity in a bulk deuterium plasma $\Delta V_{||}^{i,I}$ on axis is approximately given by [2]

$$\Delta V_{||}^{i,I} = 3.0 \frac{V_\ell}{R} \frac{T_i^{3/2}}{n_{20}} (km/s) \tag{8.4}$$

where V_ℓ is the loop voltage in volts, T_i is the ion temperature in keV, n_{20} is the ion density in $10^{20} m^{-3}$ and R is the major radius in meters. For all the MC discharges this expression gives $\Delta V_{||}^{i,I}$ ~5 km/s. From radial pressure balance the perpendicular ion velocity can be written as

$$V_\perp^i = \frac{1}{B}\left(E_r - \frac{T_i}{e} L_{p,i}^{-1}\right) \tag{8.5}$$

where $L_{p,i}^{-1}$ is the inverse gradient scale length of the ion pressure. Substitution of E_r from the impurity radial pressure balance equation gives

[2]For details see appendix E

$$V_{\perp}^{i} = \frac{1}{B}\left(V_{\theta}^{I}B_{\phi} - V_{\phi}^{I}B_{\theta} + \frac{T_I}{Z_I e}L_{p,i}^{-1} - \frac{T_i}{e}L_{p,i}^{-1}\right) \tag{8.6}$$

We can now substitute the expressions for $V_{||}^{i}$ (equation 8.3) and $V_{\perp}^{i}$ (equation 8.6) into the expression for V_{θ}^{i} (equation 1). Some routine algebra then gives,

$$V_{\theta}^{i} = V_{\theta}^{I} + 3.0\frac{V_{\ell}}{R}\left(\frac{B_{\theta}}{B}\right)\left(\frac{T_i^{3/2}}{n_{20}}\right) + \frac{B_{\phi}}{B^2}\left[\frac{T_I}{Z_I e}L_{p,I}^{-1} - \frac{T_i}{e}L_{p,i}^{-1}\right] \tag{8.7}$$

The first term is simply the impurity poloidal velocity which was measured to be $\sim$ 2km/s at $\rho \approx 0.4$. The second term is the poloidal projection of the difference in parallel flow. Substituting $V_{\ell} = 0.65$ V, $R = 0.67$ m, $B_{\theta} = 0.55$ T, B = 5.4 T, $T_i =$ 1.8 keV and $n_2 0 = 1.4$ gives $\Delta V_{||} \cdot \hat{\theta} \approx$0.5 km/s.

The third term is simply the poloidal projection of the difference between the ion and impurity diamagnetic velocities. For $\rho \sim 0.4$ in the MC plasmas $L_{p,i}^{-1}$ is comparable to $L_{p,I}^{-1}$. Therefore the impurity diamagnetic term is smaller than the ion diamagnetic term by about factor of Z_I. Since the ion pressure gradient is < 0, it then follows that the diamagnetic velocity term will always be positive (i.e. in the ion diamagnetic direction, hence the name). With $L_{p,i}^{-1} \sim 10\ m^{-1}$, the third term has a value of $\sim$3 km/s. Taken together these estimates suggest that the ion poloidal rotation velocity in this case is $\sim$5.5 km/s in the ion diamagnetic direction.

8.3 Comparison with Theory

In their 2002 paper J.R. Myra et al. derived approximate expressions for both poloidal and toroidal flows driven by IBW absorption[81]. The expression for the poloidal rotation was derived in the "Diffusion limit" in which $\Delta << \lambda << r_a$, where r_a is the minor radius, λ is the width of the poloidal flow layer and Δ is the absorption layer thickness. For the MC Alcator C-Mod plasmas, we have $\Delta \approx 1$ cm, $\lambda \approx 2$ cm and $r_a \approx 10$ cm, and therefore the second condition is somewhat satisfied while the first is marginal. In the derivation, the condition $\Delta << \lambda$ is manifested as the assumption that the RF force is a delta function in minor radius. Given the nature

of this derivation, having $\Delta \sim \lambda$ simply has the effect of broadening the poloidal flow profile while reducing its height. As a result, the predicted poloidal rotation for the specific Alcator C-Mod case being considered here will be somewhat over estimated. Bearing these caveats in mind, the expressions for the toroidal and poloidal flows (equations 43 and 45 in reference [81]) are:

$$V_{\phi}^{IBW} \approx 48 \frac{P_{IBW} k_{||}}{RfDn_{20}\mu} \tag{8.8}$$

$$V_{\theta}^{IBW} \approx 0.4 \frac{P_{IBW}}{q^2 R r_a B D n_{20}} \tag{8.9}$$

where $V_{\phi,\theta}^{IBW}$ are the toroidal and poloidal rotations induced by the absorption of IBWs, P_{IBW} is the rate of IBW energy absorption, $k_{||}$ is the parallel wave number, R is the major radius, r_a is the minor radius of the resonance layer, f is the wave frequency, D is the momentum diffusivity, n_{20} is the electron density in $10^{20} m^{-3}$, $q(r)$ is the local safety factor and μ is the ratio of the average ion mass to a proton mass, defined as[3]

$$\mu \equiv \frac{\sum n_i m_i}{\sum n_i m_p} \tag{8.10}$$

The units and values of the parameters in equations 8.8 and 8.9 for the MC ICRF plasma in figure 8-1 are given in table 8.1. Most of these values (i.e. f, B, R, r_a, $q(r)$, n_{20} and μ) were measured, while the remaining three (D, $k_{||}$ and P_{IBW}) require estimates. The momentum diffusivity, D, was estimated to be 0.2 m^2/s since this is a typical value for L-mode discharges in Alcator C-Mod[86]. The estimate of $k_{||} \approx 40 m^{-1}$ is based on numerical solutions of the full electromagnetic wave dispersion relation which takes into account $k_{||}$ up-shift. The estimate of $P_{IBW} \approx \frac{1}{2} P_{RF}$ is consistent with both TORIC simulations and the observed increases in electron and ion temperatures.

Substituting the values from table 8.1 into equations 8.8 and 8.9 give estimates of $V_{\phi}^{MC} \approx 160 km/s$ and $V_{\theta}^{MC} \approx 3 km/s$ both of which are within a factor of approx-

[3]In reference [81] the definition of mu is incorrectly given as the inverse of equation 8.10.

Table 8.1: MC Plasma Parameters

Parameter	P_{IBW}	f	B	R	r_a	q(r)	n_{20}	$k_{\|\|}$	D	μ
Units	MW	MHz	T	m	m	-	$10^{20}m^{-3}$	m^{-1}	m^2/s	-
Value	$\sim \frac{1}{2}3.1$	50	5.1	0.7	0.1	~1.5	1.2	~40	~0.2	~2.1

imately two of the experimental values. In the derivation of equation 8.8 the plasma volume is taken to be $V = 2\pi^2 r^2 R$ which implicitly assumes a circular cross section (a similar assumption is made in the derivation of 8.9). Taking into account non-unity plasma elongation leads to a factor of κ appearing in the denominators of equations 8.8 and 8.9. For the plasma referenced in table 8.1 the elongation is 1.6 which reduces the predicted rotation values to $V_\phi^{MC} \approx 100km/s$ and $V_\theta^{MC} \approx 2km/s$. While these values are closer to the experimental measurements the factor of κ may have been omitted from the derivation because the resulting expressions were only intended as order of magnitude estimates. In this context, there is qualitative agreement between theory and experiment with or without the inclusion of κ.

8.4 Direct ICRF Momentum Input

It is tempting to think that the flows driven in MC ICRF plasmas are simply the result of direct momentum input from the RF antennas. While this direct wave momentum can contribute to the toroidal torque on a plasma it is certainly not the only mechanism involved. It is possible to get an upper estimate on the direct wave momentum input by considering a control volume enclosing the RF antenna and then calculating the rate of momentum transfer through its surface. For this calculation it is convenient to think of the RF waves launched from the antenna as a flux of photons. The energy and momentum of each photon is simply $E = \hbar\omega$ and $p = \hbar k$ respectively. The ratio of the E/p for each photon is then $E/p = \omega/k = c$. If an antenna is launching P_{RF} watts worth of photons it follows that the rate of momentum

transfer from the antenna is simply $\frac{1}{c}P_{RF}$ in Newtons[4].

To estimate the importance of direct wave momentum input we can calculate how quickly a plasma is accelerated when subject to the $\frac{1}{c}P_{RF}$ force. To get an upper estimate we will make the following simplifying assumptions

1. There is no viscous damping
2. There is 100% wave absorbtion
3. All waves are launched in the same direction (i.e. ignoring secondary lobe emission)
4. The momentum of all photons is directed entirely in the toroidal direction

Making these assumptions, applying Newton's second law and rearranging gives

$$\Delta V = \frac{P_{RF}\Delta t}{cM} \tag{8.11}$$

where M is the mass of the plasma and ΔV is the change in velocity after Δt seconds of constant acceleration. Substituting $M \approx 2\pi^2\kappa r^2 R m_D \bar{n}_e$, where $\bar{n}_e$ is the average electron density and m_D is the mass of deuterium gives

$$\Delta V = \frac{P_{RF}\Delta t}{2\pi^2 c m_D \kappa r^2 R \bar{n}_e} = 0.5\frac{P_{RF}\Delta t}{\kappa n_{20} r^2 R} \tag{8.12}$$

where P_{RF} is in MW, Δt is in seconds and ΔV is in km/s. Figure 8-7 shows the time history of the central toroidal rotation for a MC ICRF discharge in which 3.4 MW of RF power (1.7 MW at both 50 MHz and 80MHz) is turned on at t = 0.6s. The central toroidal rotation changes by $\Delta V \approx 70$ km/s in a time $\Delta t \approx 120$ ms. For this discharge, $\kappa = 1.6$, r = 0.2, R = 0.67 and $n_{20} = 1.2$. Evening assuming all 3.4 MW of RF power goes entirely into co-current toroidal rotation, equation 8.12 predicts a ΔV of only ~4 km/s which is considerably less than the experimentally measured value. This example clearly illustrates that the large rotation velocities observed in

[4]The expression $\frac{1}{c}P_{RF}$ for the momentum input of the waves is consistent with numerical calculations of the integral of the Poynting vector over the antenna grill

MC ICRF plasmas are not simply the result of direct photon momentum input from RF antennas.

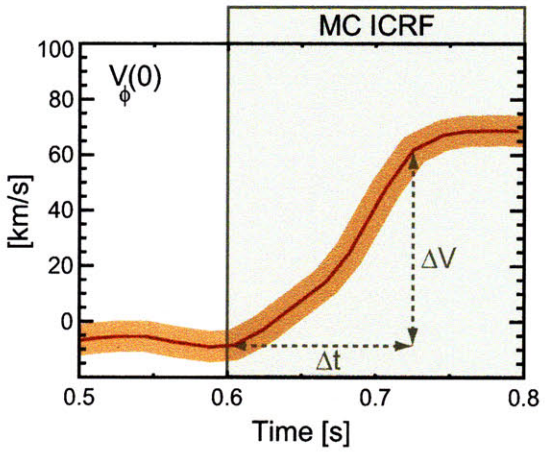

Figure 8-7: Central toroidal rotation vs. time for an MC ICRF discharge. The rapid acceleration of the plasma is too fast to be explained by photon momentum input from the RF antennas.

8.5 Chapter Summary

It has been demonstrated that the absorption of mode converted ICRF slow waves can drive substantial rotation in a tokamak plasma. The resulting co-current toroidal rotation profiles tended to be peaked on axis, with $\Delta V_\phi(0)$ up to 100km/s being measured. Compared to MH ICRF at the same power level, the MC waves were more efficient at driving rotation, but less efficient at heating. The MC driven poloidal rotation velocity was of order a few km/s in the ion diamagnetic direction and concentrated in the radial range $0.2 < r/a < 0.6$, peaking around $r/a \approx 0.45$. The experimentally measured plasma flows are in qualitative agreement with theoretical predictions based on the absorption of IBWs.

Looking forward to next generation tokamaks such as ITER, it is possible implement mode conversion ICRF schemes in D-T plasmas. Through careful choice of species mix, magnetic field strength, RF frequency, etc. it may be possible to drive significant amounts of poloidal and toroidal rotation in such plasmas.

THIS PAGE INTENTIONALLY LEFT BLANK

Chapter 9

Conclusions and Future Work

This thesis has described a novel imaging spectrometer capable of making detailed measurements of plasma rotation and has identified a number of mechanisms for driving flows without the need for neutral beam injection. This chapter will summarize the key results of these two themes and identify possible directions for future work.

9.1 Imaging X-ray Crystal Spectroscopy

A novel high resolution x-ray crystal spectrometer capable of making spatially resolved measurements has been designed, built, installed and operated on the Alcator C-Mod tokamak. By taking advantage of toroidal symmetry and magnetic flux surface mapping it is possible to perform spectral tomography with a single fan of views. This combination of spatial resolved spectra and tomographic techniques has allowed for measurement of a number of local plasma parameters from line integrated x-ray spectra for the first time. In particular these techniques have been used to measure temporally evolving profiles of emissivity, charge state densities, rotation velocity, electron temperature, ion temperature, as well as radial electric field.

Currently, the standard method for measuring rotation profiles in tokamak plasmas is active charge exchange spectroscopy with neutral beam injection. The perturbative nature of neutral beams with respect to plasma rotation makes it very difficult to study intrinsic flows with this technique. Moreover, next generation tokamaks like

ITER will operate at high densities and be considerably larger than present day experiments. Both of these effects will make neutral beam penetration (and therefore charge exchange spectroscopy) much more challenging. In contrast, high densities and increased plasma dimensions will make imaging x-ray crystal spectroscopy easier[1] rather than more difficult and the passive nature of this technique is ideally suited for intrinsic rotation studies.

The Hirex-Sr spectrometer has clearly demonstrated the feasibility of imaging x-ray crystal spectroscopy as a reliable diagnostic approach for fusion plasmas. The success of this project has influenced the decision to have a suite of such instruments on ITER and plans are underway to deploy similar spectrometers on other major tokamaks worldwide.

There are many ways in which the Hirex-Sr spectrometer and the associated set of data analysis routines can be up-graded. For example, developing an in-situ calibration source so that wavelength calibrations can be acquired without the need for locked mode discharges would be highly advantageous. Additionally, providing thermal stabilization of the spectrometer may help to reduce calibration drift. The use of toroidally, as opposed to spherically, bent crystals would decouple sagittal and meridional focusing. This decoupling would in turn allow spectral and spatial resolution to be optimized separately.

Potential up-grades aside, the Hirex-Sr spectrometer has recorded a large quantity of data since its installation in May of 2007 and only a small fraction of this data set has been studied in detail. The focus of this thesis has been on intrinsic rotation, but there are a number of other topics for which the Hirex-Sr spectrometer is well suited. For example, the ability to measure density profiles of multiple impurities (and multiple charge states) simultaneously and on short time scales (< 10 ms) constitutes a tremendous opportunity for impurity transport studies. The installation of an impurity injector on Alcator C-Mode for the next run campaign makes such studies even more promising. There is also an opportunity for fruitful collaborations with

[1]Increasing the density and size of a plasmas both increase the amount of line radiation it emits and therefore increases signal levels for x-ray spectroscopy.

atomic physics modelers who wish to validate their wavelength and rate coefficient calculations. Further atomic physics studies may also lead to alternative line ratio combinations for reliable T_e measurements at higher temperatures.

9.2 Intrinsic Rotation Studies

In past experiments the twin benefits of plasma rotation, namely turbulence suppression and resistive wall mode stabilization, have been provided by large amounts of tangential neutral beam injection. For reasons already alluded to in the previous section, neutral beam injection will be much less efficient at driving rotation in future reactors and so there is a need to identify alternative methods. The development of the Hirex-Sr spectrometer was motivated by a desire to measure plasma flows in the absence of neutral beam injection. In this thesis three methods of flow generating without the use of NBI have been identified: intrinsic rotation in enhanced confinement modes, lower hybrid wave induced rotation and ICRF mode conversion flow drive. A brief summary of the major findings for each of these methods is given below.

9.2.1 Intrinsic Rotation in Enhanced Confinement Modes

Tokamak plasmas in enhanced confinement modes have been observed to rotate in the co-current direction on every machine in which measurements have been made. In an effort to better characterize this phenomenon a multi-machine intrinsic rotation database was constructed. Statistical analysis of this database lead to the development of the following dimensionless and dimensional empirical scaling relations

$$\Delta V = 0.9 B_o^{1.1} \Delta \langle p \rangle^{1.0} I_p^{-1.9} R^{2.2} \tag{9.1}$$

$$M_A = 0.65 \beta_T^{1.4} q_*^{2.3} \tag{9.2}$$

This co-current rotation has the same phenomenology regardless of the type of auxiliary heating. This suggests that it is plasma gradients themselves, as opposed to the specifics of any given heating mechanism, that are giving rise to the observed rotation. The fact that these flows are observed to develop on time scales much shorter than those predicted by neoclassical theory is suggestive of a turbulence based driving mechanism. Given the complexity of the turbulence based rotation theories it is hugely surprising that simple scaling relations based on global plasma parameters do such a reasonable job unifying the observed data. Although empirical scaling relations are undoubtedly blunt instruments, even the most pessimistic extrapolations of the expression above suggest that there will be substantial intrinsic rotation in ITER H-modes.

9.2.2 Lower Hybrid Wave Induced Rotation

Lower hybrid waves have been shown to induce strong modifications to the toroidal rotation profiles in Alcator C-Mod plasmas. These modifications are in the counter-current direction, are core localized ($\rho < 0.5$) and have been observed in both L-mode and H-mode discharges. Changes in central rotation of up to 60 km/s have been observed in discharges with $\sim$1 MW of LH power. The modifications are well correlated with changes in normalized internal inductance, and their magnitude is inversely related to the $n_{||}$ of the launched LH waves. The negative increment in toroidal velocity observed in these discharges implies a negative charging of the plasma core and is consistent with a pinch of resonant trapped electrons.

These observations represent the first demonstration of the ability to create strongly sheared rotation and significant modification to the electric field profiles using lower hybrid waves. This phenomenon could prove to be helpful for advanced scenario development by providing a method for tailoring V_ϕ and E_r profiles.

9.2.3 ICRF Mode Conversion Flow Drive

Experiments on Alcator C-Mod have led to the first unambiguous measurement of flow drive via mode converted waves. For the same power level, mode converted waves drive significantly more toroidal rotation than minority heating ICRF. The resulting MC toroidal rotation profiles are peaked on axis, with rotation developing in the central portion of the plasma first. The toroidal acceleration of the plasma is much to rapid to be explained by the absorption of photon momentum alone.

Mode converted ICRF waves have also been shown to drive poloidal rotation. The resulting impurity poloidal rotation profiles are localized to the mid radius ($0.2 < \rho < 0.6$) with a peak velocity of $\sim$2 km/s in the ion diamagnetic direction. Strong coupling of parallel flows between ions and impurities suggests that the main ion poloidal rotation is in the same direction and somewhat larger than that of the impurities. The magnitude of both the poloidal and toroidal flows is consistent with theoretical estimates based on the absorption of ion Bernstein waves. Although it is not clear how these flow drive effects will scale to larger reactors, it should be possible to implement a MC heating scheme in D-T plasmas through judicious choice of RF frequency, species mix, and magnetic field strength.

9.3 Conclusions

Further study of the flow drive mechanisms identified here will no doubt lead to a greater understanding of the complicated subject of plasma rotation. It seems likely that these studies will also identify other methods for the modification of plasma flows. The broader message from this area of research in recent years has been that self-generated plasma flow is the rule as opposed to the exception. In hindsight, the fact that these flows went unnoticed for so long is the result of the misguided notion that plasma rotation is simply the result of neutral beam torque and diffusive momentum transport. With our greater understating of the subtleties of momentum transport and ever improving diagnostic capabilities there is justified hope that plasma rotation can be used to substantially improve the performance of tokamak plasmas.

THIS PAGE INTENTIONALLY LEFT BLANK

Appendix A

H- & He-Like Argon Spectra

The Hirex-Sr spectrometer was designed to measure line radiation from highly ionized charges states of argon, specifically the hydrogen and helium like charge states. The spectrometer covers the spectral range $3.94\mathring{A} < \lambda < 4.00\mathring{A}$ to measure the strongest of the He-like argon lines. For lack of a better name, this wavelength range will be referred to as "He-like" even though He-like argon emission lines are not the exclusive inhabitants of this spectral range. By the same token, the wavelength range $3.72 < \lambda < 3.80$ will be referred to as "H-like".

A.1 He-like Argon Spectra

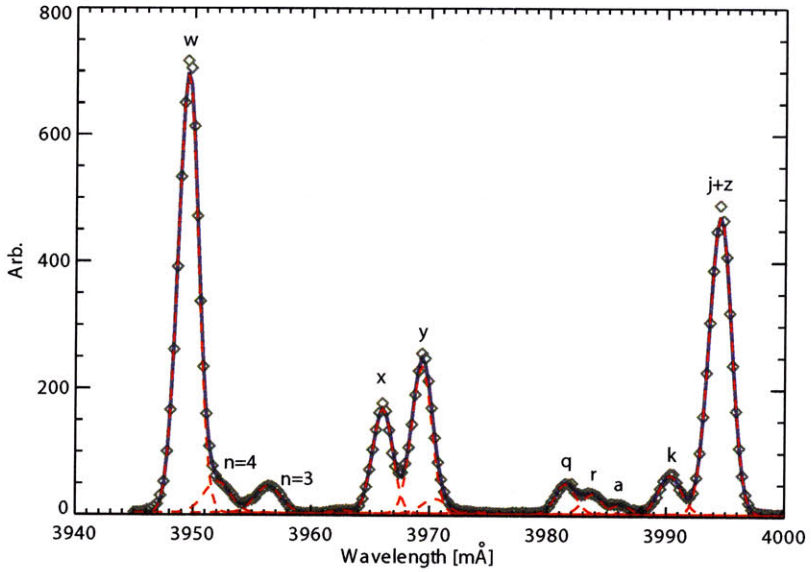

Figure A-1: The He-like argon spectrum as measured by the Hirex-Sr spectrometer.

Table A.1: Argon lines in the wavelength range $3.94\mathring{A} < \lambda < 4.00\mathring{A}$. Wavelength are from reference[95]

Name	Transition	Wavelength [Å]
w	$1s2p\ ^1P_1 \rightarrow 1s^2\ ^1S_0$	3.9492
x	$1s2p\ ^3P_2 \rightarrow 1s^2\ ^1S_0$	3.9659
y	$1s2p\ ^3P_1 \rightarrow 1s^2\ ^1S_0$	3.9692
q	$1s2s2p\ ^2P_{3/2} \rightarrow 1s^22s\ ^2S_{1/2}$	3.9815
r	$1s2s2p\ ^2P_{1/2} \rightarrow 1s^22s\ ^2S_{1/2}$	3.9839
a	$1s2p^2\ ^2P_{3/2} \rightarrow 1s^22p\ ^2P_{3/2}$	3.9864
k	$1s2p^2\ ^2D_{3/2} \rightarrow 1s^22p\ ^2P_{1/2}$	3.9903
j	$1s2p^2\ ^2D_{5/2} \rightarrow 1s^22p\ ^2P_{3/2}$	3.9932
z	$1s2s\ ^3S_0 \rightarrow 1s^2\ ^1S_0$	3.9943

A.2 H-like Argon Spectra

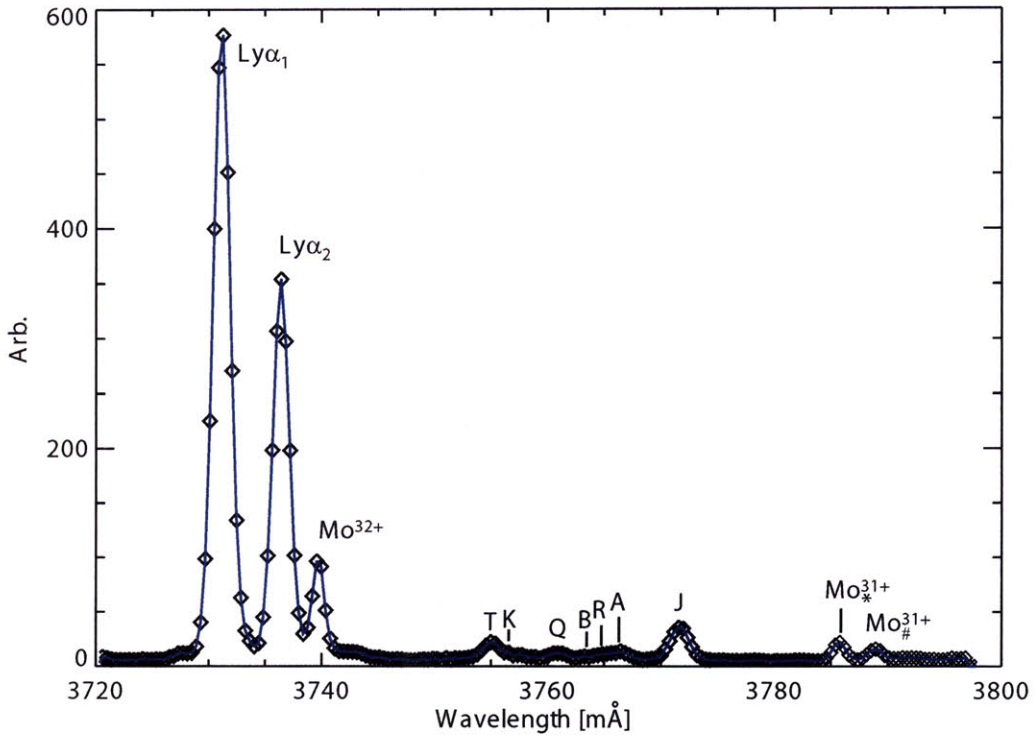

Figure A-2: The H-like Argon Spectrum as measured by the Hirex-Sr spectrometer.

Table A.2: Argon lines in the wavelength range $3.72 < \lambda < 3.80$. Wavelengths are from reference [98]

Name	**Transition**	**Wavelength**
Ly-α_1	$2p\ ^2P_{3/2} \rightarrow 1s\ ^1S_{1/2}$	3731.10
Ly-α_2	$2p\ ^2P_{1/2} \rightarrow 1s\ ^1S_{1/2}$	3736.52
T	$2s2p\ ^1P_1 \rightarrow 1s2s\ ^1S_0$	3755.26
Q	$2s2p\ ^3P_2 \rightarrow 1s2s\ ^3S_1$	3761.06
J	$2s2p^2\ ^1D_2 \rightarrow 1s2p\ ^1P_1$	3771.79

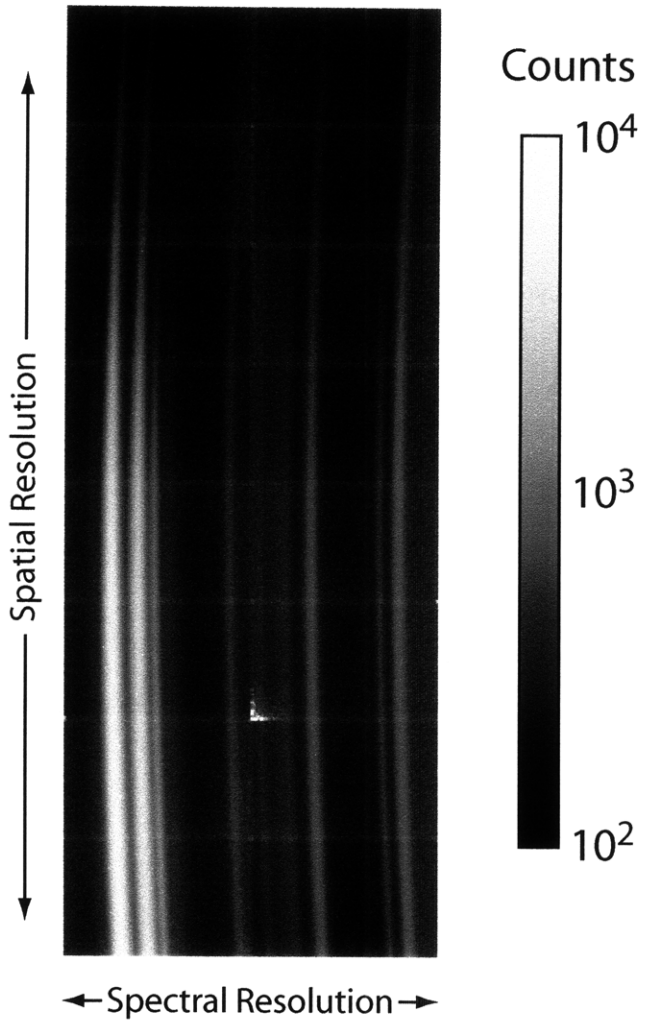

Figure A-3: Raw image from the H-like argon module.

Table A.3: Molybdenum lines in the wavelength range $3.72 < \lambda < 3.80$. Wavelengths are from reference [96]

Label	**Transition**	**Upper State**	**Wavelength**
$M32^{+}$	$2p - 4d$	$(2p-)^2(2p+)^4 4d - J = 1$	3739.8
$M31^{+}_{*}$	$2p - 4d$	$2p + [3s]\, 4d + J = \frac{3}{2}$	3785.7
$M31^{+}_{\#}$	$2p - 4d(3p)+$	$2p + [3p+]\, 4d + J = \frac{3}{2}+$	3787.4

Appendix B

X-ray Transmission Coefficients and Helium Purity Measurements

We wish to measure the attenuation coefficient of 3.1 keV X-rays in a gaseous mixture of predominantly He with a trace amount of air. The transmission coefficient, t, of x-rays passing through a gas can be written in the following form:

$$\tau \equiv \frac{I}{I_o} = \exp\left[-\alpha \frac{p}{T} x\right] \tag{B.1}$$

Where I_o is the intensity measured in a vacuum (i.e. with no gas present), I is the intensity measured in the presence of the gas, p is the pressure of the gas, T is the temperature, x is the path length through the gas and α is the attenuation coefficient

If the gas is composed of a mixture of gases then the total transmission coefficient is simply the product of the transmission coefficient of each component:

$$\tau_T = \prod_i \tau_i = \exp\left[-\sum_i -\alpha \frac{p_i}{T_i} x_i\right] \tag{B.2}$$

If all the components of the gas are in thermal equilibrium, and the path length is the same then x and T are constants and we get:

$$\tau_T = \prod_i \tau_i = \exp\left[-\frac{x}{T} \sum_i \alpha\ p_i\right] \tag{B.3}$$

For a gas composed of air and helium equation B.3 becomes:

$$\tau_T = \exp\left[-\frac{x}{T}(\alpha_{air}p_{air} + \alpha_{He}p_{He})\right] \tag{B.4}$$

Solving this equation for p_{air} we get:

$$p_{air} = -\frac{1}{\alpha_{air}}\left[\frac{T}{x}\ln\left(\frac{I}{I_o}\right) + \alpha_{He}p_{He}\right] \tag{B.5}$$

Since α_{He} and α_{air} are known values, and T, x and p_{He} are can be directly measured, we can estimate the partial pressure of air in a mixture by measuring the count rate of an x-ray detector, I, and comparing to the count rate of the same detector in a vacuum, I_o.

There is, however, one further complication. Although we are interested in x-rays of 3.1kev, there is no convenient source of x-rays at 3.1kev. Iron 55, Fe^55, is an acceptable substitute since its spectra is dominated by x-rays at 5.9 keV.

$$p_{air}^{calc} = -\frac{1}{\alpha_{air}^{Fe}}\left[\frac{T}{x}\ln\left(\frac{I^{Fe}}{I_o^{Fe}}\right) + \alpha_{He}^{Fe}p_{He}\right] \tag{B.6}$$

We can then substitute this value into the attenuation coefficient for the Argon line emission at 3.1kev.

$$\tau_T^{Ar} = \exp\left[-\frac{x}{T}(\alpha_{air}^{Ar}p_{air}^{calc} + \alpha_{He}^{Ar}p_{He})\right] \tag{B.7}$$

Where subscripts refer to the medium and superscripts refer to the photon energy (Ar the for 3.1 keV argon lines, and Fe for the 5.9 keV iron 55 source). Using equation B.7 the total transmission coefficient for 3.1kev photons traveling through 1.3 m of helium was calculated as a function of air (impurity). Figure B-1 shows that the transmission coefficient for pure He at standard temperature and pressure is about 97%. The transmission coefficient drops to about 90% at an air impurity fraction of 0.3%.

During part of the 2007 campaign, x-ray attenuations measurements were made using a scheme similar to that described above. An Fe^{55} source was placed inside the

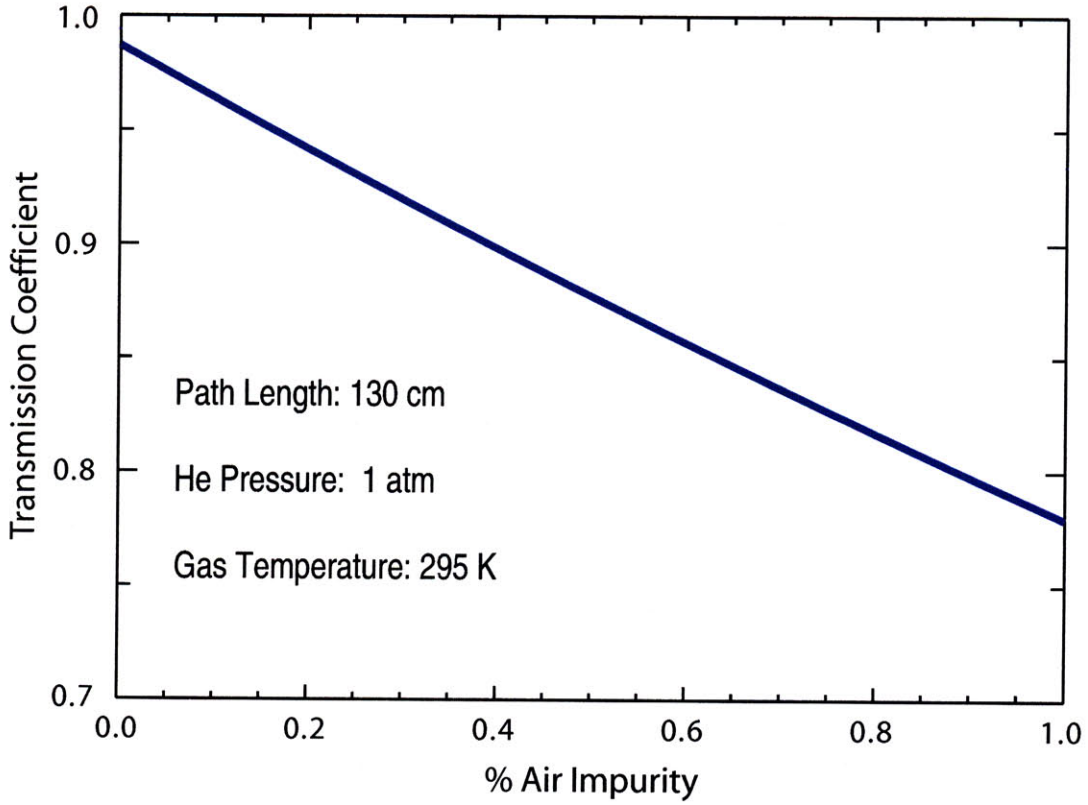

Figure B-1: Transmission coefficient of 3.1 keV x-rays as a function of % air impurity for a path length of 130cm at STP.

spectrometer housing and aimed at the Pilatus 100k x-ray detectors. The distance between the source and detectors was chosen such that the count rate per pixel was very small ($<<$ 1/second) but the total count rate for an entire module was large ($>$ 1000/second). This adds a negligible amount of background noise but allows for measurement of the Helium purity and x-ray transmission coefficient. The detectors were set up to trigger 100ms before the beginning of each discharge to allow for a measurement of the Fe55 source in the absence of plasma x-rays. IDL routines were written to automatically analyze the x-ray data at the end of each plasma discharge. This allowed for easy tracking of the helium purity and x-ray transmission throughout a run day without the need for a cell access. An example of the inferred helium purity and transmission coefficients over the course of a run day is shown in figure B-2.

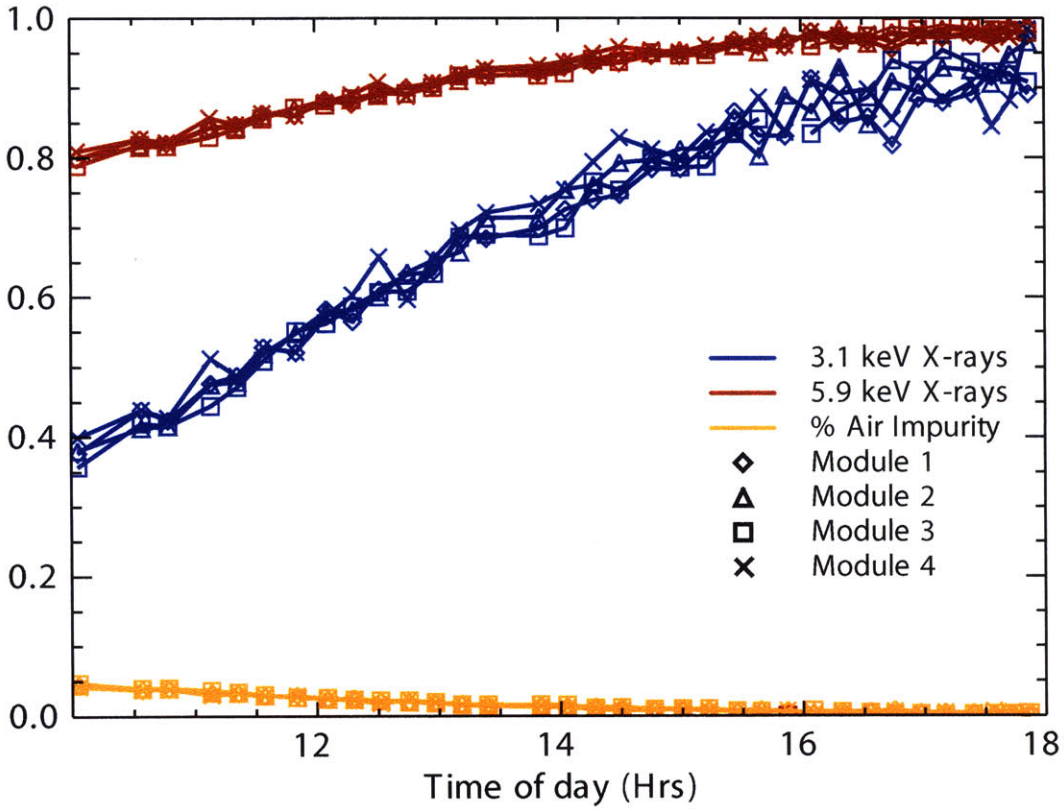

Figure B-2: The measured x-ray transmission coefficients of 5.9 keV x-rays were used to infer the % air impurity of the gas mixture in the spectrometer housing. This % air impurity was then used to calculate the transmission coefficient for 3.1 keV x-rays.

There is good agreement between the results based on data from all four detectors. This particular run day came after 3.5 days without operation during which time no helium was flowing through the spectrometer. At about 8:30 the helium flow was turned on. The steady flow of helium led to a gradual reduction in the air impurity levels throughout the day. As the amount of air in the spectrometer was reduced there was an associated increase in the x-ray transmission coefficients. The sensitivity of 3.1 keV X-rays to an air impurity is clearly visible, with the transmission coefficient doubling over the course of the day.

THIS PAGE INTENTIONALLY LEFT BLANK

Appendix C

Interspecies Thermal Equilibration

In general the temperature of each species in a plasma need not be the same. Temperature separation can occur when an one species is preferentially heated or cooled. Once a temperature difference develops, net energy is transfered from the hotter to the cooler species via Coulomb collisions. If the distribution functions of both species are Maxwellian then the time scale for thermal equilibration is given by

$$\tau_{eq}^{a,b} \approx \frac{3}{8\sqrt{2\pi}} \left(\frac{4\pi\epsilon_o}{Z_a^2 Z_b^2} \right)^2 \frac{m_b}{\sqrt{m_a}} \frac{(T_a/e)^{3/2}}{n_a} \frac{1}{ln\Lambda} \tag{C.1}$$

where T is temperature, n is density, m is atomic mass, Z is atomic charge charge, Λ is the Coulomb logarithm, the subscript a and b refer to the two species in question, and ϵ_o is the permittivity of free space[99]. It should be noted that the equation above assumes that $m_a << m_b$. The extent to which two species equilibrate their temperatures depends on the ratio of τ_{eq} to the energy confinement time, τ_E, which has the following definition,

$$\tau_E = \frac{W}{P_{in} - \dot{W}} \tag{C.2}$$

where W is the total thermal energy content of the plasma, $\dot{W}$ is the time rate of change of W and P_{in} is the total input power. If the equilibration time is slow compared to the energy confinement time then most of the energy deposited into the hotter species will be lost before it can be transmitted to the cooler species.

Conversely, if the equilibration time is short compared to the energy confinement time then the two species will thermally equilibrate before the energy is radiated or transported away. Thus we can expect good temperature equilibration when

$$\frac{\tau_{eq}}{\tau_E} << 1 \tag{C.3}$$

C.1 Ion-Impurity Thermal Equilibration

The ion temperature measurements presented in this thesis are based on Doppler broadening of emission lines from partially ionized argon impurity atoms in bulk hydrogen plasmas. These measurements reflect the temperature of the emitting argon atoms, while it is the temperature of the bulk hydrogen ions which is of greater interest. In the temperature range for fusion plasmas high Z impurities and bulk hydrogen ions tend to be well thermally coupled. This can be seen by rewriting equation C.1 for a bulk deuterium plasma, and an high Z impurity ($Z >> 1$),

$$\tau_{eq}^{I,D} \approx 2 \times 10^{-4} \frac{T_k^{3/2}}{Z_I n_{20}} \tag{C.4}$$

where T_k is the temperature in keV and n_{20} is the density in $10^{20} m^{-3}$ (it has also been assumed that $m_I \approx Z_I m_D$). For a typical Alcator C-Mod plasma ($T \approx 2keV$, $n \approx 10^{20} m^{-3}$) this gives $\tau_{eq}^{I,D} \approx 40\mu s$ which is considerably shorter than typical energy confinement times ($\sim 20 - 40$ ms).

An estimate of the upper limit on $\tau_{eq}^{I,D}$ for argon in an Alcator C-Mod plasma can be obtained by substituting a high temperature ($T_k = 5keV$) and low density ($n_{20} = 0.5$) into equation C.4 giving $\tau_{eq}^{Ar,D} \approx 0.3ms$. Clearly then $\frac{\tau_{eq}^{Ar,D}}{\tau_E} << 1$ even for low density, high temperature discharges on Alcator C-Mod and therefore argon is indeed well equilibrated with the bulk ions.

Next generation devices like ITER and DEMO will be operating at high densities ($\sim 10^{20}\ m^{-3}$) and temperatures ($\sim$ 12 keV). These values give a $\tau_{eq}^{Ar,D}$ of approximately 0.5 ms which we certainly hope will be much shorter than the energy confinement time.

C.2 Electron Ion Thermal Equilibration

Rewriting equation C.1 for the case of electron-deuterium thermal equilibration gives,

$$\tau_{eq}^{e,D} \approx 10^{-2} \frac{T_k^{3/2}}{n_{20}} \tag{C.5}$$

Comparing this result with the expression for $\tau_{eq}^{Ar,D}$ derived in the previous section (equation C.4) we see that the thermal equilibration time between electrons and ions is much larger than the equilibration time between ions and impurities. Substituting in the same high temperature/low density values used in the previous section ($T = 5keV$, $n = 0.5m^{-3}$) gives $\tau_{eq}^{e,D} \approx 250ms$ which is considerably longer than the energy confinement times on Alcator C-Mod. Substituting low temperature/high densities values ($T = 2keV$, $n = 3m^{-3}$) gives $\tau_{eq}^{e,D} \approx 10ms$ which is somewhat shorter than typical energy confinement times. Clearly then, for the parameter ranges of Alcator C-mod the ions and electrons can be, but are not necessarily, well thermally coupled.

Figure C-1 shows the electron-deuterium thermal equilibration time, $\tau_{eq}^{e,D}$, and the energy confinement time, τ_E, as a function of time throughout a high density/low temperature discharge. Since the energy confinement time is many times greater than the equilibration time, we expect that the $T_e \approx T_i$ for this discharge. Figure C-2 shows measurements of both the electron and ion temperature profiles from a number of different diagnostics. As expected the ion and electron temperature measurements are in good agreement. The fact that these measurements agree adds confidence to temperature calibration of the x-ray spectrometer.

Figure C-3 shows electron and ion temperature profiles in a high temperature ($T_e(0) \sim$ 4keV), low density ($n_e(0) \sim 2 \times 10^{20}\ m^{-3}$) discharge in which there is substantial separation between T_e and T_i.

The time histories of the energy confinement time and the ion-electron thermal equilibration times for this discharge are plotted in figure C-4. At 0.6 s 3 MW of ICRF power was coupled to the plasma leading to an immediate transition into H-mode.

This transition led to an increase in the energy confinement time and a reduction in thermal equilibration time (due to the large increase in temperature). During

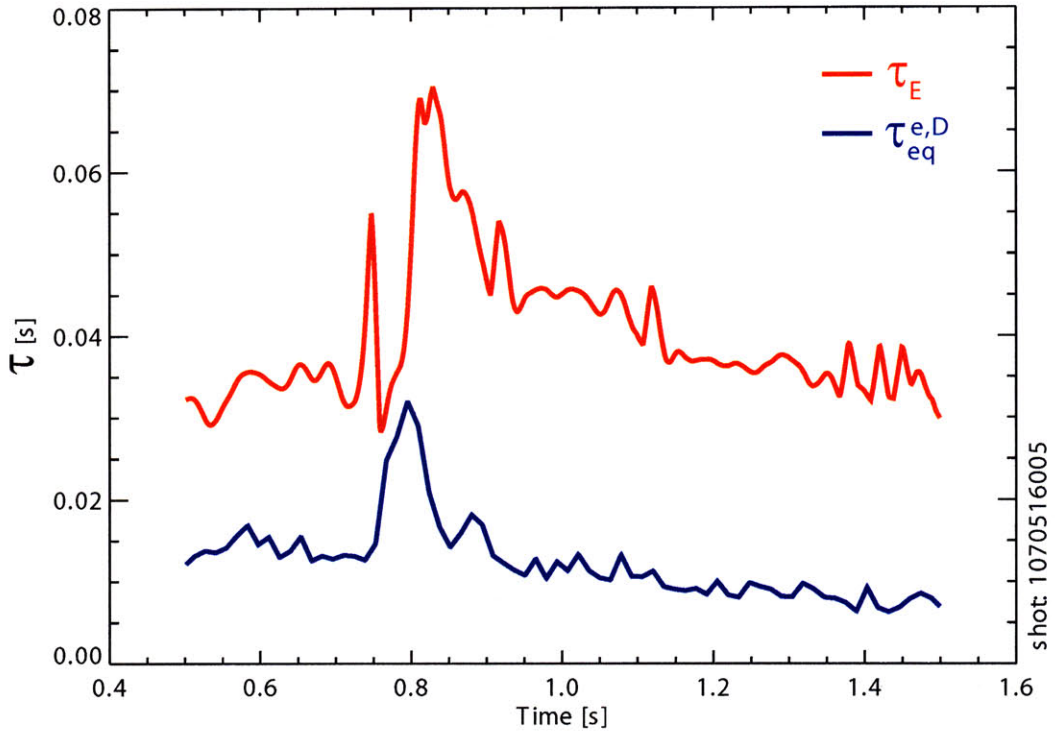

Figure C-1: Comparison of the energy confinement time and the electron-dueterium thermal equilibration time for a high density/low temperature discharge. Since the energy confinement time is long compared the equilibration time, the ions and electrons in this discharge are well thermally coupled.

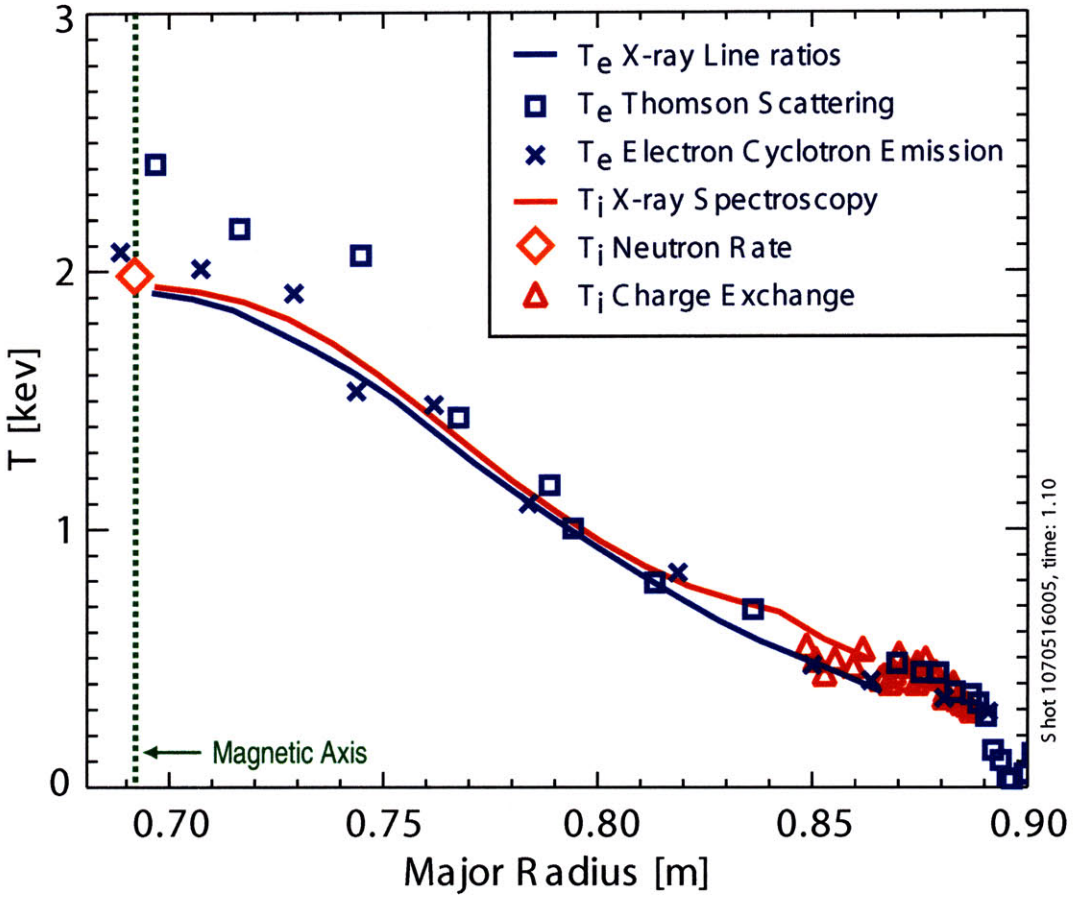

Figure C-2: Electron and ion temperature profiles in a high density/low temperature discharge (t = 1.1 s of figure C-1)

the H-mode phase the ratio of τ_{eq}/τ_E becomes less than unity making it possible for significant temperature separation to occur between the ions and electrons.

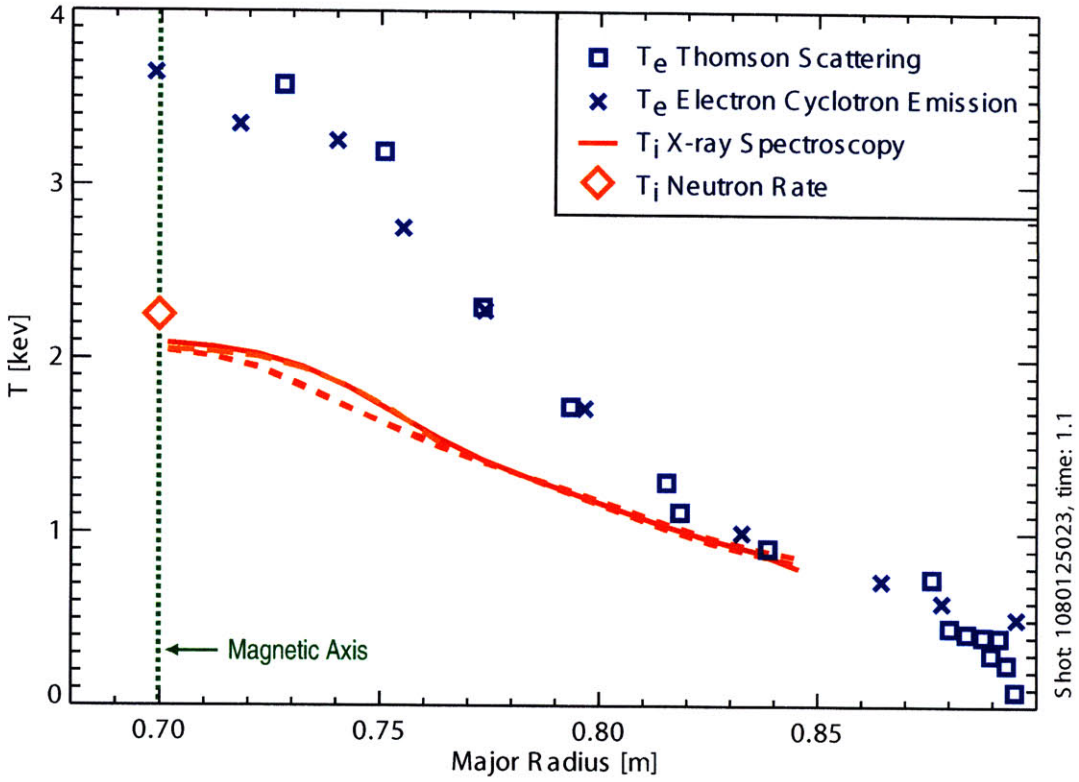

Figure C-3: Electron and ion temperature profiles in a high temperature (t = 1.1 s of figure C-4)

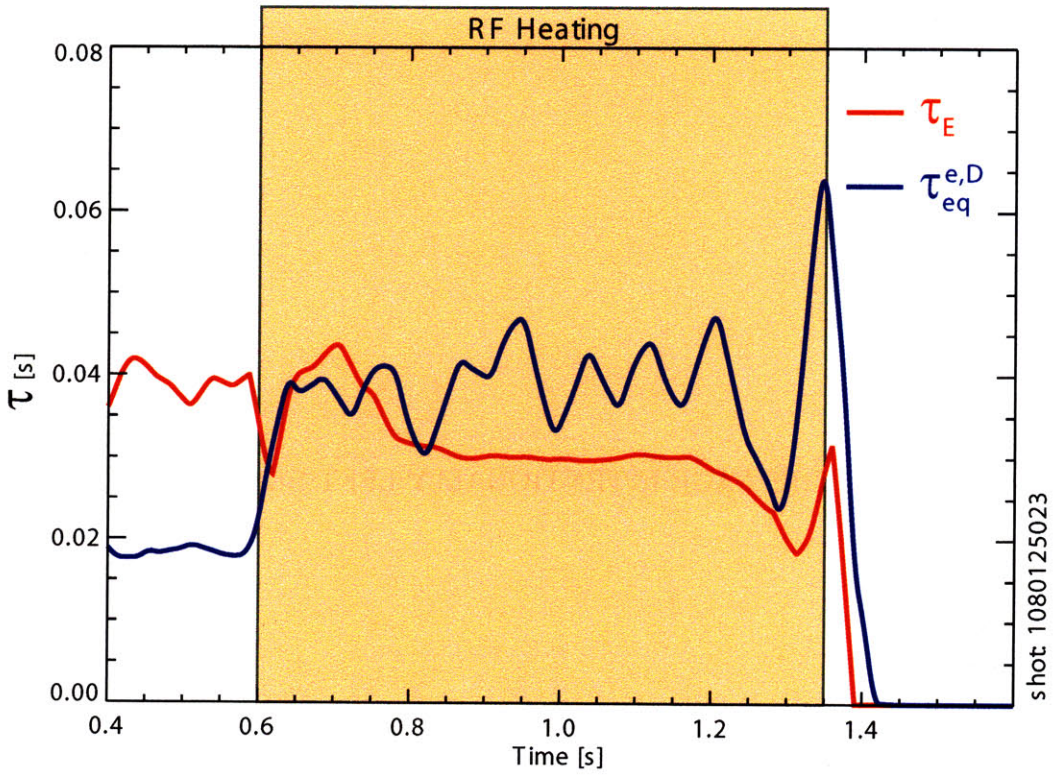

Figure C-4: Comparison of the energy confinement time and the electron-deuterium thermal equilibration time in a high temperature discharge.

THIS PAGE INTENTIONALLY LEFT BLANK

Appendix D

Resolving Power and Instrumental Temperature

The ability to infer plasma parameters from the subtle Doppler shifts and broadenings of x-ray line emission requires a high resolution spectrometer. The notion of "high resolution" is typically quantified in terms of the resolving power, $\lambda/\Delta\lambda$, where $\Delta\lambda$ is a measure of the smallest difference in wavelength that can be discerned by an instrument. One common way to determine $\Delta\lambda$ is to direct monochromatic light into the instrument in question and record the resulting spectra. The shape of this line is referred to as the instrument function, and $\Delta\lambda$ is usually taken to be its full width at half maximum (FWHM). In general the measured line shape will be the convolution of instrumental function and the actual line shape,

$$M(\lambda) = \int I(\lambda)L(\lambda - u)du \tag{D.1}$$

where $M(\lambda)$ is the measured line shape, $I(\lambda)$ is the instrumental function, and $L(\lambda)$ is the actual line shape. The convolution of the instrumental function with the line shape leads to an artificially broad measured line width. For the special case of a plasma with a Maxwellian impurity distribution and a Gaussian instrumental function it can be shown that the relationship between the measured, instrumental and actual widths is given by,

$$\Delta_M^2 = \Delta_I^2 + \Delta_L^2 \tag{D.2}$$

where Δ_M, Δ_I, Δ_L are the FWHMs of the measured line, instrumental function and the actual line shape respectively. For a purely Doppler broadened line, the relationship between temperature and line width is given by,

$$T = \frac{mc^2}{8 \ln 2} \left(\frac{\Delta\lambda}{\lambda_o} \right)^2 \tag{D.3}$$

where T, is the temperature, m is the mass of the emitting ion, c is the speed of light, λ_o is the rest wavelength of the emission line, and $\Delta\lambda$ is the FWHM of the line. Substituting this equation into D.2 and rearranging gives,

$$T^2 = T_M^2 - T_I^2 \tag{D.4}$$

where T is the actual plasma temperature, T_M is the temperature inferred based on the width of the measured line and T_I is the "instrumental temperature". The instrumental temperature can be interpreted as the temperature that one would infer from the measured width of a perfectly monochromatic source i.e.,

$$T_I = \frac{mc^2}{8 \ln 2} \left(\frac{\Delta\lambda_I}{\lambda_o} \right)^2 \tag{D.5}$$

where $\Delta\lambda_I$ is the FWHM of the instrumental function. It should be noted that the instrumental temperature depends on the mass of the emitting impurity.

There is no convenient calibration source for the wavelength regions of the H- and He-like argon spectra, so the plasma itself must be used. Determining the instrumental function and resolving power based on line radiation from a fusion plasma is non-trivial since the measured lines will necessarily be the convolution of the Doppler broadening and the instrument function. If the impurity temperature is not known *a priori* then it is not possible to distinguish the Doppler broadening from the instrumental broadening. This ambiguity can be resolved if two emission lines from impurities of significantly difference masses (but sharing the same temperature) can

be measured simultaneously. This can be seen by writing equation D.5 for each impurity and eliminating the plasma temperature:

$$ {}_aT_I^2 = {}_bT_I^2 + {}_aT_M^2 - {}_bT_M^2 \tag{D.6} $$

From equation D.5 the ratio of the instrumental temperatures is given by,

$$ \frac{{}_aT_I}{{}_bT_I} = \frac{m_a}{m_b} \tag{D.7} $$

Substitution of D.7 into D.6 and rearranging gives,

$$ {}_aT_I^2 = \frac{{}_aT_M^2 - {}_bT_M^2}{1 - \left(\frac{m_b}{m_a}\right)^2} \tag{D.8} $$

Since m_a and m_b are known quantities and ${}_aT_m$ and ${}_bT_m$ are both measured, one can calculate the instrumental temperature of both impurities. Fortunately the presence of a strong Ne-like molybdenum line very close to the H-like argon Lyman-α doublet allows for the calculation of the impurity temperatures. Figure D-1 shows a multi line fit to an example spectrum containing these lines.

The applicability of this method for determining the instrumental temperature is somewhat limited due to the requirement that the instrumental function be a Gaussian. For many instruments the rapid exponential decay of a Gaussian does not accurately model the instrumental function and this can lead to inaccuracies in inferred instrumental temperatures. An alternative approach involves using a Lorentizian instead of a Gaussian to model the instrument function. The Lorentizian function can be expressed as,

$$ I(\lambda) = \frac{1}{\pi} \frac{\frac{1}{2}\Delta}{(\lambda - \lambda_o)^2 + \left(\frac{1}{2}\Delta\right)^2} \tag{D.9} $$

where Δ is the FWHM and $I(\lambda)$ is normalized such that the integral of I over all λ is unity. The algebraically decaying wings provide a more realistic approximation to the instrument function of many instruments. The convolution of a Maxwellian velocity

distribution with a Lorentzian instrumental function gives rise to a measured Voigt line shape.

The crux of this alternative approach is to perform a multi-line Voigt fit to a spectrum containing lines from multiple impurities in which the Maxwellian widths of the lines are allowed to vary independently but the Lorentzian widths of all lines are taken to be the same. In addition to using a more appropriate model for the instrument function, this method also provides a convenient self consistency check. If the ratio of the Maxwellian widths for the two impurities differ significantly from the ratio of their masses, this suggests that there is a problem with the analysis. Conversely if ratio of the Maxwellian widths is close to the ratio of impurities, then the assumption of a Lorentzian instrument function is probably a reasonable one.

Figure D-1 shows the results of a multiple Voigt line fit to the H-like Argon spectra. The same Lorentzian width was used for each line, while the Maxwellian widths were allowed to vary independently. The fit shown gave a Lorentzian FWHM of 0.14 mÅ and Maxwellian widths of 0.782 mÅ and 0.525 mÅ for the argon and molybdenum lines respectively. The ratio of these widths is 0.67 while the expected value is $\sqrt{m_{Ar}/m_{Mo}} = 0.645$. This close agreement between the ratio of fitted Maxwellian widths and the square root of the impurity mass ratio suggests that a Lorentzian is a reasonable approximation for the instrumental function of the spectrometer. The inferred Lorentzian FWHM of 0.14 m$\mathring{A}$ implies a resolving power of $\lambda_o/\Delta\lambda \approx 25,000$.

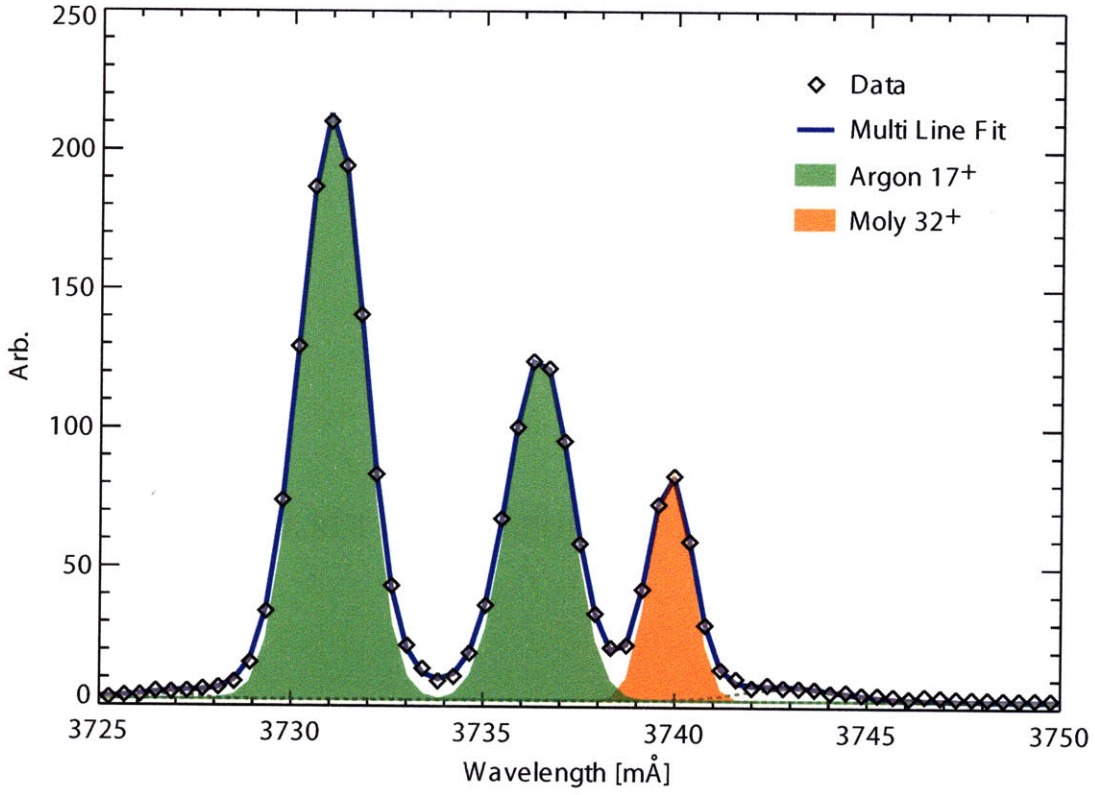

Figure D-1: Multi line fit of an H-like spectra using Voigt functions. The Maxwellian widths of the molybdenum and argon lines were allowed to vary independently, while a single Lorentzian width was used for all lines. Shaded regions indicate the width of each line associated with Doppler broadening.

THIS PAGE INTENTIONALLY LEFT BLANK

Appendix E

Ion-Impurity Parallel Flow Separation

The rotation velocities presented in this thesis are based on the Doppler shifts of impurity emissions lines. Although the flows of impurities are related to the flows of the main ions they are not identical. The poloidal flows of ion and impurities can in fact be quite different and can even have opposite signs[25]. The parallel velocities of ions and impurities, however, tend to be very well coupled due to parallel friction.

One effect that gives rise to separation in parallel velocities between ions and impurities is the parallel electric field. In the presence of a parallel electric field, the ions and electrons will drift in opposite directions. When a trace impurity is introduced into the plasma its flow will result from a balance between the electric field force and ion drag in the co-current direction and electron drag in the counter current direction. A detailed calculation of the difference in parallel flow between ions and impurities gives

$$\Delta V_{||}^{i,I} = -\frac{Z_i e E_{||}}{\nu_{ii} m_i} \frac{Z_I - Z_i}{Z_I} \frac{\sqrt{2} + 13\alpha/4}{(1+\alpha)(\sqrt{2}+\alpha} \tag{E.1}$$

where, Z_i and Z_I are the charge of the ions and impurities respectively, m_i is the ion mass, $E_{||}$ is the parallel electric field and $\alpha \equiv n_I Z_I^2 / n_i Z_i^2$[25]. For a heavy trace impurity in a bulk deuterium plasma equation E.1 simplifies to

$$\Delta V_{||}^{i,I} = 3.0 \frac{V_\ell}{R} \frac{T_i^{3/2}}{n_{20}} (km/s) \tag{E.2}$$

where T_i is the ion temperature in keV, n_{20} is the ion density in $10^{20} m^{-3}$, R is the major radius in meters and $V_\ell = 2\pi R E_{||}$ is the loop voltage in in volts. Figure E-1 shows time histories of V_ℓ, T_i, n_{20} and $\Delta V_{||}^{i,I}$ for Alcator C-Mod discharge. For this discharge (and the vast majority of Alcator C-Mod discharges[97]), $\Delta V_{||}^{i,I}$ is approximately 5 km/s. When interpreting impurity rotation data it is important to keep in mind that there can be slight differences between ion and impurity parallel flows.

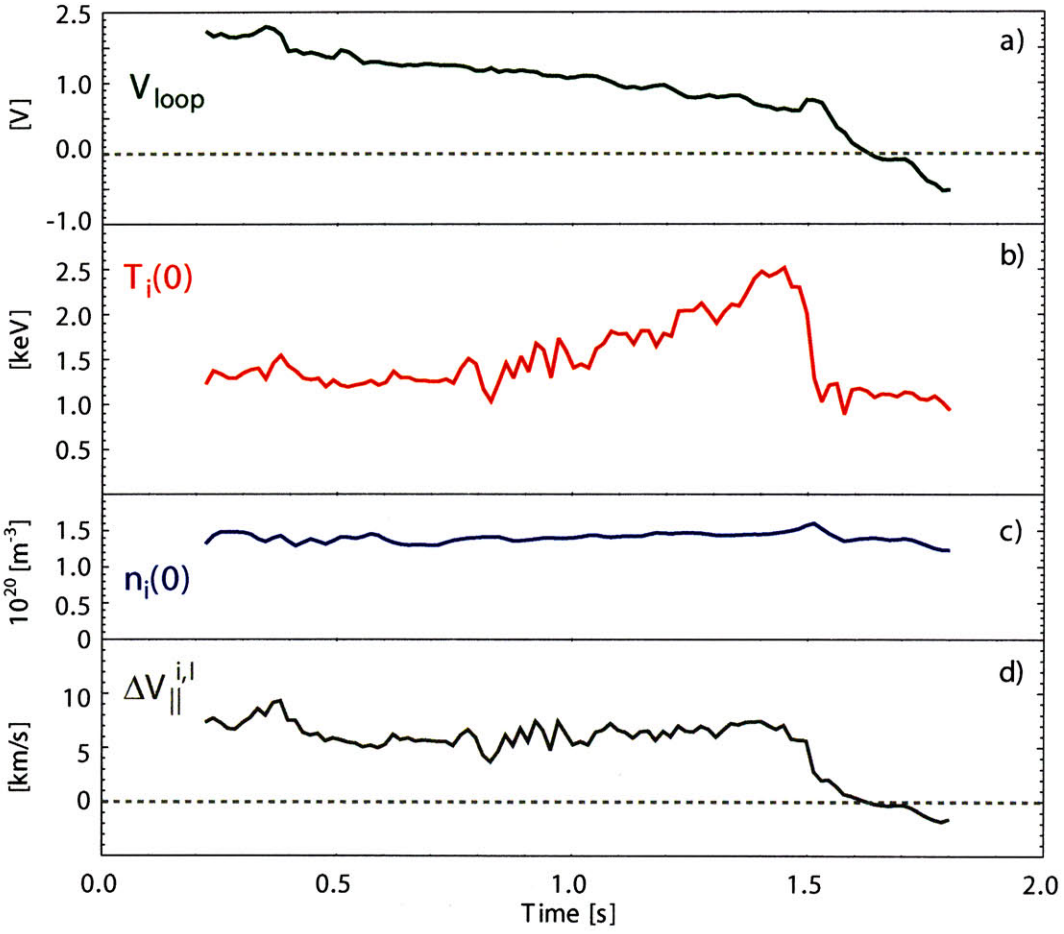

Figure E-1: Time histories of $\Delta V_{||}^{i,I}$ in a typical Alcator C-Mod discharge. The three quantities used to calculate $\Delta V_{||}^{i,I}$, namely loop voltage a), ion temperature b), and ion density c) are also are also plotted.

Appendix F

Intrinsic Rotation Scaling Variable Description

All units are in MKS unless otherwise specified

Table F.1: Plasma Quantities

Var.	**Units**	**Description**
V_ϕ	[km/s]	Toroidal rotation velocity
W	[MJ]	Plasma stored energy
I	[MA]	Plasma current
B_o	[T]	Toroidal field on axis
T_i	[keV]	Ion temperature
T_e	[keV]	Electron temperature
n_e	$[m^{-3}]$	Electron density
Z_I		Charge of dominant impurity species
Z_{eff}		$Z_{eff} = \frac{1}{n_e}\sum_j Z_j^2$

Table F.2: Geometric Quantities

a	[m]	Plasma minor radius
R	[m]	Plasma major radius
ϵ		Inverse aspect ratio: $\epsilon = a/R$
κ		Plasma elongation

Table F.3: MHD Variables

q_*		Edge safety factor: $q_* = \epsilon \frac{B_o}{B_\theta}$
β		$\beta = \frac{2\mu_o \langle p \rangle}{B_o^2}$
β_N	$[\%Tm/MA]$	Beta Normal: $\beta_N = \beta \frac{aB_o}{I}$
β_N'		Non-dimensional β_N: $\beta_N' = \beta_N/\mu_o = \frac{1}{2\pi\kappa} \frac{B_o}{B_\theta} \beta$

Table F.4: MHD Variables

ρ^*		Normalized gryo-radius: $\rho_* = \frac{r_L}{a} = \frac{1}{a} \frac{v_{th}}{\omega_I} = \frac{1}{aeB_o} \sqrt{m_i T_I}$
ν^*		Collisionality: $\nu^* \approx 2 \times 10^{-3} \left(\frac{q n_{20} Z_{eff} R}{\epsilon^{3/2} T_e^2} \right)$ with n_{20} in units of $[10^{20}]$

F.1 Derivation of m_{ave}

We begin with the definition for the average ion mass in a multi-species plasma:

$$m_{ave} \equiv \frac{\sum m_j n_j}{\sum n_j} \tag{F.1}$$

If we assume that the plasma consists of a bulk deuterium population and a single dominant impurity species of charge Z_I we obtain:

$$m_{ave} = \frac{m_D n_D + m_I n_I}{n_D + n_I} \tag{F.2}$$

We can then make the further assumption that the impurity is fully stripped and that $m_I \approx Z_I m_D$. The expression then becomes:

$$m_{ave} \approx m_D \left(\frac{n_D + Z_I n_I}{n_D + n_I} \right) \tag{F.3}$$

Assuming quasi-neutrality ($n_e \approx n_D + Z_I n_I$) we get:

$$m_{ave} \approx m_D \frac{n_e}{n_D + n_I} \tag{F.4}$$

After some routine algebraic manipulation it is possible to rewrite n_I and n_D in terms of Z_I and Z_{eff}:

Table F.5: Velocities

$V_{th,i}$	[km/s]	Ion thermal speed: $V_{th,i} = \sqrt{T_i/m_{ave}}$ where $m_{ave} \equiv (\sum m_j n_j) / (\sum n_j) \approx m_D \left[1 - (Z_{eff} - 1)/Z_I\right]^{-1}$
$V_{th,e}$	[km/s]	Electron thermal speed: $V_{th,e} = \sqrt{T_e/m_{ave}}$
C_A	[km/s]	Alfven speed: $C_A^2 = \frac{B_o^2}{\mu_o \rho} \approx \frac{B_o^2}{\mu_o n_e m_D}$
C_S	[km/s]	Ion Acoustic sound speed: $C_S^2 = (\sum \gamma_j p_j) / (\sum \rho_i) \approx \frac{T_i}{2m_D}\left[1 - \frac{Z_{eff}-1}{Z_I} + 3\frac{T_e}{T_i}\right]$

Table F.6: Mach Numbers

$M_{th,i}$		Ion thermal Mach #: $M_{th,i} = V_\phi / V_{th,i}$
$M_{th,e}$		Electron thermal Mach #: $M_{th,e} = V_\phi / V_{th,e}$
M_S		Ion acoustic Mach #: $M_S = V_\phi / C_S$
M_A		Ion thermal Mach #: $M_A = V_\phi / C_A$

$$n_I = n_e \frac{Z_{eff} - 1}{Z_I (Z_I - 1)} \tag{F.5}$$

$$n_D = n_e \left(1 - \frac{Z_{eff} - 1}{Z_I - 1}\right) \tag{F.6}$$

Plugging these expressions into equation F.4 gives the final result

$$m_{ave} \approx m_D \left(1 - \frac{Z_{eff} - 1}{Z_I}\right)^{-1} \tag{F.7}$$

F.2 Derivation of the Ion Acoustic Sound Speed

It can be shown that for an un-magnetized multi species plasma the general expression for the ion acoustic sound speed is given by:

$$C_S^2 = \frac{\sum \gamma_j p_j}{\sum \rho_j} \tag{F.8}$$

If we again assume that the plasma consists of bulk deuterium and a single fully stripped impurity species of charge Z_I then we can write:

$$C_S^2 = \frac{\sum \gamma_j p_j}{\sum \rho_j} \approx \frac{\gamma_D p_D + \gamma_i p_I + \gamma_e p_e}{m_D n_D + m_I n_I + m_e n_e} \tag{F.9}$$

The above expression is valid for an un-magnetized plasma, thus we may expect it to hold for sound waves propagating in the direction of the magnetic field. Substituting $p_j = n_j T_j$, ignoring the electron mass, and with the additional assumptions that $T_D \approx T_I = T_i$, $\gamma_D \approx \gamma_I = \gamma_i$ we obtain:

$$C_S^2 \approx \frac{\gamma_i T_i \left(n_D + n_I\right) + \gamma_e n_e T_e}{m_D n_D + m_I n_I} \tag{F.10}$$

If we further assume quasi-neutrality and (as in the derivation of m_{ave}) that $m_I \approx Z_I m_D$ then the expression above reduces to:

$$C_S^2 \approx \frac{T_I}{m_D}\left[\frac{\gamma_i \left(n_D + n_I\right) + \gamma_e n_e \left(T_e/T_i\right)}{n_e}\right] \tag{F.11}$$

Using the result for $n_D + n_I$ from equation F.4 from the m_{ave} derivation we obtain:

$$C_S^2 \approx \frac{\gamma_i T_i}{m_D}\left[1 - \left(\frac{Z_{eff} - 1}{Z_I}\right) + \frac{\gamma_e T_e}{\gamma_i T_i}\right] \tag{F.12}$$

If we further assume that the motion of the relatively slow ions is adiabatic ($\gamma_I = 3$) and that the motion of the relatively fast moving electrons is isothermal ($\gamma_e = 1$) then we obtain the final result:

$$C_S^2 \approx \frac{3T_i}{m_D}\left[1 - \left(\frac{Z_{eff} - 1}{Z_I}\right) + \frac{T_e}{3T_i}\right] \tag{F.13}$$

Appendix G

Rotation Generation Through Momentum Diffusivity Asymmetries

Bulk toroidal plasma rotation in discharges with no momentum input has been observed in a variety of machines. It will be shown that if particles with $v_{||} > 0$ and $v_{||} < 0$ can have slightly different toroidal momentum diffusivities, χ_ϕ, this can lead to significant bulk plasma rotation. To illustrate this effect we begin by considering momentum diffusion in a plasma column in which only axial flow is considered, with no source terms. Specifically

$$\frac{\partial L}{\partial t} + \nabla \cdot \Gamma = 0 \tag{G.1}$$

where $L \equiv \rho V \approx m_i n_i V_\phi$ is the toroidal momentum density (Ignoring the electron contribution). Here m_i is the ion mass, n_i is the ion particle density and V_ϕ is the axial flow velocity. If we assume a purely diffusive momentum flux then we have

$$\Gamma = -\chi_\phi \frac{\partial L}{\partial r} \tag{G.2}$$

Using cylindrical symmetry and substituting equation G.2 into G.1 gives

$$\frac{\partial L}{\partial t} - \frac{1}{r}\frac{\partial}{\partial r}\left(r\chi_\phi \frac{\partial L}{\partial r}\right) = 0 \tag{G.3}$$

We now modify this equation by considering positive and negative momentum separately by introducing the positive and negative momentum densities defined as:

$$L_+ \equiv m_i \int_{-\infty}^{\infty}\int_{-\infty}^{\infty}\int_{0}^{\infty} v_\phi f(\vec{v}) dv_x dv_y dv_\phi \tag{G.4}$$

$$L_- \equiv m_i \int_{-\infty}^{\infty}\int_{-\infty}^{\infty}\int_{-\infty}^{0} v_\phi f(\vec{v}) dv_x dv_y dv_\phi \tag{G.5}$$

where $f(\vec{v})$ is the distribution function of the main ions. Given these definitions it is possible to write separate conservation equations for positive and negative momentum.

$$\frac{\partial L_+}{\partial t} - \frac{1}{r}\frac{\partial}{\partial r}\left(r\chi_\phi^+ \frac{\partial L_+}{\partial r}\right) = F_{-/+} \tag{G.6}$$

$$\frac{\partial L_-}{\partial t} - \frac{1}{r}\frac{\partial}{\partial r}\left(r\chi_\phi^- \frac{\partial L_-}{\partial r}\right) = F_{+/-} \tag{G.7}$$

where $F_{i/j}$ is the force exerted on species j by species i. Note that in equations G.6 and G.7 the diffusivity for L+ and L- have been permitted to differ. Adding equations G.6 and G.7 gives:

$$\frac{\partial}{\partial t}\left(L_+ + L_-\right) - \frac{1}{r}\frac{\partial}{\partial r}\left(r\chi_\phi^+ \frac{\partial L_+}{\partial r} + r\chi_\phi^- \frac{\partial L_-}{\partial r}\right) = F_{+/-} + F_{-/+} \tag{G.8}$$

From the definitions of L_+ and L_- it follows that $L = L_+ + L_-$. Further, it is clear that the two friction terms cancel which gives

$$\frac{\partial L}{\partial t} - \frac{1}{r}\frac{\partial}{\partial r}\left(r\chi_\phi^+ \frac{\partial L_+}{\partial r} + r\chi_\phi^- \frac{\partial L_-}{\partial r}\right) = 0 \tag{G.9}$$

We now introduce the following variables:

$$\chi_\phi \equiv \frac{\chi_\phi^+ + \chi_\phi^-}{2} \tag{G.10}$$

$$\delta \equiv \frac{\chi_\phi^+ - \chi_\phi^-}{\chi_\phi} \tag{G.11}$$

Clearly χ_ϕ is the average of χ_ϕ^+ and χ_ϕ^-, while δ is a non-dimensional measure of the degree of the diffusivity asymmetry. Substitution of these variables into equation G.9 and some straightforward algebraic manipulations gives

$$\frac{\partial L}{\partial t} - \frac{1}{r}\frac{\partial}{\partial r}\left(r\chi_\phi \frac{\partial L}{\partial r}\right) = \frac{1}{r}\frac{\partial}{\partial r}\left[r\chi_\phi \delta \frac{\partial}{\partial r}\left(L_+ - L_-\right)\right] \tag{G.12}$$

To make further progress we must calculate $L_+ - L_-$. For computational simplicity we will assume that the distribution function of the ions can be approximated by a drifting Maxwellian, that is

$$f = \frac{n_i}{\pi^{\frac{3}{2}} v_{th}^3} \exp\left[-\frac{\left(\vec{v} - \vec{V}_\phi\right)^2}{v_{th}^2}\right] \tag{G.13}$$

where V_ϕ is the axial flow, v_{th} is the thermal speed, both of which can be functions of minor radius. Plugging this form of the distribution function into the definition for L_+ (equation G.4) and performing the appropriate integrals gives

$$L_+ = \frac{m_i n_i v_{th}}{\sqrt{\pi}}\left[\frac{1}{2} + \frac{\sqrt{\pi}}{2}M + \int_0^M (M - x)\exp\left(-x^2\right)dx\right] \tag{G.14}$$

where M represents the Mach number defined as $M \equiv V_\phi / v_{th}$. A similar calculation for L_- gives

$$L_- = -\frac{m_i n_i v_{th}}{\sqrt{\pi}}\left[\frac{1}{2} - \frac{\sqrt{\pi}}{2}M + \int_0^M (M - x)\exp\left(-x^2\right)dx\right] \tag{G.15}$$

Combining these results gives

$$L_+ - L_- = \frac{m_i n_i v_{th}}{\sqrt{\pi}}\left[1 + 2\int_0^M (M - x)\exp\left(-x^2\right)dx\right] \tag{G.16}$$

Taylor expanding the remaining integral for small Mach numbers yields

$$L_+ - L_- \approx \frac{m_i n_i v_{th}}{\sqrt{\pi}}\left[1 + 2M^2 - \frac{1}{3}M^4\right] = m_i n_i v_{th} G(M) \tag{G.17}$$

where $G(M) \equiv \pi^{-1/2}\left(1 + 2M^2 - M^4/3\right)$. We can now substitute equation G.17 into equation G.12 to obtain the final result

$$\frac{\partial L}{\partial t} - \frac{1}{r}\frac{\partial}{\partial r}\left(r\chi_\phi \frac{\partial L}{\partial r}\right) = \frac{1}{r}\frac{\partial}{\partial r}\left[r\chi_\phi \delta \frac{\partial}{\partial r}\left(m_i n_i v_{th} G\right)\right] = \tau(r) \tag{G.18}$$

This equation is the same as the diffusion equation with which we started (G.18) except for the new term on the right hand side, $\tau(r)$. This term implies that in the presence of a diffusivity asymmetry (i.e. $\delta \neq 0$) gradients in the thermal momentum density ($m_i n_i v_{th}$) can give rise to local torque densities and therefore drive flows. Given the relatively stiff nature of temperature and density profiles, the fact that $\tau(r)$ is proportional to gradients in $n_i T^{1/2}$ is consistent with the scaling of intrinsic rotation with stored energy. Figure G-1 shows the radial profile of the thermal momentum density, and its second derivative (proportional to τ) for a typical H-mode Alcator C-Mod discharge.

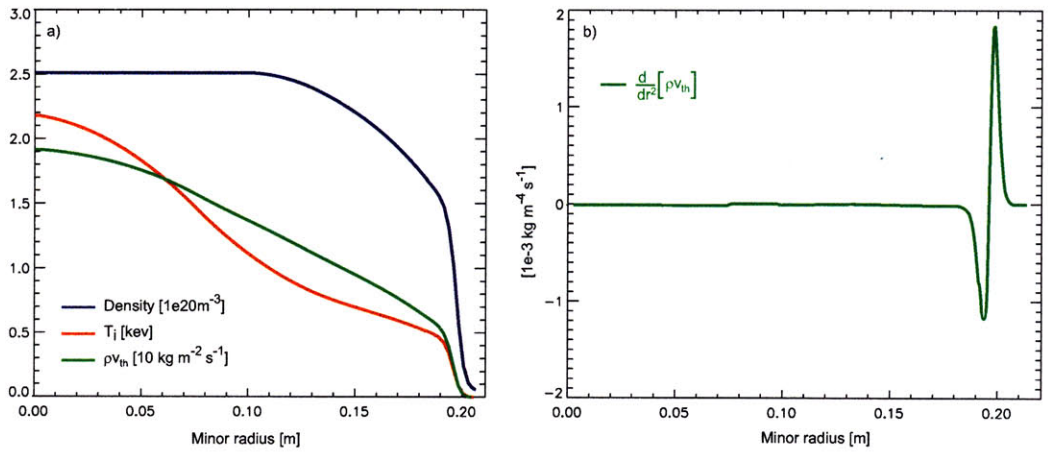

Figure G-1: Spatial profiles of a) thermal momentum density (ρv_{th}) and b) the second derivative of ρv_{th}.

Interestingly the radial profile of $\tau(r)$ is strongly localized to the edge region of the plasma which is consistent with the experimental evidence of an edge source of intrinsic rotation.

The total momentum input, P, can be calculated by integrating $\tau(r)$ over the plasma cross section

$$P = \int \tau dA = \int_0^{2\pi} \int_0^a r\tau(r) dr d\theta = 2\pi \int_0^a r\tau(r) dr \tag{G.19}$$

substituting the form of $\tau(r)$ from equation G.18 gives

$$P = 2\pi \int_0^a \frac{\partial}{\partial r} \left[r\chi_\phi \delta \frac{\partial}{\partial r} \left(m_i n_i v_{th} G(M) \right) \right] dr \tag{G.20}$$

Applying the fundamental theory of calculus gives

$$P = a\chi_\phi \delta \frac{\partial}{\partial r} \left(m_i n_i v_{th} G(M) \right) |_{r=a} \tag{G.21}$$

Equation G.21 shows that the momentum input $T(r)$ depends only on boundary conditions, i.e. it is the wall that is ultimately inputting momentum into the system.

G.0.1 Symmetry Breaking

The preceding derivation demonstrates that a momentum diffusivity asymmetry can drive flows but does not indicate what mechanisms might gives rise to such an asymmetry. As mentioned in chapter 6, the fact that the observed intrinsic rotation develops on time scales much shorter than those predicted by neoclassical theory suggests that a turbulence drive mechanism is involved. As described in chapter 5, there are a number of mechanisms that can break the symmetry of turbulent fluctuations ($\mathbf{E} \times \mathbf{B}$ velocity shear, magnetic curvature, etc.). As suggested in accretion theory, particles traveling at different speeds with respect to the phase velocity of turbulent fluctuations interact with that turbulence in different ways. Such an effect could give rise to the diffusivity asymmetries described above.

THIS PAGE INTENTIONALLY LEFT BLANK

Bibliography

[1] A. Bondeson and D. J. Ward. *Phys. Rev. Lett.*, 72:2709, 1994.

[2] R. Betti and J. Freidberg. *Phys. Rev. Lett.*, 74:2949, 1995.

[3] K.C. Shaing and E.C. Crume. *Phys. Rev. Lett.*, 63:2369, 1989.

[4] K.H. Burrell T.S. Hahm. *Phys. Plasmas*, 2:1648, 1995.

[5] S.M. Kaye. *Phys. Fluids*, 28:2327, 1985.

[6] S.A. Sabbagh et al. *Phys. Rev. Lett.*, 97:045004, 2006.

[7] Y. Liu et al. *Nucl. Fusion*, 44:232, 2004.

[8] J.E. Rice et al. *Nucl. Fusion*, 47:1618, 2007.

[9] H. Griem. *Principles of Plasma Spectroscopy.* Cambridge University Press, Cambridge, United Kingdom, 1997.

[10] R. E. Bell. *Rev. Sci. Instrum.*, 68:1273, 1997.

[11] I. Condrea et al. *Phys. Plasmas*, 7:3641, 2000.

[12] B.S. Fraenkel and M. Bitter. *Rev. Sci. Instrum.*, 70:296, 1999.

[13] H.H. Johann. *Z. Phys.*, 69:185, 1931.

[14] M. Bitter et al. *Rev. Sci. Instrum.*, 70:292, 1999.

[15] J. H. Underwood. *X-ray Data Booklet.* Lawrence Berkeley National Laboratory, Berkeley, California, 2004.

[16] W.H. Zacharissen. *Theory of X-ray Diffraction in Crystals.* Wiley, New York, 1945.

[17] S. K. Allison. *Phys. Rev.*, 41:1–20, 1932.

[18] M. Bitter et al. *Rev. Sci. Instrum.*, 66:530, 1995.

[19] H. De Lang. *Physica*, 25:945, 1959.

[20] E. Eikenberry et al. *Nucl. Instr. Meth. A*, 501:260, 2003.

[21] S.G. Lee et al. *Rev. Sci. Instrum.*, 74:1997, 2003.

[22] E. Eikenberry et al. http://pilatus.web.psi.ch/pilatus.htm.

[23] S.M. Wolfe et al. *Phys. Plasmas*, 12:056110, 2005.

[24] J.E. Rice et al. *Nucl. Fusion*, 44:379, 2004.

[25] Y.B. Kim et al. *Phys. Fluids B*, 3:2050, 1997.

[26] M.F. Gu. *Astrophys J*, 582:1241, 2003.

[27] A. Ince-Cushman et al. *Rev. Sci. Instrum.*, 2008.

[28] The data for this plot was generously provided by M.F. Gu. based on calculations using the FAC (Flexible Atomic Code).

[29] M. Bitter et al. *Can. J. Phys.*, 86:291, 2008.

[30] P.M. Schoch et al. *Rev. Sci. Instrum.*, 74:1846, 2008.

[31] W. Solomon et al. *Phys. Plasmas*, 13:056116, 2006.

[32] W.M. Solomon et al. *Phys. Plasmas*, 13:056116, 2006.

[33] S.P. Hirshman and D.J. Sigmar. *Nucl. Fusion*, 21:1079, 1981.

[34] A. Rogister. *Phys. Plasmas*, 6:200, 1999.

[35] I. Braginskii. *Reviews of Plasma Physics*, 1:205, 1965.

[36] A. Rogister et al. *Nucl. Fusion*, 42:1144, 2002.

[37] J.E. Rice et al. *Phys. Plasmas*, 11:2427, 2004.

[38] F.W. Perkins et al. *Phys. Plasmas*, 8:2181, 2001.

[39] C.S. Chang et al. *Phys. Plasmas*, 8:2181, 2001.

[40] L.-G. Eriksson et al. *Phys. Rev. Lett.*, 23:235001, 2004.

[41] J. E. Rice et al. *Nucl. Fusion*, 41:277, 2001.

[42] B. Coppi. *Nucl. Fusion*, 42:1, 2002.

[43] J.E. Rice et al. *Nucl. Fusion*, 38:75, 1998.

[44] J.E. Rice et al. *Nucl. Fusion*, 39:1175, 1999.

[45] B. Coppi et al. *Phys. Fluids*, 10:582, 1967.

[46] B. Coppi and F. Pegoraro. *Nucl. Fusion*, 17:969, 1977.

[47] K.C. Shaing. *Phys. Rev. Lett*, 86:640, 2000.

[48] O. D. Gurcan et al. *Phys. Plasmas*, 14:042306, 2007.

[49] T.S. Hahm et al. *Phys. Plasmas*, 14:072302, 2007.

[50] J.E. Rice et al. *Nucl. Fusion*, 45:251, 2005.

[51] B. LaBombard et al. *Nucl. Fusion*, 44:1047, 2004.

[52] A. Scarabosio et al. *Plasma Phys. Control. Fusion*, 48:663, 2006.

[53] A. Bortolon et al. *Phys. Rev. Lett*, 97:235003, 2006.

[54] B.P. Duval et al. *Plasma Phys. Control. Fusion*, 49:B195, 2007.

[55] B.P. Duval et al. *Phys. Plasmas*, 15:056113, 2008.

[56] L.G. Eriksson et al. *Plasma Phys. Control. Fusion*, 39:27, 1997.

[57] I.H. Hutchinson. *Phys. Rev. Lett.*, 84:3330, 2000.

[58] J. E. Rice et al. *Phys. Plasmas*, 7:1825, 2000.

[59] J.S. deGrassie et al. *Phys. Plasmas*, 11:4323, 2004.

[60] J.S. deGrassie et al. *Phys. Plasmas*, 14:056115, 2007.

[61] I.H. Coffey et al. *Proc. 11th Colloquium on UV and x-ray Spectroscopy of Astrophysical and Laboratory Plasmas*, 15:431, 1995.

[62] W.D. Lee et al. *Phy. Rev. Lett.*, 91:205003, 2003.

[63] S. Assas et al. Toroidal plasma rotation in icrf heated tore supra discharges. *30th EPS Conf. on Plasma Physics and Controlled Fusion*, 27:(ECA) P–1.138, 2003.

[64] ITER Physics Expert Group on Confinement and Transport. *Nucl. Fusion*, 39:2175, 1999.

[65] Christiansen et al. *Nucl. Fusion*, 32:291, 1992.

[66] E.J. Strait et al. *Phys. Rev. Lett*, 74:2483, 1994.

[67] M. Kotschenreuther L.J.Zheng and M.S. Chu. *Phys. Rev. Lett*, 95:225003, 1994.

[68] A.M. Garofalo et al. *Nucl. Fusion*, 47:1121, 2007.

[69] P.T. Bonoli et al. *Fusion Sci. Tech.*, 51:401, 2007.

[70] L.L. Lao et al. *Phys. Rev. Lett*, 22:3435, 1993.

[71] N. J. Fisch and C. F. F. Karney. *Phys. of Fluids*, 24:27, 1981.

[72] N.J. Fisch, editor. *Proceedings of the Second Joint Verenna-Grenoble International Symposium on Heating Toroidal Plasmas, Como, Italy*, 1980.

[73] A.A. Ware. *Phys. Rev. Lett.*, 25:15, 1970.

[74] W. Perkins. *Nucl. Fusion*, 17:1197, 1997.

[75] H. Stix. *Waves in Plasmas.* American Institute of Physics, New York, New York, 1992.

[76] P. T. Bonoli et al. *Phys. Plasmas*, 4:1774, 1997.

[77] E. Nelson-Melby et al. *Phys. Rev. Lett.*, 90:155004, 2003.

[78] Y. Lin et al. *Phys. Plasmas*, 11:2466, 2004.

[79] Y. Lin et al. *Plasma Phys. Control. Fusion*, 47:1207, 2005.

[80] L.A. Berry et al. *Phys. Rev. Lett.*, 82:1871, 1999.

[81] J.R. Myra and D.A. D'Ippolito. *Phys. Plasmas*, 9:3867, 2002.

[82] D.A. D'Ippolito J.R. Myra and E.R. Jaeger. *Phys. Plasmas*, 11:1786, 2004.

[83] C. K. Phillips et al. *Nucl. Fusion*, 40:461, 2000.

[84] P. T. Bonoli et al. *Nucl. Fusion*, 51:401, 2007.

[85] R. C. Morris et al. *Phys. Plasmas*, 12:4513, 1996.

[86] W.D. Lee et al. *Phys. Rev. Lett*, 91:205003, 2003.

[87] K Ida. *Plasma Phys. Control. Fusion*, 40:1429, 1998.

[88] L.L. Lao et al. *Nucl. Fusion*, 25:1611, 1985.

[89] J.M. Noterdaeme et al. *Nucl. Fusion*, 43:274, 2003.

[90] G.T. Hoang et al. *Nucl. Fusion*, 40:913, 2000.

[91] L.G. Eriksson et al. *Nucl. Fusion*, 41:91, 2001.

[92] Y. Sakamoto et al. *Plasma Phys. Control. Fusion*, 48:A63, 2006.

[93] L. Porte et al. *Nucl. Fusion*, 47:952, 2007.

[94] T.H. Stix. *Phys. of Fluids*, 16:1260, 1973.

[95] J.E. Rice et al. *Phys. Rev. A*, 35:3033, 1987.

[96] J.E. Rice et al. *Phys. Rev. A*, 51:3551, 1995.

[97] J.E. Rice et al. *Nucl. Fusion*, 37:421, 1997.

[98] E.S. Marmar et al. *Phys. Rev. A*, 33:774, 1986.

[99] I.H. Hutchinson. Introduction to plasma physics. Course notes, 2003.